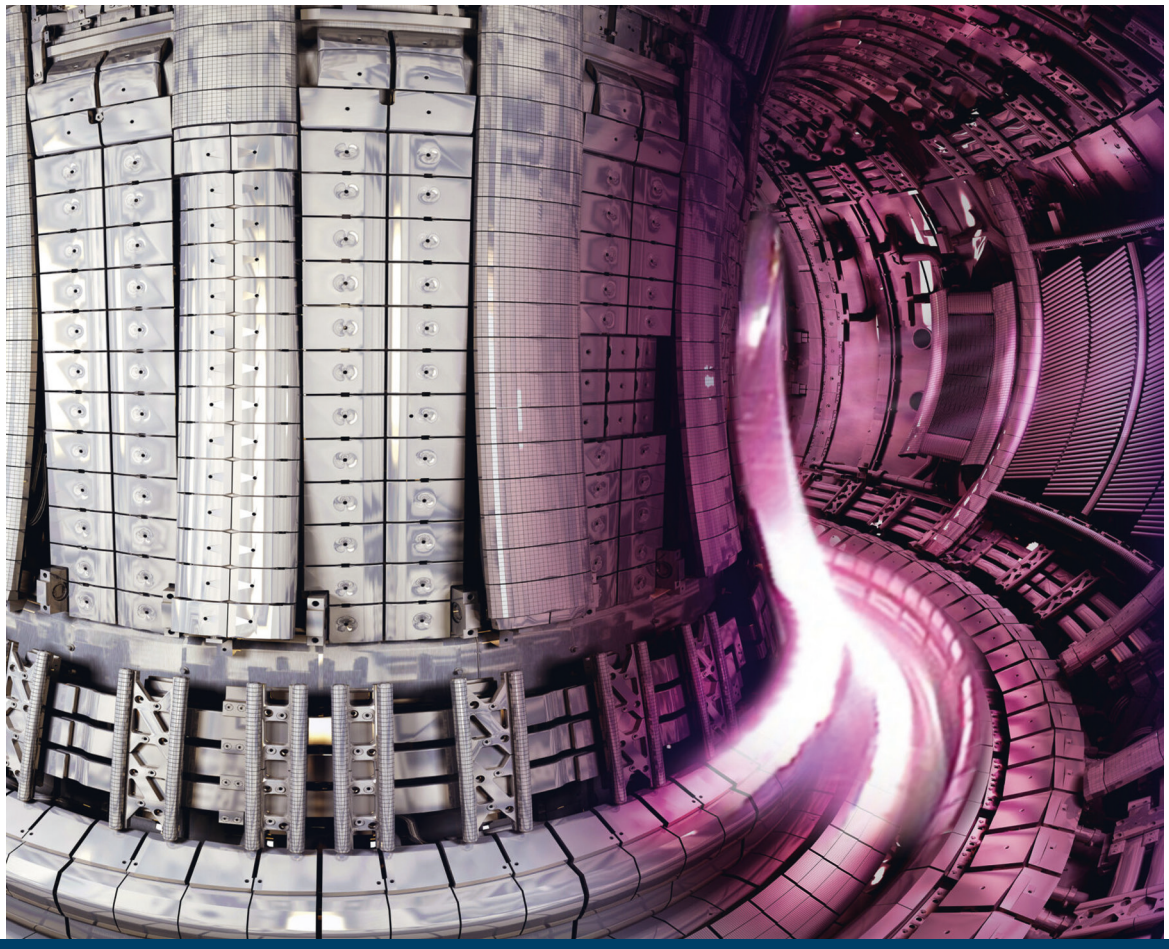

Plasma Breakdown and Runaway Modelling in ITER-scale Tokamaks

Junxian Chew

IAS Series
Band / Volume 57
ISBN 978-3-95806-730-1

Mitglied der Helmholtz-Gemeinschaft

JÜLICH
Forschungszentrum

Schriften des Forschungszentrums Jülich
IAS Series Band / Volume 57

Forschungszentrum Jülich GmbH
Institute for Advanced Simulation (IAS)
Jülich Supercomputing Centre (JSC)

Plasma Breakdown and Runaway Modelling in ITER-scale Tokamaks

Junxian Chew

Schriften des Forschungszentrums Jülich
IAS Series Band / Volume 57

ISSN 1868-8489 ISBN 978-3-95806-730-1

Bibliografische Information der Deutschen Nationalbibliothek.
Die Deutsche Nationalbibliothek verzeichnet diese Publikation in der
Deutschen Nationalbibliografie; detaillierte Bibliografische Daten
sind im Internet über http://dnb.d-nb.de abrufbar.

Herausgeber und Vertrieb:	Forschungszentrum Jülich GmbH Zentralbibliothek, Verlag 52425 Jülich Tel.: +49 2461 61-5368 Fax: +49 2461 61-6103 zb-publikation@fz-juelich.de www.fz-juelich.de/zb
Umschlaggestaltung:	Grafische Medien, Forschungszentrum Jülich GmbH
Druck:	Grafische Medien, Forschungszentrum Jülich GmbH
Copyright:	Forschungszentrum Jülich 2023

Schriften des Forschungszentrums Jülich
IAS Series, Band / Volume 57

D 294 (Diss. Bochum, Univ., 2022)

ISSN 1868-8489
ISBN 978-3-95806-730-1

Vollständig frei verfügbar über das Publikationsportal des Forschungszentrums Jülich (JuSER)
unter www.fz-juelich.de/zb/openaccess.

Declaration of Authorship

Ruhr-Universität Bochum
Physik und Astronomie

RUHR
UNIVERSITÄT
BOCHUM

RUB

Junxian Chew
Name, Vorname

Eidesstattliche Versicherung gemäß § 7 Abs. 2 Nr. 6 PromO 2011

Hiermit versichere ich, dass ich meine Dissertation selbstständig und ohne unerlaubte fremde Hilfen angefertigt und verfasst habe und keine anderen als die angegebenen Hilfsmittel und Hilfen benutzt habe. Meine Dissertation habe ich in dieser oder ähnlicher Form noch bei keiner anderen Fakultät der Ruhr-Universität Bochum oder bei einer anderen Hochschule eingereicht.

Bochum, den 21.12.2022 .....

.....
Unterschrift

"Nuclear fusion might just be the fanciest way to boil water in all of human history yet!"

Unknown origin

Acknowledgements

I would like to express my gratitude to Prof. Dr. Paul Gibbon for providing a research environment that encourages exploration of ideas. It is invaluable to be granted a measure of autonomy in the process of developing a numerical model and conducting simulation studies. His guidance in research directions and the numerous discussions have been the catalysts towards the completion of the research work.

A special thanks to Dr. Dirk Brömmel for making the time for discussions that compelled me to scrutinize my own code development and results analysis methodologies. The presented challenges improved the scientific rigorousness of the conducted studies.

I would also like to acknowledge the role of Dr. Peter De Vries from the ITER organisation in this project, who kick-started this topic more than 4 years ago. His interests and enthusiasm in modelling the plasma breakdown have played a crucial role throughout the study. Numerous discussions with him have solidified the numerical setups of various tokamak operating conditions. The discussions also helped define the scope of study and the following set of analyses.

The rest of the ITER science team, specifically Dr. Yuri Gribov and Dr. Tom Wauter, have been invaluable in providing feedback for the presented numerical results and write-ups related to the tokamak simulations. For that I am thankful for their involvement and interests.

I would also like to thank Prof. Dr. Unterberg and Prof. Dr. Grauer for their trust in me and their willingness to be my supervisors in Ruhr-Universität Bochum. Without their involvements, the doctoral study process would never have been possible. I also deeply appreciate the time they took to have numerous one-on-one discussions about my work, which gave me useful suggestions that helped improve the research work.

Deepest of gratitude towards Jülich Supercomputing Centre for providing the computational resources which enabled the numerical studies. The center also provided the tools necessary to develop a simulation program that has high parallel efficiency and the research project would not be possible without it.

Lastly, I would like to express my thanks to my parents for allowing me to pursue my interests in science. Their unwavering support gave me a peace of mind necessary to see the project to an end.

Contents

List of Figures

List of Tables

I dedicate this work to my dreams & ideals that died along the way...

Chapter 1

Introduction

At the time of writing this thesis, the world's largest tokamak device named the International Thermonuclear Experimental Reactor (ITER) is under construction. This experiment presents a long list of engineering and scientific challenges to be solved. Among the many scientific questions that it will try to answer throughout its operational lifetime, demonstrating that the existing ITER design is able to generate 10 times more fusion power than the power fed into the device is one of the more prominent goals. In other words, the experiment aims to find out if ITER can achieve a fusion gain factor $Q \approx 10$.

The success of ITER will be seen as a major step towards the future of integrating nuclear fusion energy into the existing power grid infrastructure, providing a new source of clean energy production to meet the growing annual energy demands worldwide [10]. As the awareness of the impending climate crisis surfaces, there has been an increase in clean energy infrastructure investments globally [11]. This is also mirrored in fusion energy research. The 2022 Global Fusion Industry Report by the Fusion Industry Association (FIA) [12] found that the private sector of fusion energy research had an increase of 139 % in funding from the year before, reaching a record of $4.7bn. Thus, the drive and motivation towards energy production via nuclear fusion cannot be overstated.

There are multitudes of scientific challenges that must be solved to realise long pulse high-performance discharges, crucial for providing stable and continuous electricity generation. Among them is the accumulation of impurities in the plasma core causing instabilities and disruption of the plasma [13], suppression of edge-localised modes (ELMs) which could cause damage to plasma-facing components (PFC) [14], and thermal stresses on PFCs due to cyclical heat loading during pulsed operations [15].

Notable progress was made over the decades of research and they help us better understand the respective complex physics. However, there are areas of research that weren't given due attention, being perceived as having less importance towards the goal of energy production. One such topic is the plasma initiation during the tokamak startup process, where it is theorised that charged particle number densities develop over time as a result of Townsend avalanche breakdown. There have been research works done in that regard [16–18], but the number of reported studies pale in comparison to the study of plasma instabilities for example. It should also be noted that the studies of plasma initiation are mostly numerical or theoretical.

There is a need for additional research work in the area, especially when there are new tokamaks with record sizes (ITER, and perhaps DEMO for example), in which the validity of long-established theories could be challenged. Taking advantage of the impressive computational resources available at the Jülich Supercomputing Center in Forschungszentrum Jülich, they enabled the possibility of conducting first principles numerical studies of the plasma initiation process in an ITER-scale tokamak device. Throughout this study, upward of 18 million core-hours and 5 million core-hours were consumed on the JURECA Booster and JURECA DC systems respectively. This study aims to construct a numerical solver that is capable of simulating the growth of charged particle population via electron-neutral impact ionisation, and provide insight into the influence of background electric and magnetic fields on the growth rate and time evolution of electrons' velocity distribution. Adhering to the first principles modelling paradigm, efforts were committed to avoiding assumptions that reduce the spatial dimension of the numerical simulation. Further numerical implementation details and the supporting motivations are discussed throughout the thesis.

This thesis is separated into chapters that describe the various aspects related to the developed numerical model. The thesis continues with the theory of tokamak breakdown in Chapter 2, which also details the main goals of this study. This is then followed by the description of numerical considerations and the implementations of the solver in Chapter 3. This is then followed by a discussion on the merging algorithm in Chapter 4, developed for high electron number density scenarios. Chapter 5 then discusses numerical tests of the implemented solver, to choose the scattering angle model which yields the best approximation of ionisation rate when compared with prior parallel plate experiment. The benchmarked results inform the choice of scatter model for use in the tokamak plasma initiation simulation, which is the focus of Chapter 6. Chapter 7 then extends the numerical studies to the variants of the field geometry within the tokamak, which is done to improve the understanding of background fields to ionisation fraction

growth rate, velocity distribution and spatial distribution of charges etc. A summary of the study and the discussions on future works is covered in Chapter 8.

Chapter 2

Tokamak breakdown physics

2.1 General description of tokamak

The fusion of lighter two nuclei into heavier nuclei (at the very low nucleon number range) releases an amount of energy that is equivalent to the mass difference before and after the reaction. This total energy is in the order of $\sim 10\,\mathrm{MeV}$ for a fusion event that produces ^{4}He as a byproduct, which pales in comparison to a fission event that releases $\sim 100\,\mathrm{MeV}$. However, the measure of energy per nucleon paints a very different picture. For example, released energy per nucleon from D-T fusion reaction reaches about $3.5\,\mathrm{MeV}$ while fission of U-235 into Ba-144 and Kr-89 isotopes is at approximately $0.7\,\mathrm{MeV}$, concluding that energy per unit mass of fuel in fusion reaction is clearly higher. Therefore, it is of interest to tap into such a method to complement the existing energy production infrastructure. Another key attraction of nuclear fusion as an energy source is the significantly lower degree of radioactivity of the fusion byproduct (and its surrounding reactor structure) when compared with nuclear fission [19, 20]. Fusion reaction between the light nuclei can happen when they overcome the Coulomb potential barrier which is in the order of $100\,\mathrm{keV}$ and above (D-T reaction requires approximately $380\,\mathrm{keV}$ in the center-of-mass frame), which translates to a plasma temperature in excess of $10^9\,\mathrm{K}$ for such direct fusion to occur. A silver lining to that immense energy requirement is that the fusion reaction can already occur at a much lower energy level due to the quantum tunneling effect. As seen in Fig. 2.1, D-T reaction is the candidate that has the least energy threshold while having a reasonable cross section from $10\,\mathrm{keV}$ onward, which corresponds to plasma temperature in excess of $10^8\,\mathrm{K}$. As such, this reaction became the prime candidate for future energy production via fusion.

There are two primary methods to achieve fusion, which are inertial confinement and

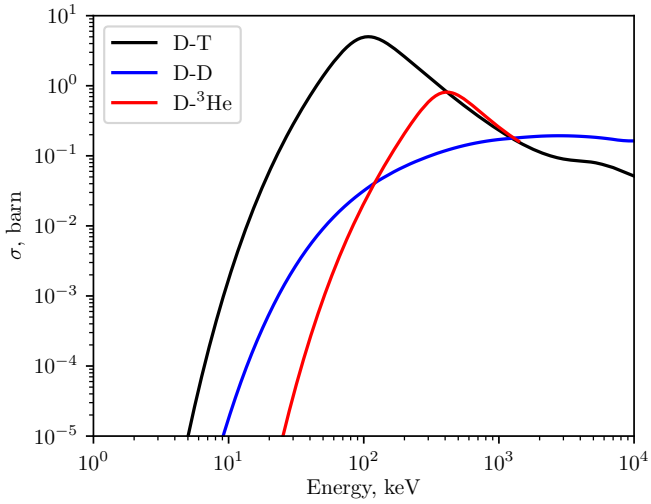

FIGURE 2.1: Cross sections of the corresponding fusion reactions [1].

magnetic confinement respectively. Among the machines designed for magnetic confinement fusion, the stellator and the tokamak are the two commonly explored methods. This work focuses on the tokamak and a brief description of its major components is given here. Since the temperature range of plasma is targeted to be above 10 keV for a noticeable fusion reaction to occur, the plasma will have to be suspended in vacuum. Since plasma is a collection of charged particles, the particles will be confined along the experienced magnetic field. The idea is then to design a magnetic field geometry that is closed (which loops back to itself). As such, the charged particle will remain confined for as long as the magnetic field loop is closed. One of the geometries that fulfills this condition is a torus, which is subsequently reflected in the generic shape of a tokamak. Alas, perfect confinement property isn't simple to achieve in reality since the dynamics of the plasma will interact with the prescribed background field, and stray fields which causes poor confinement will always be a challenge to overcome. Various forms of instabilities (e.g. from plasma turbulence or some slight imbalance of magnetic forces in the plasma column, to name a few) will also be ever-present, and they all have to be controlled to achieve good confinement properties. The following description will ignore any form of imperfection in the prescribed field so that a singular focus is placed on the general workings of a tokamak.

During the operation of a tokamak, the toroidally shaped magnetic field is generated by the passing current through the series of superconducting toroidal field coils surrounding the vacuum vessel torus. This creates the magnetic field vector that is parallel to the torus' minor axis, whose purpose is to confine the charged particles in the

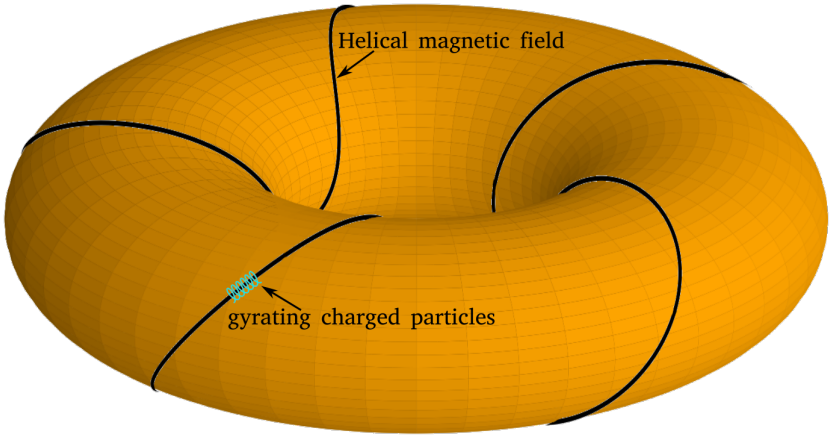

FIGURE 2.2: Sketch of magnetic field in a tokamak plasma column. Torus volume represents confined plasma.

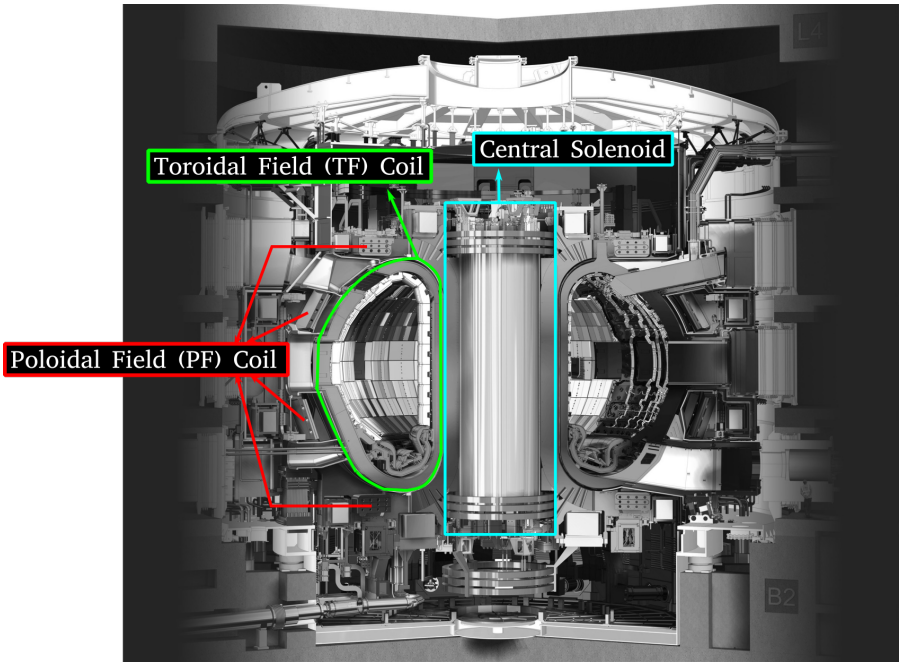

FIGURE 2.3: Magnetic coil placements in ITER.

same direction. An additional magnetic field in the poloidal direction (perpendicular to the toroidal field) is also required. This is to correct the induced drift motion of charged particles (multiple drifts have been identified, some of them being the $\mathbf{E} \times \mathbf{B}$ drift and $\nabla \mathbf{B}$ drift).

In order to illustrate the need for poloidal fields, assume a quasi-neutral plasma confined within a torus with a purely toroidal magnetic field. Due to a denser arrangement of the toroidal field coil near the central solenoid, the resulting toroidal field will have a negative gradient along the outboard direction. Gyromotion of the charged particles as they travel along the torus necessarily causes a vertical charged separation between the positive and negatively charged particles (a manifestation of the $\nabla \mathbf{B}$ drift). The separation will, in turn, cause the formation of a vertically aligned self-consistent $\mathbf{E}$ field. As the $\mathbf{E}$ field becomes more significant over time, the charged particle's interaction with both the vertical $\mathbf{E}$ and the purely toroidal $\mathbf{B}$ will cause a drift motion (termed $\mathbf{E} \times \mathbf{B}$ drift) along the horizontal plane of the torus. Such horizontal drift causes poor confinement as the charged particles will continuously stream out of the plasma column. The existence of the poloidal field is then required to introduce a helical twist to the otherwise purely toroidal magnetic field so that the confined charged particles (both negative and positively charged) will traverse along the now formed magnetic flux surface in Fig. 2.2. The created magnetic flux surface is a result of the addition of both the toroidal and poloidal fields, which can be imagined as a thin torus surface where particles will always reside on. The ratio between the particle's angular traverse in the poloidal direction ι and in a single toroidal revolution 2π is termed the field line pitch. Once again, a closed flux surface example here is a crude simplification. In reality, there will always be magnetic stray fields that end at the vessel wall and particle losses are expected before the plasma current rises to the threshold needed to form a self-consistent closed magnetic flux surface.

The poloidal field responsible for the formation of a closed magnetic flux surface arises mainly from the plasma current itself. The PF coils shown in Fig. 2.3 serve a few different functions during tokamak operation. Chief among them is creating the magnetic null configurations in the vacuum vessel, providing the initial confinement property of free charges to facilitate plasma initiation. During the later phase of the operation, the coils contribute and provide control toward the overall equilibrium field of plasma. PF coils are also capable of providing plasma heating via the inductive current drive (ramp-up of the current flow in the coils, inducing a toroidal electric field) [21]. Lastly, the central solenoid is the major component that provides the major toroidal electric field for the tokamak, which is primarily used for initiating the plasma. The creation of such an electric field is once again through electromagnetic induction, as the current in

the solenoid continuously ramps up during the operation.

At the stage when plasma (electron density reaching $\sim 10^{19}\,\mathrm{m}^{-3}$) is formed, continuous plasma heating can be augmented via a few different methods. First among the notable methods is the neutral-beam injection (NBI). This method operates on the consideration that direct injection of ionised fuel (deuterium ions and the like) into the plasma column is difficult due to deflection from strong magnetic fields, penetration depth will then be less than ideal and heating from direct ion source is ineffective. As such, direct delivery of highly energetic neutral molecules into the plasma is favourable. Such energetic neutrals will then be ionised from collisions with existing ions within the plasma, and confined by the existing magnetic field structure. The newly ionised high-energy ions will then deposit their energy to the existing charged particles via Coulomb interaction, relaxing into a new thermal equilibrium. The plasma temperature is demonstrably raised as a result of such injection [22, 23].

Another method used for plasma heating would be electron/ion cyclotron resonance heating (E/ICRH). Effective energy deposition from radio frequency (RF) waves is dependent on the cyclotron frequency of the targeted charged particle species. This is because energy transfer to the charges occurs when RF frequency is at a specific charge's cyclotron frequency (the result of cyclotron resonance) [24]. Since electrons are much lighter than protons, the electron cyclotron frequency is approximately 1836 higher than the proton's, and the electron-ion cyclotron frequency ratio grows larger when the ion mass is heavier. This dictates the RF range differences required by ECRH and ICRH respectively. In the ITER tokamak, gyrotron for ECRH is targeted to operate at 170 GHz while the ICRH system is in the range of 40 - 55 MHz. Heating via RF comes with higher physical complexity when compared with NBI, due to the dynamic interaction between the RF wave and the self-consistent fields originating from the plasma itself. Other considerations, such as the effective propagation of the RF waves into the plasma core (through the study of plasma dispersion relation), are not discussed here.

In the pursuit of demonstrating that nuclear fusion is a viable energy production source, the fusion energy gain factor Q is generally used as a metric to measure the performance of a tokamak. The following section will elaborate on the expression of Q, as well as provide a glimpse into the growing trend of tokamak machines towards energy production-ready prototypes.

2.1.1 Scaling laws and tokamak dimensions

Assuming a scenario where the plasma within a tokamak is confined in a steady-state equilibrium, the Q factor can be described as the ratio between the fusion power P_{fus} and the external power P_{ext} supplied into the plasma to sustain fusion ready temperatures (above 10 keV). P_{ext} includes all channels of energy loss over time P_{loss}, which can be radiative power loss as well as loss of energetic particles due to poor confinement. This power loss is then offset by the fraction c of retained fusion power. In order to maintain the plasma temperature,

$$P_{\text{ext}} = P_{\text{loss}} - cP_{\text{fus}} \tag{2.1}$$

should be fulfilled at all times. The approximate fraction c of power retention that arises from the energy partition of the nuclear fusion is explained as follows. Since the considered fusion candidates undergo a neutronic fusion process (where one of the outcomes of the fusion process is a free energetic neutron), P_{fus} can be separated into the power carried by the neutron and another part that is carried by the resulting heavy nuclei (^{4}He for D-T fusion, T for D-D fusion). Taking the example of D-T fusion, the nuclear reaction is expressed as

$$^2_1\text{D} + ^3_1\text{T} \rightarrow ^4_2\text{He} + ^1_0\text{n} + 17.6\,\text{MeV},$$

where approximately one fifth of the 17.6 MeV is carried by $^4_2$He particle. The remaining ~ 14.1 MeV is carried by the neutrons, which quickly leave the confined plasma as it is charge neutral. The heavy nuclei can be further ionised within the plasma, thus retaining that portion of fusion power. As such, $c \approx 1/5$ is determined. The final expression for Q is then

$$Q = \frac{P_{\text{fus}}}{P_{\text{ext}}} \approx \frac{P_{\text{fus}}}{P_{\text{loss}} - \frac{1}{5}P_{\text{fus}}}. \tag{2.2}$$

Conventionally, P_{loss} is treated as the plasma energy W over the energy confinement time τ_{E}. By substituting Eq. 2.2 and definition of P_{loss} into Eq. 2.1, a simple description of the energy confinement time is then

$$P_{\text{loss}} \approx \frac{W}{\tau_{\text{E}}} \approx P_{\text{fus}}\left(\frac{1}{Q} + \frac{1}{5}\right). \tag{2.3}$$

Assuming that the number density of D and T ions are identical and homogeneous in space, necessarily means that each of them is half of the overall ion density ($n_{\text{D}} = n_{\text{T}} = n/2$). It is also assumed that the ion temperature distribution is Maxwellian, centered around temperature T. P_{fus} can then be approximated as the rate of fusion event per unit time multiplied by the fusion energy release per event E_{fus}. The event rate is

computed as

$$\dot{N}_{\text{fus}} = \int n_{\text{D}}\ n_{\text{T}}\ \sigma\nu\ \mathrm{d}V = \frac{n^2}{4}\sigma\nu V \tag{2.4}$$

where V denotes the plasma volume. σ refers to the D-T cross section in Fig. 2.1 and ν the ion velocity, both these variables are averaged values at ion temperature T. The expression for P_{fus} is then

$$P_{\text{fus}} = \frac{n^2}{4}\sigma\nu V\ E_{\text{fus}}, \tag{2.5}$$

where $E_{\text{fus}} = 17.6\,\text{MeV}$ in the case of D-T fusion. The final piece of information required to derive the energy confinement time τ_{E} is the plasma energy W, which is obtained by simply treating the charged particle ensemble (both ions and electrons) as ideal gas. The expression comes up to be

$$W = 3nk_{\text{B}}TV, \tag{2.6}$$

assuming that the ion temperature is the same as the electron temperature. This assumption is valid considering that it is a hot plasma at fusion ready energy threshold. Substituting Eq. 2.5 and Eq. 2.6 into Eq. 2.3 will yield

$$\tau_{\text{E}} \approx \frac{12k_{\text{B}}}{n\sigma\nu}\frac{1}{\left(\frac{1}{Q}+\frac{1}{5}\right)}. \tag{2.7}$$

Multiplying Eq. 2.7 with nT will give the well-known expression of Lawson's criterion. Should a target fusion energy gain Q_{target} and above is required from a tokamak, the triple product requirement is then

$$nT\tau_{\text{E}} \geq \frac{12k_{\text{B}}T}{\sigma\nu}\frac{1}{\left(\frac{1}{Q_{\text{target}}}+\frac{1}{5}\right)}.$$

Even though the energy confinement time is now derived in Eq. 2.7, several crucial assumptions were made along the process. It was known that the neoclassical model (let alone Lawson's criterion) is inadequate in explaining experimentally measured energy confinement behaviour [25]. Thus, showing that a fundamental understanding of the underlying physics which determines the P_{fus} and P_{loss} is rather incomplete. Therefore, a concise analytical expression for both variable has not been proposed as of yet. However, one could still attempt to measure the power output of various tokamak operations and data fit it to a proposed empirical expression.

This is also true for the energy confinement time parameter τ_{E}. There is not one standardised expression for τ_{E} and its set of variables encompasses macro observables of the tokamak geometry and the plasma. Among those variables, two primary limits of the confined plasma are always incorporated [26]. They are the β limit of the specific tokamak (could be derived from the stability condition of Grad-Shafranov equation [27–29])

and the plasma current limit [30, 31] (written as a function of the safety factor q). One suggested scaling of τ_{E} is reported [32] as

$$\tau_{\mathrm{E}} = C_1 \tau_{\mathrm{Bohm}}^{x_\tau} \rho_*^{x_\rho} \nu_*^{x_\nu} \beta^{x_\beta} M^{x_M} q^{x_q} \varepsilon^{x_\varepsilon} \kappa^{x_\kappa}. \tag{2.8}$$

The above variables are, C_1 and the rest of x_* parameters denote the generic fitting coefficients, τ_{Bohm} being the Bohm time, ρ_* the ion Larmor radius normalised by the torus minor radius, ν_* the normalised collisionality (ratio between connection length and ion mean free path), β is the ratio of plasma pressure and magnetic pressure, M the average ion mass, q the cylindrical safety factor, ε the inverse torus aspect ratio, and κ the elongation of the plasma. The formulation for τ_{Bohm}, ρ_*, ν_* and q is not elaborated here. The detailed formulation can be found in the second chapter of ITER physics basis [32]. As an example of the mentioned data fitting, Zohm *et al* [33] reported the fitting of Eq. 2.8 expression using the ITERH.DB3 dataset as

$$\tau_{\mathrm{E}} \sim H^{3.23} \tau_{\mathrm{Bohm}} \rho_*^{-0.7} \beta^{-0.9} q_{95}^{-3} A^{-0.73}. \tag{2.9}$$

Here, H is defined as the confinement limit, q_{95} is the safety factor at the position where 95% of the poloidal flux is covered by a flux surface along the torus' horizontal plane and $A = 1/\varepsilon$. Note that τ_{E} is no longer dependent on plasma temperature T, which resulted from an assumption that the tokamak is always operating in the fusion ready temperature above 10 keV. Zohm also suggested that P_{fus} can be represented by

$$P_{\mathrm{fus}} = c_1 \frac{\beta^2 B^4 R_0^3}{q_{95}^2 A^4},$$

with B representing the toroidal magnetic field strength and R_0 the tokamak's major radius. Along with the P_{loss} as

$$P_{\mathrm{loss}} \sim c_2 \frac{\beta_N^{1.9} \, R_0^{0.3} \, B^{0.3} \, q_{95}^{1.1}}{H^{3.23} A^{0.47}},$$

Eq. 2.2 can be computed as a function of R_0. Here, $\beta_N = \beta q_{95} A$. Fig. 2.4 demonstrated clearly that one of the ways to raise the Q factor is by increasing the major radius of the tokamak. This explains the motivation behind the ITER tokamak's size in pursuit of reaching $Q = 10$ at $R_0 \approx 6$ m. The DEMO experimental tokamak that follows in the footsteps of ITER will likely be larger. The other method of pushing for higher Q factor is through higher toroidal magnetic field strength [34], as a higher B will be able to increase the τ_{E} through the β, q_{95}, ρ_* and τ_{Bohm} in Eq. 2.9.

While the discussions up to this point explore the viability of nuclear fusion as an

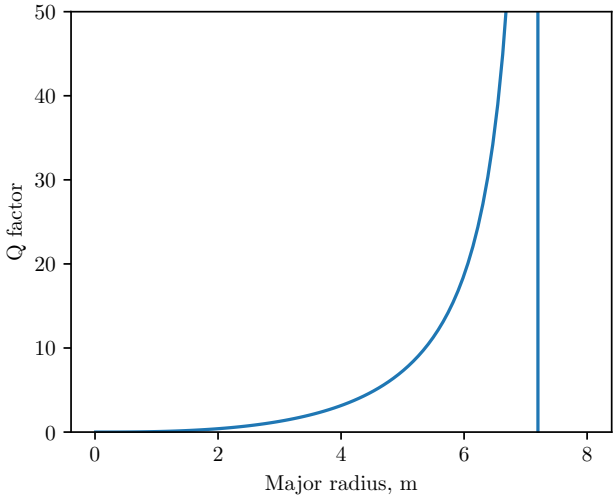

FIGURE 2.4: Fusion gain Q as a function of major radius R_0.

energy source, the very early step of plasma initiation in a tokamak has only been explored more in-depth in recent years. Much of the underlying physics is in the process of discovery and not well understood as of yet. The following sections will then focus on the prior works and the physics related to plasma breakdown avalanche theory.

2.2 Tokamak plasma initiation theory

Creation of plasma within the tokamak vacuum vessel is mainly through the ohmic heating (OH) startup [35, 36]. Additionally, the plasma current ramp from OH startup can be accelerated through electron cyclotron heating (ECH) assisted methods [37, 38], which creates pre-ionised electrons prior to the OH startup scenario. OH startup relies on the theory of Townsend's breakdown avalanche. The theory is based on a simple 1D experiment (a parallel plate capacitor experiment) on the electric discharge and it exerts a dominant influence in shaping the plasma initiation physics. Most notably, the exponential cascade of the electron from discharge in a tokamak is extrapolated from the theory. Such approximation is briefly explored here, starting with the expression of Townsend's breakdown model expression given as

$$\frac{I}{I_0} = \frac{e^{\alpha d}}{1 - \gamma(e^{\alpha d} - 1)}. \tag{2.10}$$

Assuming that the electric current of the initial free electron is denoted by I_0, the current I is then the amplified current measured at a distance of d. The amplification factor is

exponential and governed by the first Townsend coefficient α (which can be interpreted as the number of ionisations per unit length traveled by electron) and γ describes the secondary electron emissions from positive ion and surface impact ionisation. A further simplification is made to Eq. 2.10, such that the secondary electron emissions is ignored when considering only the areas in the vicinity of the torus' minor axis (where the breakdown region is). The simplification can be justified as the main bulk of the created plasma arises from electron-neutral impact ionisation during the very early phases, since secondary electron emission only occurs after ion confinement time scale τ_{ion} has elapsed (which is approximately 2 orders of magnitude larger than the electron confinement time [17]). This yields

$$\frac{I}{I_0} = e^{\alpha d}. \tag{2.11}$$

The α parameter can be derived analytically, by considering the electrons that have reached the ionisation energy (due to acceleration from the electric field with a strength of E), their corresponding mean free path at a given operating pressure p as well as the probability of collision with the help of known cross sections. This gives the expression of

$$\alpha = Ap \exp\left(-\frac{Bp}{E}\right), \tag{2.12}$$

with A and B constants obtained by experimental fitting [39]. For the work presented here, the neutral target is purely hydrogen molecules, so $A = 3.83\,\text{m}^{-1}\,\text{Pa}^{-1}$ and $B = 93.6\,\text{V}\,\text{m}^{-1}\,\text{Pa}^{-1}$ would normally be used to predict the current growth. The required breakdown voltage that is conducive for Townsend avalanche (satisfying $\alpha d > 1$) then follows from Eq. 2.11, resulting in the Paschen curve, expressed as

$$V_{\text{BD}} = \frac{Bpd}{\ln(Apd)}. \tag{2.13}$$

Fig. 2.5 shows a minimum H_2 breakdown voltage of approximately $V_{\text{BD}} = 66.43\,\text{V}$ at $pd \approx 0.71\,\text{Pa}\,\text{m}$. In order to solve for the required minimal travel distance of confined electrons (d_{BD}) in a tokamak, Eq. 2.13 is recast into breakdown electric field

$$E_{\text{BD}} = \frac{Bp}{\ln(Apd_{\text{BD}})}.$$

ITER is planned to operate at a prefill pressure of 1 mPa and toroidal electric field strength of $E_{\text{loop}} \sim 0.3\,\text{V}\,\text{m}^{-1}$. Therefore, $E_{\text{BD}} < E_{\text{loop}}$ must be respected in order for ITER to sustain a breakdown avalanche for an ohmic heating (OH) breakdown scenario. For the condition to be true, electrons must be ensured to have a minimum confined distance (can be interpreted as connection length L) of $d_{\text{BD}} \approx 357\,\text{m}$ [18]. One should realise that this estimate is purely extrapolating from a 1D formulation of Eq. 2.11, the

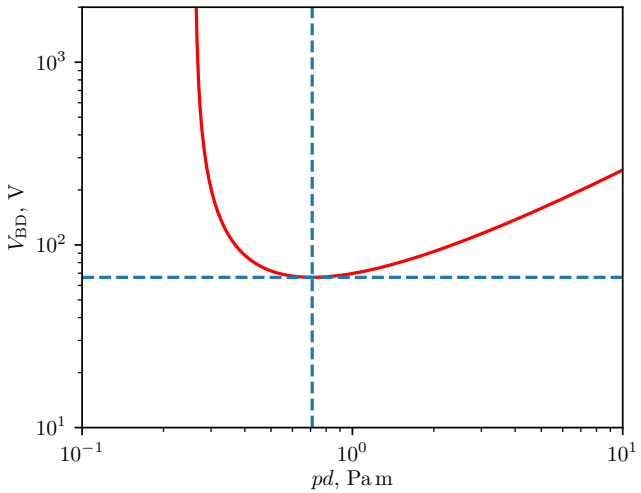

FIGURE 2.5: H_2 Paschen curve, calculated with ITER's operating prefill pressure of 1 mPa.

reality will deviate from this proposed connection length due to geometrical considerations and the unavoidable magnetic stray field during the tokamak startup phase.

Papoular provided a theoretical framework to describe the rate of plasma current rise, considering the balance between Townsend breakdown avalanche and losses [40]. Assuming that the tokamak operates at $E/p \gtrsim 100\,\mathrm{V\,Torr^{-1}\,cm^{-1}}$, the exponential growth of the current is proportional to α and given as

$$\alpha \simeq 2.5p. \tag{2.14}$$

The electron's parallel drift velocity is also predicted via extrapolation from low E/p data and it is suggested to settle at

$$V_\mathrm{e} \simeq 3.5 \times 10^5 E/p. \tag{2.15}$$

Papoular made a conjecture here that the electron population is unable to accelerate beyond 10 eV due to continuous energy loss via ionisation.

As mentioned previously, the growth rate of charged particles from the Townsend avalanche is damped by various other loss channels experienced by the electrons. One such loss is through diffusion, caused by the random scattering of electrons by background neutrals.

Papoular proposed that the diffusion loss rate $\dot{n}_\mathrm{e}$ is given as

$$\dot{n}_\mathrm{e} = \frac{D_\perp}{a^2}, \tag{2.16}$$

where

$$\begin{aligned} D_\perp &\approx \frac{D_0}{(\omega_c t_m)^2} \\ t_m &= \frac{\lambda}{\bar{w}} \approx \frac{1}{\sigma_{\mathrm{scat.}} n_\mathrm{e} \bar{w}} \\ D_0 &= \frac{\bar{w}\lambda}{3} \end{aligned}$$

a is referring to the torus' minor radius, $\bar{w}$ the electron thermal velocity magnitude (the velocity excluding the parallel component), λ the electron's mean free path, $\sigma_{\mathrm{scat.}}$ the electron neutral scattering cross section, ω_c the gyrofrequency and D_0 the diffusion coefficient in the absence of magnetic field. t_m is subsequently the mean time between collisions. One can interpret Eq. 2.16 as the average time scale for electrons to diffuse radially away from the minor axis of the torus, covering a distance of a.

Losses due to transverse drift are also considered and given as the time required for an electron to transversely drift beyond the torus' minor radius. A slight but important difference between the diffusion loss and transverse drift loss is that, diffusion loss is purely from random scattering, while transverse drift loss is the sideways drift velocity v_d of the electron as it gyrates along the toroidal B field. Finally, Papoular also discussed the contribution of vertical magnetic stray field $\mathbf{B}_\mathrm{z}$, inducing a drift velocity v_z causing the loss of electrons. Expression for both v_d and v_z is given as

$$\begin{aligned} v_\mathrm{d} &= \frac{1}{R_0 \omega_c} \left(\frac{1}{2} \|\mathbf{v}_\perp\|^2 + \|\mathbf{v}_\parallel\|^2 \right) \\ v_\mathrm{z} &= \mathbf{v}_\parallel \times \frac{\mathbf{B}_\mathrm{z}}{\|\mathbf{B}\|}. \end{aligned}$$

The associated loss time is subsequently

$$\begin{aligned} \tau_\mathrm{d} &= \frac{a}{v_\mathrm{d}} \\ \tau_\mathrm{z} &= \frac{a}{v_\mathrm{z}}, \end{aligned} \tag{2.17}$$

and can be interpreted as the time for electrons to drift a distance of a from the minor axis of the torus. Papoular acknowledged that the proposed formulations make use of assumptions to facilitate an early understanding of plasma initiation physics. At the time of Papoular's original publication, verification of the proposed model with experiments wasn't feasible due to a lack of comparable results.

2.3 Tokamak experimental considerations

The criteria to sustain breakdown avalanche in tokamak is shown to be dependent on the connection length L (interpreted as d_{BD} from given minimum V_{BD} in Eq. 2.13). In a tokamak setting, L is a function of the toroidal magnetic field strength B_ϕ. Mueller [17] states that connection length can be expressed as

$$L \sim \frac{aB_\phi}{\langle \mathbf{B}_z \rangle}, \tag{2.18}$$

where a is the transverse length to the vacuum vessel wall and $\langle \mathbf{B}_z \rangle$ refers to the average magnetic stray field. Even though it seems that one can come up with a prediction of the current amplification with Eq. 2.18 and Eq. 2.11, the result is quite simplistic and will not be able to fully describe the breakdown phase as the equations are inherently 1D approximations.

However, such formulation can help provide insight into the tokamak plasma initiation process even with the simplifying assumptions considered. Lloyd *et al.* [41] studied the impact of the discussed variables (p, $\mathbf{B}_z$, loop voltage V_{loop} etc.) on the breakdown duration in the DIII-D tokamak. A commonly used criterion to decide the end of the breakdown phase of plasma initiation is when the electron-ion Coulomb collision dominates over electron-neutral collision frequency. It was demonstrated at the prefill pressure of approximately 5.2 mPa, having a higher V_{loop} (subsequently higher toroidal electric field) increases the plasma current growth rate in an ohmic heating startup scenario. The breakdown duration shows an exponentially decreasing trend as a direct result of raising the prescribed V_{loop}.

It was also demonstrated that there is an optimal prefill pressure range that gives the shortest breakdown duration. One could surmise that the breakdown process struggles to start when p is excessive due to high collisional drag experienced by the electron, unable to freely accelerate to ionising energy threshold. This upward trend in breakdown duration begins at approximately 4.3 mPa and higher. The opposite extreme of having low pressure (below $\sim$2.1 mPa) also has an adverse effect on the breakdown process, due to the lack of background neutral molecules for electron-neutral impact ionisation to occur.

Another aspect that was studied is the impact of magnetic stray field strength $\mathbf{B}_z$ on breakdown duration. It is this aspect of the study that showed the most difference between pure OH startup and ECH-assisted startup, with ECH startup being least affected by stray field and achieving consistently shorter breakdown duration than OH. However, the study of OH startup proves to be more revealing. It was shown that the

breakdown duration is demonstrably shorter for low $\mathbf{B}_z$ values.

As important as Lloyd's findings were, attempting to contextualize the findings in terms of Townsend's breakdown theory necessarily simplifies the experimental results into the framework of the 1D model. The final analytical expressions follow closely with the model proposed by Papoular's publication. For example, the drift velocity expression reported in Lloyd's is similar to Eq. 2.15 which is

$$V_\mathrm{e} = \eta E/p,$$

with η denoting a derived constant. The ionisation rate can then be estimated from this expression as $\tau_\mathrm{ion}^{-1} = \alpha V_\mathrm{e}$. Similar treatment is performed on the loss rate due to drifts as discussed in Papoular's publication. Therefore, Lloyd came to the conclusion that the net current growth rate over time is adequately described by Townsend theory. The growth rate is subsequently a balance of τ_ion^{-1} and the tweaked expressions of Eq. 2.17 (with added considerations for the operating parameters of specific tokamak device).

The work by Lloyd and Papoular laid the groundwork for plasma breakdown analysis for later tokamak devices. Example studies were carried out in different capacities and on various devices, De Vries *et al.* performed similar analysis on JET-ILW [42] and Belyakov *et al.* conducted a study with a 2D simulation code which Lloyd previously worked on, providing information on various time evolution of physical variables on T-15 tokamak during the breakdown phase [43]. While the relationship between tokamak operating parameters and the breakdown duration has been established, there is a lack of detailed understanding of breakdown physics in much smaller timescales (below ms scale). Detection of current ramp-up in experimental tokamak is usually already in the order of kA, which the early development of charged particle populations is simply glossed over. Questions such as the electron velocity distribution function in the very early phase were never answered. The difficult issues of runaway electrons and shaping of the plasma column were insufficiently explored.

There are more recent numerical studies done on the topic of plasma initiation as a result of the advancement in the field of high-performance computing. The next section offers a brief recounting of such works.

2.4 Recent numerical studies

Jiang *et al.* conducted a simplistic numerical study of the tokamak breakdown phase in an attempt to answer the question if ITER-like tokamak will be able to achieve breakdown with only ohmic heating [36]. While strong assumptions were made in the study, it demonstrated the feasibility of simulating the current amplification via Monte-Carlo collision instead of relying directly on Townsend theory. Among the list of assumptions, the most notable ones are the treatment of the tokamak as an infinite-length cylinder volume without proper particle loss mechanism, as well as using argon cross section instead of H_2 molecules.

Yoo *et al.* developed the BREAK simulation code (a 2D PIC-MCC code) that uses gyro-averaging in the particle drift description. Implicit time stepping method is also used within the simulation code [44]. The BREAK code subsequently showed that $E \times B$ mixing avalanche begins at $n_e \approx 10^{13}\,\mathrm{m}^{-3}$ and serves to damp the current growth rate during the latter stage of the avalanche process [45].

Hoppe *et al.* developed a wholly different numerical methodology to simulate the plasma breakdown and creation of runaway electrons [46]. The method describes the particle balance and current ramp-up through sets of conservation governing equations. The specific description of ion-electron balance is done through the interaction exchange rate from the Atomic Data and Analysis Structure (ADAS) database. Runaway electron density is then captured by utilising several semi-analytical expressions which compute the balance between free electron creation and loss rate of highly energetic electrons.

While the mentioned studies provided new insights into the various aspects of the plasma initiation process, a highly detailed study of the current growth at a high timescale resolution has never been attempted before. This could potentially improve the understanding of the various charged particles' physical time evolution when the drift behaviour is mainly from the interaction with background fields and neutral scattering.

2.5 0D ionisation fraction growth rate

As mentioned previously, detailed studies of electrons' energy and velocity distribution and their growth rate in the early ms are lacking. The equations proposed by Papoular (Eq. 2.14, 2.15, 2.16) are commonly used to form a prediction of the observables. The work by De Vries *et al.* formulated an equation that describes a net growth rate that is

inclusive of the losses. The equation is given as

$$\frac{1}{f_\mathrm{i}}\frac{\mathrm{d}f_\mathrm{i}}{\mathrm{d}t} = \frac{1}{n_\mathrm{e}}\frac{\mathrm{d}n_\mathrm{e}}{\mathrm{d}t} = \nu_\mathrm{ion} - \nu_\mathrm{loss} = \alpha V_\mathrm{e} - \frac{V_\mathrm{e}}{L}, \tag{2.19}$$

f_i denotes the ionisation fraction of the prefill gas, n_e the electron number density; ν_ion and ν_loss referring to the rate of electron growth (due to ionisation) and electron loss respectively, α denoting the first Townsend's coefficient, V_e describing the electron drift velocity and finally the connection length experienced by electrons represented by L. An interpretation of Eq. 2.19 is that the ionisation fraction over time is a balance between ionisation rate (due to electron-neutral impact ionisation) and loss rate of runaway electrons (always assuming that the electrons will leave the domain after travelling a distance of L). The first Townsend coefficient α is obtained as a function of E/p in Eq. 2.12.

An analytically derived value of V_e is then derived from a few simplifications. First, is the assumption that the electron drift velocity will eventually settle to a constant, and this constant is achieved due to the force balance between acceleration and collisional drag, expressed as

$$F_\mathrm{acc} = F_\mathrm{drag}. \tag{2.20}$$

The expression of $F_\mathrm{acc} = eE$ holds when the electric field is the only acceleration contribution experienced by electrons. The expression for F_drag then arises from the assumption that the majority of the electron populations have less than 20 eV kinetic energy and the considered collision cross section is only the dominant elastic scattering cross section. Tawara *et al.* provided a fitting function for the elastic scattering cross section as a function of electron kinetic energy W_e given as

$$\sigma_\mathrm{elastic} = \frac{1.75\times10^{-16}}{(W_\mathrm{e}^{1.5}+750)\sqrt{W_\mathrm{e}}}.$$

As the electron energy remains below the threshold of 20 eV, the following approximation

$$\sigma_\mathrm{elastic} \propto \frac{1}{\sqrt{W_\mathrm{e}}} \sim \frac{1}{V_\mathrm{e}}$$

holds and the drag force can be expressed as a function of elastic scattering collision frequency. The expression is then

$$\begin{aligned} F_\mathrm{drag} &= m_\mathrm{e}V_\mathrm{e}\nu_\mathrm{elastic} \\ &= m_\mathrm{e}V_\mathrm{e}^2 n\sigma_\mathrm{elastic} \\ &\sim \mathcal{C}m_\mathrm{e}V_\mathrm{e}n, \end{aligned} \tag{2.21}$$

where $\mathcal{C}$ is the coefficient of the fitting function by Tawara *et al.*, m_e is the electron mass and n is the neutral number density which can be expressed from the ideal gas equation. Substituting Eq. 2.21 into Eq. 2.20, the expression is then

$$eE \sim \mathcal{C} m_\mathrm{e} V_\mathrm{e} n$$
$$eE \sim \frac{p}{k_\mathrm{B} T} \mathcal{C} m_\mathrm{e} V_\mathrm{e}.$$

The expected V_e that fulfills the force balance is then given as

$$V_\mathrm{e} \sim \frac{e k_\mathrm{B} T}{m_\mathrm{e} \mathcal{C}} \frac{E}{p}. \tag{2.22}$$

The expression above is commonly reduced to a function of E and p by fixing the temperature of the neutral gas, which then coincides with the functional dependence of α parameter described in Eq. 2.12. Lastly, the connection length L is commonly assumed to be 1 km for an ITER-like tokamak, it is the distance traveled by electrons before they collide with the plasma-facing components in the vacuum vessel. f_i can now be approximated from the 0-dimensional (0D) model with all the unknown variables defined. The core assumption remains that, the main mechanism by which the charged particle population increases can be described by the Townsend discharge process [17] during the very early phase of plasma initiation in ITER-like tokamak. However, instead of an equation that purely considers the ionisation (equally, electron population) growth rate prescribed by Townsend's first coefficient α, the growth rate is also dampened by the runaway electron population.

2.6 Research motivation and goals

Eq. 2.19 is a 0D description of a Townsend discharge in a tokamak setting, since it uses the known first Townsend coefficient α to determine the rate of ionisation without concern for the spatial geometry of the considered domain [18]. The connection length L measure is also given as a single assumed length, which is in contrast with the length found even within a tokamak device's Scrape-Off Layer (SOL) which can range between tens of meters up to the range of kilometers [47, 48]. Additionally, the force balance in Eq. 2.21 implies that the derived V_e is an averaged electron velocity purely along the acceleration field vector. The V_e measure in a 3-dimensional (3D) space is different since the scattering events introduce velocity components perpendicular to the acceleration field vector. The 0D formulation might introduce an overestimation of the collisional drag force experienced by the electrons. As it stands, the α variable is the most well-defined value among the three discussed unknowns in Eq. 2.19, since it is rooted in experimentally fitted values. Due to the listed differences between the 0D equation and

the 3D settings, it is expected that both scenarios will produce notable deviations in ionisation fraction growth rate and V_e.

There is now a need to quantify the differences in the results obtained via the 0D equation and 3D simulation model, especially in the prediction of plasma initiation in larger-scale tokamak like ITER. A larger vacuum vessel volume along with unavoidable magnetic stray fields (primarily from the poloidal magnetic field) during the plasma initiation phase will introduce a non-negligible runaway electron population. In this situation, a 0D model would be unsuitable for the approximation of runaway electrons, since runaways are heavily dependent on electrons' interaction with complex three-dimensional field geometry. Based on these considerations, there is a motivation to perform a comparative study of ionisation growth rate between the 0D approximation and the 3D simulation (perhaps providing insight into the main factors that determine the global growth rate in the tokamak plasma initiation process).

The study of space charge distribution along the tokamak is also a subject of interest. Establishing a relationship between the observed charge concentration on the poloidal plane to various external factors will provide a better-informed decision on designing the scenario of plasma initiation. Before the loop current in the tokamak reaches the threshold which forms magnetic flux tubes, the charged particles will not be properly confined and losses are expected from the prescribed magnetic stray fields. Through the study, key criteria such as the location of the first closed magnetic flux surface formations or the time scale at which Coulomb collision dominates can be identified. Another area of study would be the formation of charge separation (or lack thereof) due to charge interaction with background field and collision interactions. The underlying physics of the development of discussed observables can be understood through numerical studies.

The influence of charged particles' spatial distribution also drives the need for the development of a 3D simulation model. There was a consideration to conduct the simulations in a simplified 2D domain, taking advantage of the toroidally symmetric field configurations in a tokamak. However, due to the sparse charged particle distribution, the charged particles are strongly coupled by the self-consistent fields. Full representation of the spatial distances between charged particles becomes an important consideration in accurately resolving the charged particle motion in the early plasma initiation phase. A fully three-dimensional (3D) model will be able to simulate the complex charged particle interactions, as well as particles-fields interaction during Townsend avalanches.

During plasma initiation, the plasma is far from thermal equilibrium, so the electron velocity distribution along the toroidal direction is likely to deviate from the often-assumed

Maxwellian distribution. Several factors can influence the resulting velocity distribution. Electrons that carry kinetic energy in the order of 100 eV experience energy loss predominantly due to impact excitation or ionisation of neutral molecules. During the plasma breakdown phase, there will be an exponential increase of low energy electron population from ionisation events, skewing the distribution toward the low-velocity end. Additionally, there will be a small population of electrons that eventually gain energy above 1 keV, beyond which the cross sections fall off exponentially, allowing such electrons to continuously gain energy until they collide with plasma-facing components of the vacuum vessel. These energetic electrons form the high-velocity tail of the velocity distribution. By continuously recording the electron velocity distribution parallel to the toroidal direction, a description of the distribution during the initiation phase can be obtained. Comparison between the perpendicular and parallel velocity distribution will also provide insight into the drift mechanics as the charges travel in the toroidal geometry.

The current task is to develop a numerical model that can achieve the stated research goals. Fortunately, Simulation and Data Laboratory Plasma Physics in Forschungszentrum Jülich has an existing Coulomb potential solver that was developed in-house. The solver will be used to resolve the Coulomb forces experienced by charged particles throughout the simulation. All other aspects of the simulation (electric and magnetic field calculations, particle motion integration, neutral scattering and ionisations, etc.) will have to be developed. The next chapter focuses on the all major aspects of the simulation code that is implemented specifically for this study.

Chapter 3

Implementation of numerical model

In order to meet the stated research goals in Sec. 2.6, a numerical model that is capable of modelling charged particle motion in 3D geometry, while reproducing the expected ionisation growth rates consistent with experimental measurements is needed. The most important consideration is the type of plasma modelling that the numerical simulation will use. Magnetohydrodynamic (MHD) models, kinetic models such as the Vlasov-Maxwell-Fokker-Planck system and particles-based methods like the Barnes-Hut algorithm or Fast Multipole Method (FMM) are among the commonly known plasma modelling methodologies. A discussion of the thought process behind the chosen method for this study is detailed in Sec. 3.1. This is then followed by the details of the numerical model's various aspects, such as the Coulomb solver (Sec. 3.2), the equation of motion integrator (Sec. 3.3), electron-neutral scattering models (Sec. 3.4) and finally the electric and magnetic field calculations that were implemented.

3.1 Selection of plasma model

As it was mentioned previously, the simulated plasma regime is far from thermal equilibrium. This already eliminated the use of the magnetohydrodynamic (MHD) model. The choice is then between the particles-based approach and the kinetic equation. Considering the goal of studying the ionisation growth rate in a tokamak scenario, it is clear that impact ionisation between electron-neutral is a key component to be simulated. Both methods of plasma modelling can sufficiently capture the ionisation rate by incorporating electron-neutral cross sections in the computation of collision frequencies, thus recording the ionisation over time as an emergent behaviour (arising from convolution of

cross sections and electron energy distribution function). More specifically, such collision interaction in particle-based approach can be computed in a straightforward manner for every simulated charge by utilising the particles' energy. The kinetic formulation can achieve the same goal by incorporating impact cross sections in its collision operator.

It is also possible for both particle-based and kinetic equation methods to study the time evolution of electron velocity distribution in 3D. The numerical implementation to capture such information is rather straightforward with the particle-based method. This is simply done by recording the velocities of all simulated charges and reproducing velocity histograms with respect to the aligned direction in the torus (either along the toroidal or poloidal direction). Kinetic formulations are able to account for such velocity distributions, provided that the distribution function f includes the description of the momentum space distribution in both the aforementioned directions, which can then be updated as the simulation progresses in time. However, this requires discretisations in both space and velocities which are more computationally involved compared to a particle-based method. Finally, the goal of studying the charge distribution in space can equally be sufficiently carried out by either of the models, provided that the collision operator of kinetic equation includes careful considerations in modelling the scattering angles during collision events as well. Computation of electromagnetic fields can be computed with methods that fit best for each of the two methods, and the charged particles' interaction with the fields should be satisfied as long as Maxwell's equations are solved in conjunction.

Finally, an important unknown to consider is the initial number density of charges in the simulation. Since this work aims to understand if Townsend breakdown avalanche can occur in ITER-like tokamak conditions starting from purely unionised gas without the aid of auxiliary heating (electron/ion cyclotron resonance heating and neutral beam injection etc.), the simulation should ideally start with approximately $\sim 10\,\mathrm{m}^{-3}$ electrons. At this stage, the major challenge is the proper representation of phase space distribution of charges. The planned dimension of the simulated tokamak breakdown region will have a major radius of 5.8 m and a minor radius of 1.75 m. Should the simulated domain be discretised in the length scale of centimetres, there will be a large number of cells that carry no charged particles. This is unfavourable to kinetic equations, as the distribution function cannot properly represent the local charges' phase space distribution (which can be null in some discretised cells during initial time). Particle-based approach is therefore more appropriate for the regime of study, even if the exponentially increasing computational cost can potentially be a problem at a later stage.

3.1.1 General overview of particle-based models

The justification for the usage of particle-based methods was made and this section now focuses on a general description of the method itself. This class of method involve the integration of equation of motion for each individual charged particle within the system, subjected to the influence of electromagnetic fields and collisions, either between charged particles or interactions with neutrals. This method usually employs an explicit time-stepping scheme to integrate the equation of motion as it marches forward in time. One commonly used time-stepping algorithm is the Boris pusher [49], a rather direct implementation of the leapfrog algorithm which is computationally economical. Although it is not symplectic by nature, it does a sufficient job of preserving the simulated system's phase space over time (which provides conservation of momentum and energy of the system). The Boris pusher solves a generic equation of motion shown in Eq. 3.1, which describes the forces experienced by charged particles within a magnetised domain throughout the simulation.

$$m\frac{\mathrm{d}\mathbf{v}}{\mathrm{d}t} = q(\mathbf{E} + \mathbf{v} \times \mathbf{B}) \tag{3.1}$$

The equation of motion depends on the mass and charge of the charged particle m, q, the charged particle's velocity $\mathbf{v}$; $\mathbf{E}$ and $\mathbf{B}$ each representing the experienced electric and magnetic field respectively. The electromagnetic fields are solved via Maxwell's equations, given as

$$\begin{aligned} \nabla \cdot \mathbf{E} &= \frac{\rho_\mathrm{v}}{\varepsilon_0} \\ \nabla \cdot \mathbf{B} &= 0 \\ \nabla \times \mathbf{E} &= -\frac{\partial \mathbf{B}}{\partial t} \\ \nabla \times \mathbf{B} &= \mu_0 \left(\mathbf{J} + \varepsilon_0 \frac{\partial \mathbf{E}}{\partial t} \right). \end{aligned} \tag{3.2}$$

The set of Maxwell's equations is not commonly solved concurrently as the coupling between $\mathbf{E}$ and $\mathbf{B}$ is computationally expensive to solve. Instead, $\mathbf{E}$ and $\mathbf{B}$ are often times computed separately. Darwin's approximation to Maxwell's equation is one such method to decouple the two fields. Collision interactions between free electrons and background neutrals can also be explicitly simulated (assuming that the neutrals are homogeneously distributed and static), often via prescribed collision frequencies as a function of neutral number density, specific cross sections and the electron's energy. Collisional drags experienced by electrons will then arise as an aggregate of a few factors, such as scattered angles with respect to the experienced acceleration field (often prescribed static background electric field) and the electron energy loss due to excitation or ionisation of neutrals.

The particle-based method has a few options to numerically resolve the **E** and **B** fields, Particle-in-Cell (PIC) and the mesh-free algorithms are the typical choices. Particle-in-Cell method generally follows the computational loop, beginning from interpolating the electromagnetic field at the grid vertices to the individual particles bounded by the cell, followed by the pusher algorithm that updates the particles' velocity and position, then projection of the resulting current and charge density to the nearest cell grid points and finally solving Maxwell's equation to obtain **E** and **B** from the projected values for the next time step loop. Before such a loop can begin, the simulation domain is discretised into cells where **E** and **B** are stored on the cell vertices. There are numerical details to every step of the computational loop. For example, there is a freedom of choice in the shape function used to interpolate the field variables to the particles [50]. Aside from that, one could choose to solve Maxwell-Ampère and Maxwell-Faraday equations to compute the field variables for the next time step, instead of the set of Maxwell's equation. The projection of components of **E** and **B** from particles to 3D cartesian grids can also be done with the Yee lattice [51]. The assignment of the vector components in cubic grid is derived from expressing the **E** and **B** in its cartesian components, realising that not all the grid points has to carry all components of either **E** and **B** in order to compute the rate of change of electric displacement field **D** and magnetic field **B**. One has to be aware of the possibility of numerical heating and numerically induced instabilities arising from the spatial aliasing of defined grid structure in PIC algorithms [52–54]. It has also been demonstrated that numerical heating occurs in simulations that couples PIC with binary Monte-Carlo collisions [55].

Mesh-free method side-steps the unphysical effects arising from the grid definition. The biggest drawback to the mesh-free method is the immense computational cost and it is usually not feasible to numerically simulate a system with a large number of particles. Take a simulation which resolves the electrostatic potentials between charged particles, a straightforward potential evaluations of n particles introduces a computational cost that scales in the order of $\mathcal{O}(n^2)$. The expensive nature of particle-based methods often limits the size of the particle system.

In order to address the issue, two commonly used methods are the fast multipole method (FMM) [56] and the treecode method (Barnes-Hut algorithm [57] for example). While both methods involve the construction of the tree structure that establishes parent-child relation between particles, summation of potential contributions is different. FMM method has a computational cost of $\mathcal{O}(n)$, while the Barnes-Hut algorithm's computational cost scales with $\mathcal{O}(n \log n)$. The difference in cost scaling between the two methods is due to Barnes-Hut computes particle-particle and particle-cell interactions,

while FMM also computes cell-cell interactions (between parent and daughter cells) during the force computation step [58, 59]. Another feature of FMM is that it is better suited for a uniform distribution of particles if no additional adaptive treatment is given [60], while Barnes-Hut algorithm is inherently adaptive as the simulation domain is decomposed until each particle is its own leaf in the tree structure. Darwin's approximation is commonly used to compute the self-consistent magnetic fields [61, 62] instead. It is entirely possible to carry out n-body simulation without spatial discretisation, since the net force experienced by charged particles is calculated and stored by each particle at every time step. Since the n-body simulation method is a fundamental description of a charged particle system, the resulting system of equations is straightforward with minimal in-built assumptions. This has the added advantage that such a method can be applied to a wide range of plasma physics applications.

The computation of self-consistent electric field $\mathbf{E}$ in this study is handled by a parallel implementation of the Barnes-Hut algorithm. A brief description of the numerical solver will be given in the following section.

3.2 Pretty Efficient Parallel Coulomb solver

The formation of rarefied magnetised plasma from neutral prefill gas is the main focus of this simulation study. While the resulting electric field due to space charge separation is initially negligible, it is still expected to have an appreciable influence on particle trajectories during the early phases of plasma initiation. For this reason, a highly parallelised numerical solver for electrostatic potential is still a useful tool to have. Comparison of the magnitude of background electric field and the field due to charge distribution can provide insight and help extrapolate the threshold when Coulomb collisions become dominant interaction among the charged particles. Eq. 2.19 fixed at temperature of $373.15\,\mathrm{K}$, $E/p = 300\,\mathrm{V\,m^{-1}\,Pa^{-1}}$ and $p = 2\,\mathrm{mPa}$ can be used to show that the electron number density will span from $10\,\mathrm{m^{-3}}$ to above $10^8\,\mathrm{m^{-3}}$ in $\sim 1.5\,\mathrm{ms}$. A numerical solver that can efficiently utilise the supercomputing nodes will better cope with the large number of particles further in simulation time.

Taking all the above considerations in mind, the Pretty Efficient Parallel Coulomb-solver (PEPC), a hybrid parallel (rank-thread) implementation of Barnes-Hut algorithm developed at the Jülich Supercomputing Centre [63] is appropriate to be the main tool for the calculation of collective Coulomb forces. The core of the PEPC code is divided into three parts: a load-balancing distribution of particles to participating MPI ranks, the construction of a data tree of simulated charges and associated multipole moments and

finally the force calculation via a tree traversal [64]. PEPC adopts an implementation strategy proposed by Warren and Salmon [65], a hashed oct tree algorithm, with the choice of either Hilbert or Morton ('Z') space-filling curves to map particle's coordinates to unique keys. The sorting of the assigned keys ensures the spatial 'closeness' of particles and assists in the distribution of particles to participating MPI ranks. This is done to avoid unnecessary communication between processors and heavy duplication of local tree data during the tree construction and traversal phase of Barnes-Hut algorithm. Details of the implementation can be found in the work of Gibbon *et al.* [66] and Winkel *et al.* [64].

Simulations are performed on two supercomputers in Forschungszentrum Jülich, namely the Jureca DC and the Jureca Booster partitions [67]. Fig. 3.1 shows the strong scaling of the PEPC solver running on both machines. The plots displayed an approximately inverse linear scaling on wall-clock time as the number of cores is increased on both machines (shorter wall time with larger number of cores), demonstrating good parallelisation efficiency of the PEPC solver. This behaviour is important to handle large number of simulated charges during the self-consistent electric field compute step. The plot on the right showed that the total compute resource (with the unit of core-hour, defined as the number of cores multiplied by hours of computation) begin to stagnate for both of the Jureca DC simulations as the number of simulated bodies per core reduces. This is most noticeable for the simulation case with 1 million particles, both scenarios of 500 and 1000 compute cores required approximately 6 core-hours to complete the simulation. This highlights the communication bottleneck between the cores and suggests that there is an optimal number of particles per rank in order for the simulation to run as efficiently as possible. As such, the number of cores requested will scale properly with the number of simulated particles to achieve reasonable runtime for each simulation case.

3.3 Gyrophase corrected Boris pusher algorithm

In order to integrate Eq. 3.1 and compute the updated charged particle velocities, a numerical integrator that has a suitable bound on the energy conservation error when both electric and magnetic fields are present has to be selected. The integrator should also avoid unbounded error accumulation over an arbitrarily large number of time steps. A very commonly used numerical scheme is the Boris scheme [49]. Although it is not a symplectic integrator, it does conserve phase space volume as well as exhibiting a global bounded energy error [68]. However, it is also well-known that the scheme's phase error is unbounded. The phase error arises purely from the treatment of the rotation phase

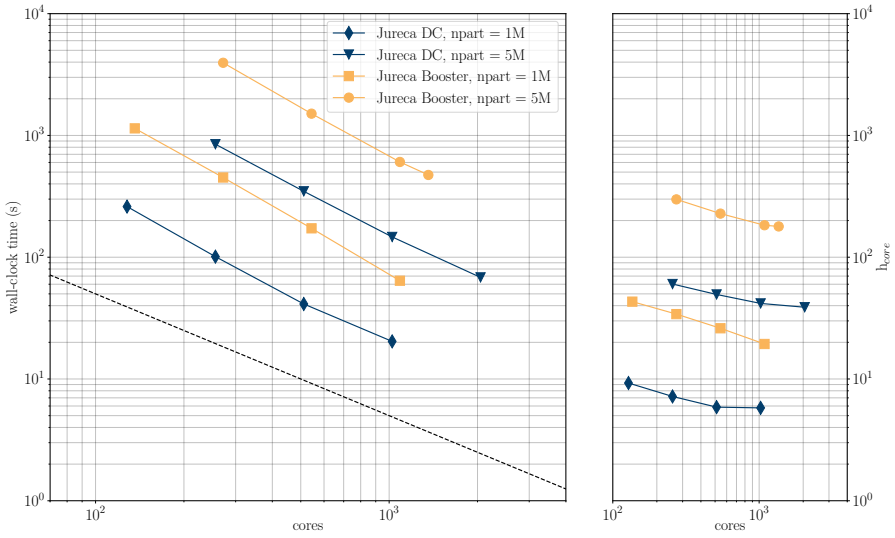

FIGURE 3.1: Left: Strong scaling of PEPC on the Jureca-DC and Jureca booster partitions for a problem size of 10^6 and 5×10^6 particles taken from the tokamak Townsend discharge scenario run for 100 timesteps, without I/O. All accompanying physics and in-development merging algorithm are included. Right: The corresponding required core-hours.

as a result of the Lorentz force.

The relativistic treatment of Eq. 3.1 is repeated here for the sake of convenience, which is

$$\frac{\mathrm{d}\mathbf{u}}{\mathrm{d}t} = \frac{q}{m}(\mathbf{E} + \mathbf{v} \times \mathbf{B}) \tag{3.3}$$

with $\mathbf{u} = \gamma\mathbf{v}$ the relativistic velocity vector, $\gamma = 1/\sqrt{1 - \|\mathbf{v}\|^2/c^2}$ and c denoting speed of light respectively. Numerical evaluation of the acceleration is performed by first discretising Eq. 3.1 in time t with central differences, which gives

$$\frac{\mathbf{u}_{t+\frac{\Delta t}{2}} - \mathbf{u}_{t-\frac{\Delta t}{2}}}{\Delta t} = \frac{q}{m}(\mathbf{E}_t + \overline{\mathbf{v}}_t \times \mathbf{B}_t).$$

where $\overline{\mathbf{v}}_t$ is the effective velocity (commonly treated as average relativistic velocity between time $t + \frac{\Delta t}{2}$ and $t - \frac{\Delta t}{2}$), this term is not usually used as-is in the implementation. The time discretised expression is further split into linear and rotational acceleration steps shown as

$$\mathbf{u}^- = \mathbf{u}_{t-\frac{\Delta t}{2}} + \frac{q\mathbf{E}_t}{2m}\Delta t \tag{3.4}$$

$$\frac{\mathbf{u}^+ - \mathbf{u}^-}{\Delta t} = \frac{q}{m}(\overline{\mathbf{v}}_t \times \mathbf{B}_t) \tag{3.5}$$

$$\mathbf{u}_{t+\frac{\Delta t}{2}} = \mathbf{u}^{+} + \frac{q\mathbf{E}_t}{2m}\Delta t \tag{3.6}$$

Numerical treatment of Eq. 3.5 proposed by Boris is not used here. Zenitani *et al.* instead proposed an analytical solution that solves the rotation exactly [69], which is given as

$$\mathbf{u}^{+} = \mathbf{u}_{\parallel}^{-} + \left(\mathbf{u}^{-} - \mathbf{u}_{\parallel}^{-}\right)\cos\theta + \left(\mathbf{u}^{-} \times \hat{\mathbf{B}}_t\right)\sin\theta \tag{3.7}$$

with

$$\mathbf{u}_{\parallel}^{-} = \left(\mathbf{u}^{-} \cdot \hat{\mathbf{B}}_t\right)\hat{\mathbf{B}}_t$$
$$\theta = \frac{q\Delta t\sqrt{1 - \|\mathbf{v}_{t-\frac{\Delta t}{2}}\|^2/c^2}}{m}\|\mathbf{B}_t\|$$

where $\hat{\mathbf{B}}_t = \mathbf{B}_t/\|\mathbf{B}_t\|$ is the unit vector of magnetic field at time t. The computed $\mathbf{u}_{t+\frac{\Delta t}{2}}$ is then used to update the position of the particle in the next half step as

$$\mathbf{x}(t + \Delta t) = \mathbf{x}(t) + \frac{\mathbf{u}_{t+\frac{\Delta t}{2}}}{\gamma}\Delta t, \tag{3.8}$$

noting that a simplification of $\gamma = \gamma_{t+\frac{\Delta t}{2}} = \gamma_{t-\frac{\Delta t}{2}}$ is taken. Staggered update of particle velocity and position is performed by implementing Eq. 3.4, Eq. 3.7, Eq. 3.6 and finally Eq. 3.8 in succession.

There is a time step size limit associated with the Boris integration scheme if the gyro-orbit of the fast-moving electrons is to be resolved by at least 3 points. The limit is expressed as

$$\Delta t < \frac{3}{\{\omega_{\mathrm{g}}\}_{\max}} = \frac{3m_{\mathrm{e}}}{q_{\mathrm{e}}|B|_{\max}},$$

where ω_{g} is the gyro-frequency, q_{e} denotes the charge of electron and m_{e} is the electron rest mass. If the simulation is done with step size larger than Δt, the electron's motion will still be confined along the experienced magnetic field vector, but the gyroradius will not be scaled correctly and there will be an offset from the actual gyrocenter. The collision frequency between electrons and neutral molecules also imposes constraint on the time step size, so that there will only be a maximum of one collision event on average in a step. This time step size bound will be discussed in detail in Section 3.4.1.

3.4 Scattering and ionisation model

This section describes the implemented calculation of electron-neutral collision probabilities and the treatment of scattering angles during each collision. Since this work is a first attempt at studying the 3D effects of Townsend avalanche breakdown in a tokamak's

very early phase, a major simplification is made such that the ionisation channels are purely from electron-neutral impact. Three different scattering models are implemented and later compared in Ch. 5 to quantify their impact on the obtained Townsend's first coefficient α. This is crucial as it affects the ionisation growth rate. Detailed discussions on the considered electron-neutral collision cross sections will be covered in Ch. 6 and 7 respectively.

3.4.1 Collision probability

A common assumption in the treatment of electron-neutral collisions is that the neutral molecules are static and homogeneously distributed in space. This removes the need for the neutrals to be explicitly simulated and saves the computational cost enormously as only the charged particles are modeled. Decisions about when electrons undergo collisions can then be made probabilistically. The following electron collision probability does not consider charged particles (electron-electron or ion-ion) collisions, which are in principle handled implicitly by the Coulomb solver.

The mean free path l_{mfp} of an electron in a volume V of neutral gas with pressure p and temperature T is derived from the number density n of neutrals and the effective collision cross section σ (which is a function of electron energy ε), expressed as

$$l_{\text{mfp}} = \frac{1}{\sigma(\varepsilon)n} = \frac{RT}{\sigma(\varepsilon)pV}$$

where R is the ideal gas constant. The collision probability between an electron and background neutral per time step can then be expressed as a function of l_{mfp}. For an electron that has kinetic energy ε (and corresponding velocity $\mathbf{v}$), the expected time between collisions is then

$$\tau = \frac{l_{\text{mfp}}}{\|\mathbf{v}\|} = \frac{1}{\sigma(\varepsilon)n\|\mathbf{v}\|}.$$

During an interval of $\Delta t = \tau$, one would expect the electron to experience one collision. That is to say that the probability of collision is 1. The probability of electron not experiencing a collision during an interval $\Delta t < \tau$ is then

$$P(\Delta t) = 1 - \frac{\Delta t}{\tau}.$$

Let's assume that the end time of the simulation is t_{end}, and a total number of steps N_{total} is taken from initial time to t_{end}, we have $\Delta t = t_{\text{end}}/N_{\text{total}}$ and the probability of

the electron not experiencing collision at all up to t_{end} is

$$P_{\text{no coll.}} = \left(1 - \frac{\Delta t}{\tau}\right)^{N_{\text{total}}} = \left(1 - \frac{t_{\text{end}}}{N_{\text{total}}\tau}\right)^{N_{\text{total}}}.$$

Lemma 1. For every sequence of complex numbers w_n with a limit w, it is true that

$$\lim_{n\to\infty}\left(1 + \frac{w_n}{n}\right)^n = \sum_{k=0}^{\infty}\frac{w^k}{k!}.$$

From the lemma [70], $P_{\text{no coll.}}$ simplifies to

$$P_{\text{no coll.}} \approx \exp\left(-\frac{t_{\text{end}}}{\tau}\right) = \exp\left[-N_{\text{total}}\,\sigma(\varepsilon)\,n\|\mathbf{v}\|\,\Delta t\right]$$

when N_{total} approaches infinity. The probability of at least one collision up till arbitrary $N_{\text{step}} < N_{\text{total}}$ is then

$$P_{\text{coll. N}} = 1 - \exp\left[-N_{\text{step}}\,\sigma(\varepsilon)\,n\,\|\mathbf{v}\|\,\Delta t\right].$$

Finally, the probability of at least one collision between an electron with ε and $\mathbf{v}$ in one time step is then

$$P_{\text{coll.}} = 1 - \exp\left[-\sigma(\varepsilon)\,n\,\|\mathbf{v}\|\,\Delta t\right]. \tag{3.9}$$

Considering that there will be multiple different cross sections included in the simulations and each cross section will have its own collision probability, the expression is then

$$P_c = 1 - \exp\left[-\sigma_c(\varepsilon)\,n\,\|\mathbf{v}\|\,\Delta t\right] = 1 - \exp\left[-\nu_c(\varepsilon)\,\Delta t\right], \tag{3.10}$$

where $\sigma_c(\varepsilon)$ denotes the cross section for collision outcome of type c and collision frequency expression

$$\nu_c(\varepsilon) = \sigma_c(\varepsilon)\,n\,\|\mathbf{v}\| \tag{3.11}$$

is used to further simplify the Eq. 3.10. Representing the background neutrals with a simple n implies that its degree of ionisation is negligible over the time scale of this study.

In order to avoid potentially costly computation of all individual collision frequencies ν_c for every particle at every time step, H. R. Skullerud proposed the null collision method which involves defining a constant collision frequency, ν', that is large enough to encompass all possible collision outcomes over the full range of electron energy [71] in a first

step. Any measure or definition of ν' can be accepted as long as it fulfils

$$\nu' \geq \nu_{\mathrm{T}}(\varepsilon), \ \forall \varepsilon.$$

$\nu_{\mathrm{T}}(\varepsilon)$ describes the collision frequency computed from summing all considered cross sections of electron-hydrogen molecule collisions,

$$\nu_{\mathrm{T}}(\varepsilon) = n\|\mathbf{v}\| \sum_{c} \sigma_c(\varepsilon) = n\|\mathbf{v}\|\sigma_{\mathrm{T}}(\varepsilon).$$

Since it is established that ν' should always be equal or larger than $\nu_{\mathrm{T}}(\varepsilon)$, the resulting collision probability is then

$$\begin{aligned} 1 - \exp(-\nu'\Delta t) &\geq 1 - \exp(-\nu_{\mathrm{T}}(\varepsilon)\Delta t) \\ P' &\geq P(\varepsilon), \ \forall \varepsilon. \end{aligned} \tag{3.12}$$

P' denotes the collision probability calculated with ν' and $P(\varepsilon)$ refers to the actual collision probabilities computed from the energy ε carried by electron. In this set-up, a 'null collision' outcome with no real interaction between hydrogen molecule and electron is already included in ν'. This would mean that only when a random number $R_1 = [0, 1]$ fulfills $R_1 \leq P'$, proper computation of each available $\sigma_c(\varepsilon)$ is done. A second random number R_2 is then used to determine the actual collision outcome via Eq. 3.10.

This implies that choosing an overly large ν' will not impose a penalty on the computational cost, it would be the same as not applying this simplification in the first place. However, one would like to minimise the probability of 'null collision' to avoid excessive calculation of the actual P_c. A specific definition of ν' is made throughout this study, which is

$$\nu'(\varepsilon) = \sigma_{\mathrm{t.s.}}(\varepsilon)\, n\, \|\mathbf{v}\|, \tag{3.13}$$

where $\sigma_{\mathrm{t.s.}}$ refers to the total scattering cross section. This definition is made with the knowledge that the considered cross sections in the simulation cases will not fully cover all electron-neutral collision outcomes. The study mainly concerns itself with electron-hydrogen molecule scattering interactions. Many of the cross sections for H_2 metastable excitations are not considered due to negligible energy transfer from electron to H_2. Aside from that, the ignored cross sections generally have an order (or more) magnitude smaller cross section value compared to the ionisation cross sections (which is the main focus of the study). As such, the following condition always holds true

$$\sigma_{\mathrm{T}}(\varepsilon) < \sigma_{\mathrm{t.s.}}(\varepsilon).$$

Eq. 3.9 refers to the probability of at least one collision within the time span of Δt. The choice of time step size is important to ensure that only one instance of collision occurs for every charged particle in each simulation step. Vahedi *et al.* [2] gave an expression for the probability r of two or more collisions ($k \geq 2$) per time step as

$$r \sim \sum_{k=2}^{\infty} P^k = \frac{P^2}{1-P}$$

In order to have less than 1% chance for each simulated particle to have more than one collision per time step ($r < 0.01$), then Δt must necessarily be chosen to fulfil

$$\sigma_{\mathrm{T}}(\varepsilon)\, n\, \|\mathbf{v}\| \Delta t \leq 0.1. \tag{3.14}$$

3.4.2 Scattering angle

In a quasi-neutral plasma, Coulomb collisions dominate in the collisional drag force experienced by electrons. However, in the early stages of Townsend discharge, the presence of ions is scarcely felt within the medium. Most of the collision events experienced by the electrons are between electron and neutral targets and thus deserve special attention. Since the differential cross sections related to electron-hydrogen elastic scattering over the wide energy range of interest are lacking, several methods of computing the scatter angle are considered in this work. This includes a new method of scatter-angle calculation along with two others by Vahedi *et al.* [2] and Okhrimovskyy *et al.* [3] respectively.

The interaction between simulated charged particles is handled by PEPC described in Section 3.2. The transition from an elastic collision dominated phase to a primarily Coulomb collision phase in the ionisation breakdown simulation can therefore be handled seamlessly.

3.4.2.1 Random Scatter model

This newly proposed method of scattering angle treatment first divides the considered cross sections into two groups: collision outcomes that do not involve splitting of the neutral targets, and those that cause ionisation or dissociation to occur. The following description details the implementation for the first group, which applies to elastic scattering and various metastable excitations of H_2 molecules.

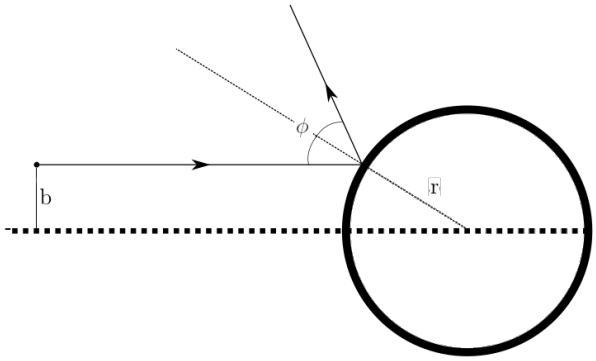

FIGURE 3.2: Simple sketch of hard sphere elastic collision model. This model can easily be extended to 3D by assuming that the neutral target is spherical, thus the azimuthal angle θ distribution is uniform.

The treatment of velocities in this scenario is rather simple and it can be illustrated with Fig. 3.2. Note that all the instances of collisions are between an electron and a neutral target. A simple assumption is made regarding the model used for collision velocity updates, which is based on a hard-sphere collision model. Another assumption is that the electron is treated as a point charge with no radius of its own. Referring to Fig. 3.2, it can be seen that the polar angle ϕ is in the range of $[0, \pi]$, which is dependent on the *impact parameter*, b. Further, for a fixed *impact parameter*, b, the azimuthal angle of approach, θ, is in the range of $[0, 2\pi]$. Since the neutral targets are not explicitly simulated, the *impact parameter* and azimuthal angle for each collision are not known. As a result, the scattered angle for electrons is determined in a random manner.

In order to ensure that the velocity vector direction is uniformly distributed over a sphere, θ and ϕ is calculated as

$$\begin{aligned} \phi &= \arccos(1 - 2R_1), \\ \theta &= 2\pi R_2 \end{aligned} \tag{3.15}$$

where R_1 and R_2 are two different random numbers in the range of [0, 1]. With the above θ and ϕ, the unit vector for velocity after collision is then

$$\hat{\mathbf{v}} = \begin{bmatrix} \sin(\phi)\cos(\theta) \\ \sin(\phi)\sin(\theta) \\ \cos(\phi) \end{bmatrix} \tag{3.16}$$

The resulting distribution of vector points on unit sphere is then shown in Fig. 3.3, seen from the side view in the x-z plane and the top view in the x-y plane. It shows an even

distribution of points over the sphere.

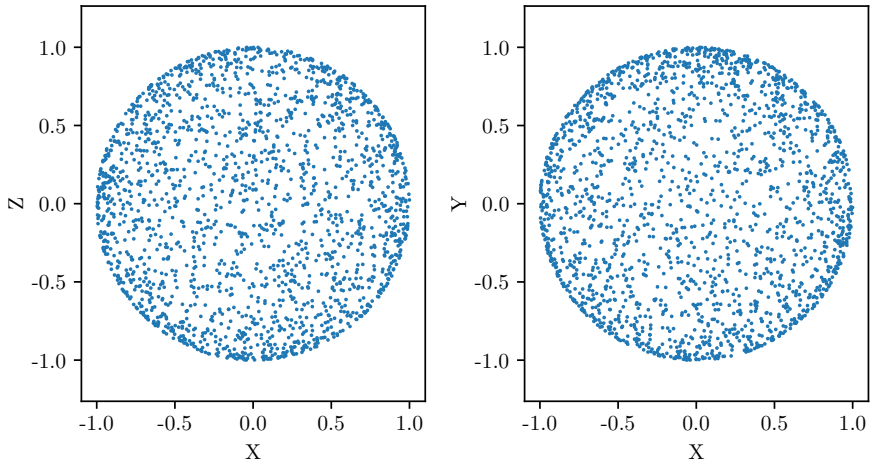

FIGURE 3.3: a) Front view of unit sphere in x-z plane.(left) b) Top view of unit sphere in x-y plane. (right)

Once the randomised unit vector is obtained, the post-collision velocity vector of incident electron $\mathbf{v}'_{\text{inc.}}$ is then

$$\mathbf{v}'_{\text{inc.}} = v'_{\text{inc.}} \cdot \hat{\mathbf{v}}$$

where

$$v'_{\text{inc.}} = \sqrt{v^2_{\text{inc.}} - \frac{2\varepsilon_{\text{redux}}}{m_e}}, \tag{3.17}$$

with $v_{\text{inc.}}$ denoting the velocity magnitude of incident electron before collision. m_e refers to the electron mass and $\varepsilon_{\text{redux}}$ the energy lost during the collision events, which depends on the type of collision outcome. As an example, $\varepsilon_{\text{redux}} = 0$ during an elastic scattering event and $\varepsilon_{\text{redux}} = 0.0441\,\text{eV}$ for rotational level transition of $J = 0 \rightarrow 2$.

The treatment of incident electron's velocity in the second group (which involves splitting of neutrals) is markedly different. In the case of electron hydrogen molecule collision, hydrogen molecule is about 3674 times heavier than electron. The resulting energy transferred from electron to hydrogen molecule is expressed by

$$E_{\text{kin,H}_2} = \frac{4m_{\text{e}}m_{\text{H}_2}}{(m_{\text{e}} + m_{\text{H}_2})^2} E_{\text{kin,e}}.$$

It is assumed that the positive ion (or H atom) after splitting does not gain any of the incident electron's energy. Thus, the remaining energy after ionisation is split between

the original electron and the newly freed electron by satisfying conservation of momentum and energy. In the event of successful ionisation, the required energy for ionisation is deducted from incident energy via Eq. 3.17 as well.

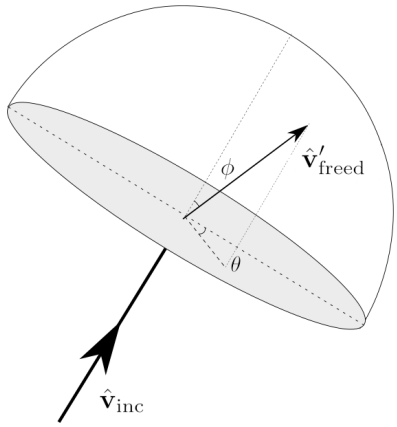

FIGURE 3.4: Allowed scattering angle for freed electron.

The freed electron's scatter direction is then determined randomly, but with the restriction that the angle of scattering is restricted to a hemisphere perpendicular to the incident electron vector shown in Fig. 3.4 ($\phi = [0, \pi/2]$). $\hat{\mathbf{v}}_{\text{inc.}}$ refers to the initial unit vector of the incident electron, while $\hat{\mathbf{v}}_{\text{freed}}$ denotes the unit vector of the freed electron after ionisation. The incident electron's vector direction after the impact is calculated in order to fulfil the conservation conditions. Since it is assumed that ion doesn't inherit any energy after ionisation ($\|\mathbf{v}_{\text{ion}}\| = 0$), the set of problems to be solved in order to obtain the incident electron's post-collision velocity reduces to a two-body elastic collision problem.

Assuming the freed electron's unit vector is predetermined as $\hat{\mathbf{v}}'_{\text{freed}}$, along with the knowledge of incident electron's velocity vector $\mathbf{v}_{\text{inc.}}$, the resulting post collision velocity vector of freed electron $\mathbf{v}'_{\text{freed}}$ and incident electron $\mathbf{v}'_{\text{inc.}}$ is fully described as

$$\begin{aligned} \mathbf{v}'_{\text{inc.}} &= ||\mathbf{v}'_{\text{inc.}}||\hat{\mathbf{v}}'_{\text{inc.}} \\ \mathbf{v}'_{\text{freed}} &= ||\mathbf{v}'_{\text{freed}}||\hat{\mathbf{v}}'_{\text{freed}}, \end{aligned}$$

where

$$\begin{aligned} \cos\theta' &= \frac{\mathbf{v}'_{\text{freed}} \cdot \mathbf{v}_{\text{inc.}}}{||\mathbf{v}'_{\text{freed}}||\ ||\mathbf{v}_{\text{inc.}}||} \\ ||\mathbf{v}'_{\text{freed}}|| &= \frac{2m_{\text{inc.}}}{m_{\text{freed}} + m_{\text{inc.}}}||\mathbf{v}_{\text{inc.}}||\cos\theta' \\ \mathbf{v}'_{\text{inc.}} &= \mathbf{v}_{\text{inc.}} - (m_{\text{freed}}/m_{\text{inc.}})\mathbf{v}'_{\text{freed}} \end{aligned} \tag{3.18}$$

Eq. 3.18 is solved for every instance where ionisation occurs. In the case of neutral dissociations where no additional electron is freed, the treatment of $\mathbf{v}'_{\text{inc.}}$ is simple. Eq. 3.15 and Eq. 3.17 is used instead, but with ϕ restricted to $[0, \pi/2]$.

Special consideration now applies to H atoms arising from either dissociative ionisation or neutral dissociation. Since the cross section of neutral dissociation and dissociative ionisation is comparable, the growth of H atom counts will follow the trend seen in H^+ ions. This means that up to the time scale of milliseconds in the plasma initiation process, the population of H atoms will still be more than 10 orders of magnitude smaller than the background H_2. For this reason, H atoms are not explicitly simulated. This extends to not including the electron - H ionisation channel as well. However, the number of H atoms as the simulation progresses is recorded, so that it can be used to inform the time when the population is sufficiently large to include electron - H scattering cross sections.

3.4.2.2 Vahedi & Surendra model

In this case, the calculation of the electron energy loss is still done using Eq. 3.17. However, the scatter angle is now a function of incident electron's energy [2]. In the case of ionisation, the scatter angle has a range of $\phi = [0, \pi]$ rather than being restricted to the forward half hemisphere $[0, \pi/2]$. The scatter angle is now computed by

$$\cos\phi = \frac{2 + \varepsilon - 2(1+\varepsilon)^R}{\varepsilon} \tag{3.19}$$

where R denotes random number of the range $[0, 1]$ and ε refers to incident electron's energy. The azimuthal angle is then determined randomly with $\theta = 2\pi R$.

An additional angle χ is also computed with $\cos\chi = \mathbf{v}_{\text{inc}} \cdot \hat{\mathbf{i}}$. The resulting scattered unit vector is then determined by

$$\begin{aligned}\hat{\mathbf{v}}'_{\text{inc.}} =& \hat{\mathbf{v}}_{\text{inc.}}\cos\phi + \hat{\mathbf{v}}_{\text{inc.}} \times \mathbf{i}\frac{\sin\phi\sin\theta}{\sin\chi} \\ &+ \hat{\mathbf{v}}_{\text{inc.}} \times (\mathbf{i} \times \hat{\mathbf{v}}_{\text{inc.}})\frac{\sin\phi\cos\theta}{\sin\chi}.\end{aligned}$$

The post-collision vector $\hat{\mathbf{v}}'_{\text{inc.}}$ calculation applies to both ionising and non-ionising events, with the energy respective to the collision type subtracted from the incident electron. In ionising events, Eq. 3.18 is used to properly partition the resulting electrons' energies.

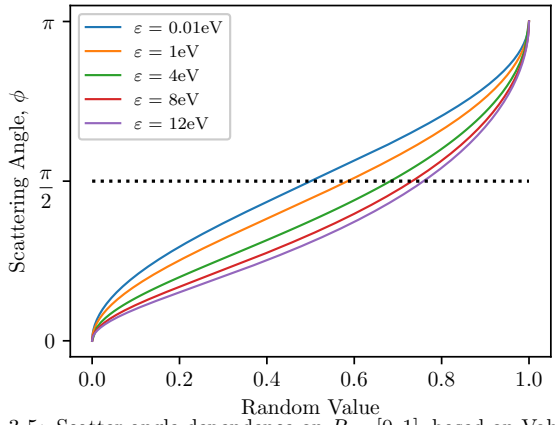

FIGURE 3.5: Scatter angle dependence on $R = [0, 1]$, based on Vahedi et al. [2].

Resolving Eq. 3.19 over a range of electron energy will affect the distribution of scattered angle and this is shown in Fig. 3.5. It is clear that the electrons are more likely to have scatter angles that are less than $\pi/2$ (forward scatter) as ε increases. At an energy of 0.01 eV, that shows an almost equal chance of forward or backward scatter.

3.4.2.3 Ohkrimovvsky model

In this section, the method proposed by Ohkrimovskyy et al. [3] is described. Normalised differential cross section for screened-Coulomb scattering of electron obtained from first Born approximation of quantum mechanical theory of scattering gives

$$I(\varepsilon, \phi) = \frac{1}{4\pi} \frac{1 + 8\varepsilon}{(1 + 4\varepsilon - 4\varepsilon \cos\phi)^2}$$

which can be rewritten as

$$I(\xi, \phi) = \frac{1}{4\pi} \frac{1 + \xi^2(\varepsilon)}{(1 - \xi(\varepsilon) \cos\phi)^2}. \tag{3.20}$$

Thus, by solving

$$R = P(\xi, \chi) = \frac{2\pi \int_0^{\chi} I(\xi, \chi) \sin\chi \mathrm{d}\chi}{2\pi \int_0^{\pi} I(\xi, \chi) \sin\chi \mathrm{d}\chi}$$

followed by some simple algebraic manipulations, scatter angle is given by

$$\cos\phi = 1 - \frac{2R(1 - \xi)}{1 + \xi(1 - 2R)}, \qquad R = [0, 1]. \tag{3.21}$$

Different interaction potentials will yield different $\xi(\epsilon)$ functions, but it can be deduced from

$$\frac{\sigma_m}{\sigma} = \frac{1-\xi}{2\xi^2}\Big((1+\xi)\ln\frac{1+\xi}{1-\xi} - 2\xi\Big), \tag{3.22}$$

where σ_m and σ denotes momentum transfer cross section and integral cross section of electron neutral collision.

Both σ_m and σ in Fig. 3.6 are plotted using the cross section data of Yoon *et al* [4], supplemented by van Wingerden's work [72] up to 2000 eV for the integral cross section and MAGBOLTZ code [73] for momentum transfer cross section up to 10 keV. Solving Eq. 3.22 with the obtained ratio gives ξ. Once ξ is obtained, it is used in Eq. 3.21 to compute the scatter angle ϕ (shown in Fig. 3.7).

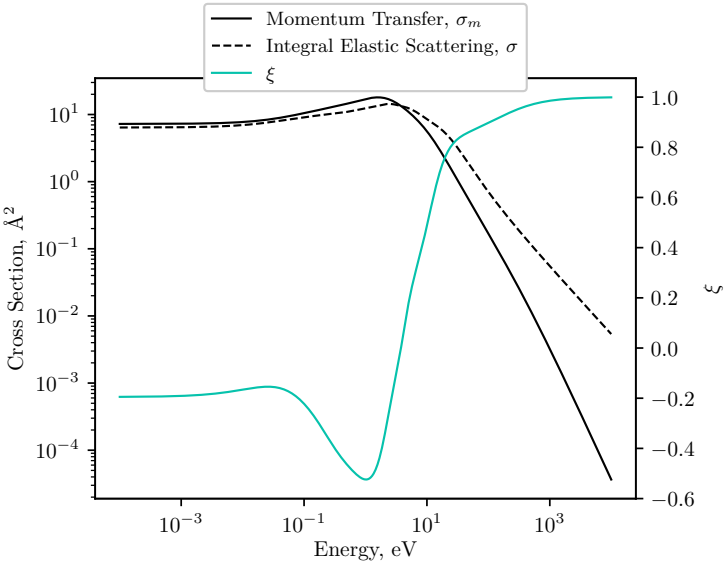

FIGURE 3.6: Cross section values of electron-H_2 molecule collision and the resulting $\xi(\epsilon)$ plotted over electron energy of 0.0001 - 10 000 eV.

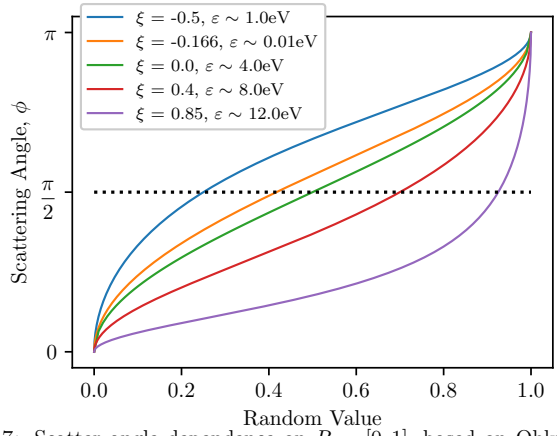

FIGURE 3.7: Scatter angle dependence on $R = [0, 1]$, based on Ohkrimovskyy et al. [3].

The resulting scatter angle distribution is markedly different from Fig. 3.5. This method produces extremes in both forward and backward scattering tendencies depending on incident electron's energy. It is shown in Fig. 3.7 that electron energy of approximately less than 3.8 eV, there is a higher likelihood that backward scatter would occur. The backward scatter tendency peaks at an energy of approximately 1 eV. Once the electron energy is above the threshold of 4 eV, it quickly becomes highly likely to scatter forward instead as seen in the case of 8 eV and 12 eV respectively.

A detailed study of the described scattering angle model will be presented in Ch. 5. The model that approximates experimentally obtained measures of α and V_e that is used in Eq. 2.19 will be chosen for the large scale tokamak plasma initiation simulation.

3.5 Tokamak field calculations

This section describes the implemented calculation of the external electromagnetic fields in toroidal geometry. As mentioned previously, the simulation is conducted in a 3D domain. Each simulated particle will then calculate the field vectors as a function of the particle's coordinates. This section is divided into 5 subsections, with the first 4 describing the numerical description of the electric and magnetic fields. The last subsection covers the numerical implementations that reduce the computational cost of resolving particles' experienced field values.

3.5.1 Vector potential of current density in circular loop

Maxwell's equations (Eq. 3.2) require that all magnetic fields $\mathbf{B}$ must be divergence free. A mathematical property involving the curl operator and divergence operator is exploited to ensure the divergence free condition is always satisfied. Assuming that there is vector $\mathbf{A}$, then the following condition holds

$$\nabla \cdot (\nabla \times \mathbf{A}) = 0. \tag{3.23}$$

$\mathbf{A}$ is then called the vector potential and its curl is magnetic field $\mathbf{B}$. Assuming that a magnetic field $\mathbf{B}$ is resulting from current density $\mathbf{J}$ flowing through a conductor, $\mathbf{A}$ can be deduced directly from the Biot-Savart law

$$\mathbf{B}(\mathbf{x}) = \frac{\mu_0}{4\pi} \int_{V'} \frac{\mathbf{J}(\mathbf{x}')\mathrm{d}V' \times (\mathbf{x} - \mathbf{x}')}{|\mathbf{x} - \mathbf{x}'|^3}. \tag{3.24}$$

By substituting

$$\frac{\mathbf{x} - \mathbf{x}'}{|\mathbf{x} - \mathbf{x}'|^3} = -\nabla \left(\frac{1}{|\mathbf{x} - \mathbf{x}'|} \right)$$

into Eq. 3.24, the equation becomes

$$\mathbf{B}(\mathbf{x}) = \frac{\mu_0}{4\pi} \int_{V'} \mathbf{J}(\mathbf{x}') \times -\nabla \left(\frac{1}{|\mathbf{x} - \mathbf{x}'|} \right) \mathrm{d}V'. \tag{3.25}$$

Since

$$\nabla \times \left(\frac{\mathbf{J}(\mathbf{x}')}{|\mathbf{x} - \mathbf{x}'|} \right) = \nabla \left(\frac{1}{|\mathbf{x} - \mathbf{x}'|} \right) \times \mathbf{J}(\mathbf{x}') + \frac{1}{|\mathbf{x} - \mathbf{x}'|} (\nabla \times \mathbf{J}(\mathbf{x}'))$$

and current density is flowing in a parallel manner through the conductor (no rotation within an infinitesimal volume at point $\mathbf{x}'$), naturally this means

$$\nabla \times \mathbf{J}(\mathbf{x}') = \mathbf{0},$$

Eq. 3.25 can be rewritten as

$$\mathbf{B}(\mathbf{x}) = \nabla \times \frac{\mu_0}{4\pi} \int_{V'} \frac{\mathbf{J}(\mathbf{x}')}{|\mathbf{x} - \mathbf{x}'|} \mathrm{d}V'. \tag{3.26}$$

Expression for the vector potential $\mathbf{A}(\mathbf{x})$ is then

$$\mathbf{A}(\mathbf{x}) = \frac{\mu_0}{4\pi} \int_{V'} \frac{\mathbf{J}(\mathbf{x}')}{|\mathbf{x} - \mathbf{x}'|} \mathrm{d}V'. \tag{3.27}$$

Fig. 3.8 shows the proposed simulation set-up, the poloidal magnetic field is established by current in a circular loop which lies in the x-y plane. The circular loop has a radius of R and the current density $\mathbf{J}$ is restricted to only present within the said loop. The

circular loop will later represent the poloidal field coils in a tokamak scenario. O denotes the object (charged particle) which is located at r distance from the circular loop's origin. The aim is to compute the $\mathbf{B}$ experienced by object O.

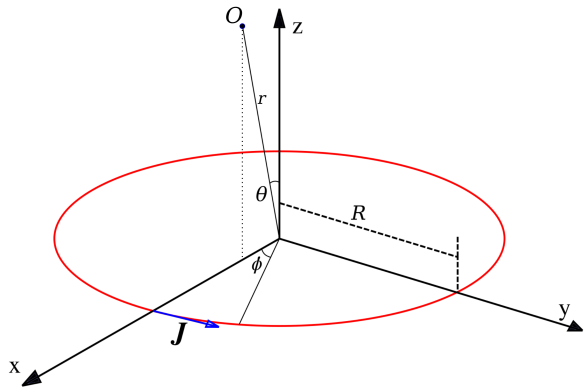

FIGURE 3.8: Current loop setting in spherical coordinate system.

Since $\mathbf{J}$ only travels along the circular loop, its magnitude is wholly its toroidal component, J_ϕ[1] which is

$$J_\phi = \frac{I}{R} \sin\theta' \ \delta(\cos\theta') \ \delta(r' - R) \tag{3.28}$$

Performing transformation from Cartesian to spherical coordinate system by substituting

$$\mathrm{d}V' = r'^2 \sin\theta' \ \mathrm{d}r' \ \mathrm{d}\phi' \ \mathrm{d}\theta'$$

Eq. 3.27 is now

$$A_\phi = \frac{\mu_0}{4\pi} \int \frac{I \cos\phi'}{R} \frac{\sin^2\theta' \ \delta(\cos\theta') \ \delta(r' - R) r'^2}{|\mathbf{x} - \mathbf{x}'|} \ \mathrm{d}r' \ \mathrm{d}\phi' \ \mathrm{d}\theta'. \tag{3.29}$$

Representing $\mathbf{x}$ and $\mathbf{x}'$ in spherical coordinate as

$$\mathbf{x} = r \ [\sin\theta\cos\phi, \ \ \sin\theta\sin\phi, \ \ \cos\theta]^T,$$

and proceed to evaluate $|\mathbf{x} - \mathbf{x}'|$ directly while keeping in mind that $\phi = 0$ yields

$$|\mathbf{x} - \mathbf{x}'| = \sqrt{r^2 + r'^2 - 2rr'(\sin\theta\sin\theta'\cos\phi' + \cos\theta\cos\theta')}.$$

[1]Derivation of J_ϕ is in App. B.

Using this identity, Eq. 3.29 is now

$$A_\phi(r,\theta) = \frac{\mu_0}{4\pi}\int \frac{I\cos\phi'}{R}\frac{\sin^2\theta'\ \delta(\cos\theta')\ \delta(r'-R)r'^2}{\sqrt{r^2+r'^2-2rr'(\sin\theta\sin\theta'\cos\phi'+\cos\theta\cos\theta')}}\ \mathrm{d}r'\ \mathrm{d}\phi'\ \mathrm{d}\theta'. \tag{3.30}$$

Evaluating the Dirac delta functions then yields

$$A_\phi(r,\theta) = \frac{\mu_0 IR}{4\pi}\int_0^{2\pi}\frac{\cos\phi'}{\sqrt{r^2+R^2-2rR\sin\theta\cos\phi'}}\ \mathrm{d}\phi'. \tag{3.31}$$

The expression for vector potential can also be expressed in complete elliptic integral of the first kind (K) and second kind (E)[2], which allows for efficient numerical implementation. The vector potential can now be written

$$\begin{aligned} A_\phi(r,\theta) &= \frac{\mu_0 IR}{\pi}\frac{1}{\sqrt{R^2+r^2+2rR\sin\theta}}\left(\left(\frac{2}{k^2}-1\right)K(k)-\frac{2}{k^2}E(k)\right) \\ \text{with } k^2 &= \frac{4rR\sin\theta}{R^2+r^2+2rR\sin\theta} \end{aligned} \tag{3.32}$$

For ease of numerical computation of the eventual magnetic field experienced by charged particles due to the current loop, transforming Eq. 3.31 into cylindrical coordinate system yields

$$\begin{aligned} A_\phi(\rho,z) &= \frac{\mu_0 I\sqrt{R}}{2\pi}\left(\left(\frac{2}{k\sqrt{\rho}}-\frac{k}{\sqrt{\rho}}\right)K(k)-\frac{2}{k\sqrt{\rho}}E(k)\right) \\ \text{with } k^2 &= \frac{4\rho R}{z^2+(\rho+R)^2} \end{aligned} \tag{3.33}$$

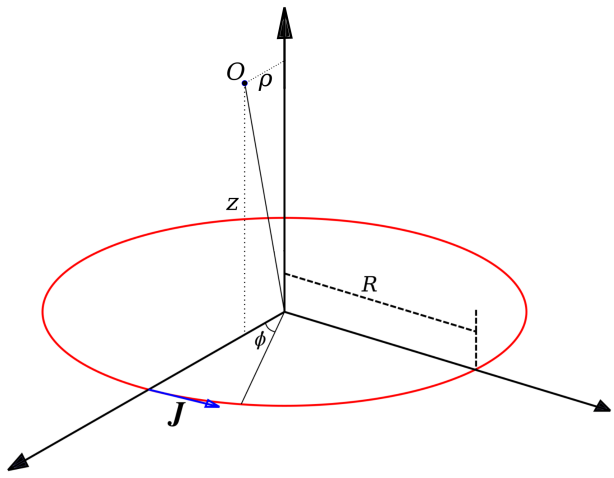

FIGURE 3.9: Current loop setting in cylindrical coordinate system.

[2]Steps to express Eq. 3.31 in $K(k)$ and $E(k)$ is in App. B

3.5.2 Poloidal B field

In a tokamak, it is convenient to describe the overall background magnetic field by the sum of toroidal and poloidal components. The overall magnetic field will satisfy the divergence free condition if the prescribed poloidal and toroidal fields are individually divergence free. This is evident from the distributive property of the divergence operator

$$\nabla \cdot (\mathbf{X} + \mathbf{Y}) = \nabla \cdot \mathbf{X} + \nabla \cdot \mathbf{Y}.$$

When both $\nabla \cdot \mathbf{X} = 0$ and $\nabla \cdot \mathbf{Y} = 0$, the divergence free condition of the overall field is naturally satisfied.

The poloidal magnetic field at point $\mathbf{x}$ (in terms of ρ and z only, ϕ is ignored due to toroidal symmetry of the current loop.) can be obtained by evaluating the curl of Eq. 3.33 which gives the following relations

$$\begin{aligned} B_\rho &= \frac{1}{\rho}\frac{\partial A_z}{\partial \phi} - \frac{\partial A_\phi}{\partial z} \\ B_\phi &= \frac{\partial A_\rho}{\partial z} - \frac{\partial A_z}{\partial \rho} \\ B_z &= \frac{1}{\rho}\left(\frac{\partial (\rho A_\phi)}{\partial \rho} - \frac{\partial A_\rho}{\partial \phi}\right) \end{aligned}$$

Since A_ρ and A_z are both zero, B_ϕ will be zero. Directly performing the differentiation and some rigorous algebraic manipulations gives

$$\begin{aligned} B_\rho &= \frac{\mu_0 I z}{2\pi\rho\sqrt{z^2 + (\rho + R)^2}}\left(\frac{z^2 + \rho^2 + R^2}{z^2 + (\rho - R)^2}E(k) - K(k)\right) \\ B_z &= \frac{\mu_0 I}{2\pi\sqrt{z^2 + (\rho + R)^2}}\left(\frac{R^2 - z^2 - \rho^2}{z^2 + (\rho - R)^2}E(k) + K(k)\right) \end{aligned} \tag{3.34}$$

The poloidal magnetic field is of course divergence free as a direct result of Eq. 3.23. The example poloidal field shown here assumes that the current loop is at $z = 0.0$. In the actual implementation, multiple loops with various R and vertical placements are defined such that the combination creates the intended poloidal field geometry.

3.5.3 Toroidal B field

The toroidal magnetic field is implemented as a current running along an infinite length wire in the $\hat{\mathbf{z}}$ direction, coinciding with the tokamak's major axis. As such, the analytical

expression for the toroidal magnetic field in cylindrical coordinates is

$$\mathbf{B}(\rho) = \frac{\mu_0}{2\pi}\frac{I}{\rho}\hat{\boldsymbol{\phi}} \tag{3.35}$$

with B_ρ and B_z component being zero. The question is whether such description satisfies $\nabla \cdot \mathbf{B}(\rho) = 0$.

Divergence of a vector field in cylindrical coordinate is given as

$$\nabla \cdot \mathbf{B} = \frac{1}{\rho}\frac{\partial(\rho B_\rho)}{\partial \rho} + \frac{1}{\rho}\frac{\partial B_\phi}{\partial \phi} + \frac{\partial B_z}{\partial z}.$$

Note that B_ρ and B_z are zero, thus the expression reduces to

$$\nabla \cdot \mathbf{B} = \frac{1}{\rho}\frac{\partial B_\phi}{\partial \phi} = \frac{1}{\rho}\frac{\partial}{\partial \phi}\left(\frac{\mu_0}{2\pi}\frac{I}{\rho}\right) = 0.$$

Therefore, the overall magnetic field experienced by charged particles is completely specified by Eq. 3.34 and 3.35.

3.5.4 Toroidal E field

In general, the electric field need not be divergence free. However, the toroidal electric field in a tokamak during the plasma initiation phase is a result of the current ramp-up of the central solenoid. As a result, the prescribed background toroidal electric field should also be divergence free. The implemented expression of the toroidal electric field is similar to Eq. 3.35, taking the form of

$$\mathbf{E}(\rho) = \frac{V_{\text{loop}}}{2\pi\rho}\hat{\boldsymbol{\phi}} \tag{3.36}$$

Here, one can define a value of V_{loop} such that the electric field strength at the minor axis of the torus corresponds to the expected tokamak operating parameter. The proof that this field definition satisfies the divergence free condition follows from Sec. 3.5.3.

3.5.5 Grid interpolation of poloidal B field

The numerical studies in Ch. 6 and 7 will eventually simulate up to 10^8 charged particles. Numerical evaluation of Eq. 3.34 for each particle is therefore unfeasible via direct evaluation of the integrals of $E(k)$ and $K(k)$, which are computationally expensive. Therefore the set of equations is evaluated once at the start of the simulation and then tabulated, exploiting the fact that the background magnetic fields are static in time.

This is done by specifying a 2D grid in the poloidal plane, and computing the poloidal magnetic field values at each of the grid points. A 2D poloidal plane grid is sufficient since the poloidal magnetic field is toroidally symmetric. Once the computed values are saved in the grid points, a linear interpolation of the grid field values can be made to the particles' positions. This avoids repeated numerical evaluation of Eq. 3.34 for every particle at every time step.

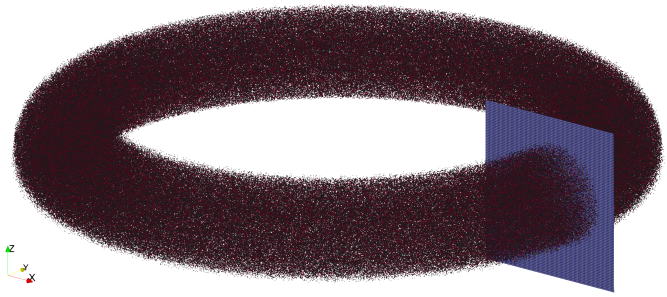

FIGURE 3.10: Extent of the 2D poloidal plane grid.

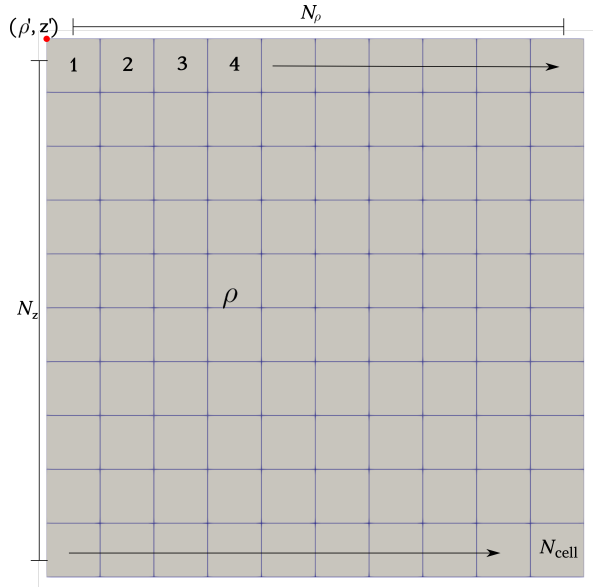

FIGURE 3.11: Grid number ordering.

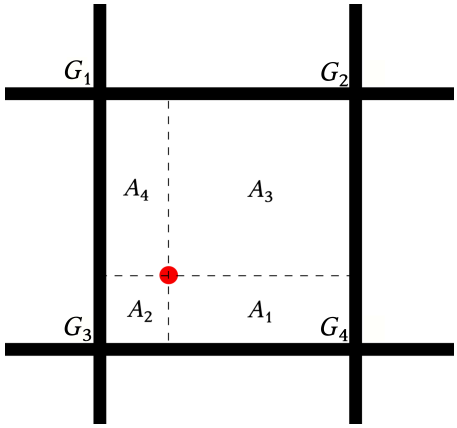

FIGURE 3.12: Weights (corresponding labeled rectangular area, A_i) of each corner's contribution of $\mathbf{B}_\mathrm{pol}$ on the red particle.

The linear interpolation of $\mathbf{B}_\mathrm{pol}$ onto a particle is briefly explained here. Beginning from the definition of the 2D grid, the extent of the grid covers only the minor radius of the simulated torus geometry as shown in Fig. 3.10. Conscious ordering of cell number is made so that each particle's (ρ, z) coordinate can be used to compute the cell number directly, using the knowledge of the regular cell size ($\Delta\rho$ and Δz) and the number of cells in both ρ and z direction (N_ρ and N_z). Referring to Fig. 3.11, the 2D plane is split into a total of N_cell cells with the top left grid has the coordinate of (ρ', z'). The starting index for both the cell and grid points numbering is 1. The exact cell number N_i that a particle 'i' belongs to is computed as

$$\begin{aligned} \eta_\mathrm{i} &= \lfloor |\rho_\mathrm{i} - \rho'| / \Delta\rho \rfloor + 1 \\ \zeta_\mathrm{i} &= \lfloor |z_\mathrm{i} - z'| / \Delta z \rfloor + 1 \\ N_\mathrm{i} &= (\zeta_\mathrm{i} - 1) N_\rho + \eta_\mathrm{i}. \end{aligned} \tag{3.37}$$

Once the cell number is known, the corresponding vertices in Fig. 3.12 are then calculated with

$$\begin{aligned} G_1 &= N_\mathrm{i} + \zeta_i - 1 \\ G_2 &= G_1 + 1 \\ G_3 &= G_2 + N_\rho \\ G_4 &= G_3 + 1. \end{aligned} \tag{3.38}$$

The labelled areas A_j will have to be normalised with the area of the cell in order to make sure that the computed weights satisfy partition of unity, thus giving

$$\begin{aligned} A'_j &= \frac{A_j}{\Delta\rho\Delta z} \\ \sum_{j=1}^{4} A'_j &= 1 \end{aligned} \tag{3.39}$$

The interpolation step of $\mathbf{B_{pol,i}}$ is then

$$\mathbf{B}_{\mathrm{pol,i}} = \sum_{j=1}^{4} A'_j \mathbf{B}_{\mathrm{pol}}(G_j). \tag{3.40}$$

In principle, a higher-order interpolation is possible here, but this was ruled out due to two factors. Firstly, the increased computational cost for second order interpolation undermines the initiative of this grid interpolation method in the first place. Secondly, grid resolution can be increased arbitrarily without increasing the computation cost of the implemented interpolation routine. Thus, N_ρ and N_z are chosen for specific simulation cases after convergence tests.

Discussions regarding the numerical components of particle-based Townsend avalanche breakdown code are concluded with this topic. There are quite a few more implementations that provide supporting framework which enables the physics based computations discussed so far. These implementations were omitted from writing in order to limit the scope of discussions to physical considerations related to Townsend avalanche breakdown and tokamak field geometry. Some examples of the supporting subroutines are the curation of the list of particles before each time step's self-consistent $\mathbf{E}$ field calculations, charged particles diagnostic tools and the prescription of the simulation domain boundary. A simplified overview of the program flow is shown in Fig. 3.13 for reference.

At the start of the program, the 2D grid of resolved $\mathbf{B_{pol,i}}$ is first computed and stored. Charged particles are then initiated and the respective self-consistent electric field computed. The time stepping loop then begins, with each particle calculating its experienced background electric and magnetic fields, adding to the computed self-consistent electric field. Update of the particle's velocity and position is done via the gyrophase corrected Boris algorithm. This is then followed by the collision probability and the respective outcomes. Once all the particles go through the three steps, any newly created electron-ion pairs are collected and prepared for the next round of self-consistent electric field computation (via PEPC). Results will then be saved for diagnostics and the whole process repeats.

```
Program start
compute and store B_pol
initiate charged particles
compute self-consistent E field (PEPC)

while steps remaining do
  while particles remaining do
    compute experienced total E and B field
    update velocity and position
    calculate scattering or ionisation
  end while
  gather new ion-electron pairs
  compute self-consistent E field (PEPC)
  save simulation results
end while
end program
```

FIGURE 3.13: Simplified overview of Townsend avalanche breakdown code.

Most of the technical aspects of the developed simulation code are covered up to this point. Some of the technical details are not discussed here, as those require additional physical considerations related to the simulation study itself. In particular, the collision cross sections are covered in Ch. 5 and 6 respectively.

Chapter 4

Merging algorithm

4.1 Introduction

The expected growth of the ion/electron population is exponential as seen in Townsend's Eq. 2.11, which is also consistent with the analytical solution of Eq. 2.19. Achieving a numerically manageable problem size during the simulation while maintaining an accurate physical representation of the system is crucial to simulating a near fusion-ready plasma in tokamak. The background electron number density for such plasma is approximately $10^{16}\,\mathrm{m}^{-3}$, a number that is unfeasible to handle numerically for a first principles particle-based solver. One method to resolve the issue is to merge large number of simulated charged particles into fewer super-particles, which then reduces the overall computational cost of the simulation. The process of merging must be handled with care in order to preserve the physical state of the charged particles system (energy, momentum distribution etc.). This chapter focuses on the merging algorithm of simulated charged particles in the application of Townsend avalanche simulation in tokamak. While the present studies will not quite reach density of $\sim 10^{16}\,\mathrm{m}^{-3}$, implementation of merging algorithm is still important to pave the way for future work approaching the full breakdown regime.

Since the focus of this study is the time evolution of charged particle population in ITER-like first plasma scenario, a merging algorithm that can preserve the energy distribution of charged particles in the proximity of the ionisation energy range is of utmost importance. The main reason is that the likelihood of impact ionisation depends on the energy carried by electrons. Should the energy distribution of electrons be altered in the process of merging, the growth rate of the charged particle population may change as a consequence. There are multiple ways to introduce this unintentional change: one

example is the improper choice of particle sampling (such as disregarding the proximity of the sampled particles in momentum phase space), which will produce a super-particle which can have a vastly different energy and momentum than its predecessors. Another contributing factor would be the improper treatment of energy, momentum and weight partition of the merged super-particle. This is further complicated by the fact that the super-particles will then be involved in impact ionisation events, affecting the energy-momentum distribution in future timesteps. Since merging essentially attempts to represent a highly detailed system with a coarser approximation, discrepancies in the resulting time evolution of energy-momentum distribution and growth rate cannot be fully avoided (especially for a scenario where the system is exponentially growing in time). A discussion on the choices and compromises made during the design of the merging algorithm will follow in Sec. 4.2.

Another consideration to make is the preservation of the original particles' spatial distribution after merging. This condition is easily met in the case of grid-based numerical methods such as the Particle-in-Cell method, where the merging algorithm can be restricted to sample original particles locally based on the existing grid structure [74, 75]. For mesh-free methods, an alternative methodology is needed to ensure the sampled particles respect the spatial proximity criteria. One such method is to assign parent-child relations of the particles via a k-d tree [76], through which one can traverse through the tree for nearest-neighbour search, only merging particles that share the same parent. The implemented spatial proximity search here operates in a similar vein, taking advantage of the tree structure created via the Barnes-Hut algorithm instead.

Teunissen *et al.* [76] proposed a methodology that merges two particles into one at every merging instance. It can be shown that such merging cannot conserve both energy and momentum. Beginning with two particles with masses m_1 and m_2, as well as velocities $\mathbf{v}_1$ and $\mathbf{v}_2$, the conservation of mass, momentum and energy is expressed as

$$\begin{aligned} m_1 + m_2 &= M \\ m_1\mathbf{v}_1 + m_2\mathbf{v}_2 &= M\mathbf{U} \\ m_1 v_1^2 + m_2 v_2^2 &= MU^2. \end{aligned}$$

M and $\mathbf{U}$ denote the mass and the velocity vector of the resulting merged super-particle respectively. v_1 and v_2 are the respective velocity magnitudes, as in $v_1 = \|\mathbf{v}_1\|$. In the case where one attempts to respect the momentum conservation, the resulting $\mathbf{U}$ would then be

$$\mathbf{U} = \frac{m_1\mathbf{v}_1 + m_2\mathbf{v}_2}{M}.$$

It then violates the conservation of energy, as it results in

$$m_1 v_1^2 + m_2 v_2^2 \neq \frac{m_1^2 v_1^2 + m_2^2 v_2^2 + 2 m_1 m_2 \mathbf{v}_1 \cdot \mathbf{v}_2}{M}.$$

As such, Teunissen *et al.* proposed multiple schemes to resolve the energy and momentum assignment of the merged super-particles. The work showed promising results for the scheme in which one of the particle's velocities is chosen at random, while scaling the chosen velocity to fulfil the energy conservation criteria. However, direct alteration of the super-particles' velocity magnitude (by extension, its energy) alters the momentum phase space of the particle system and such impact on overall ionisation rate hasn't been tested. Work done by Vranic *et al.* allows for arbitrary $n > 2$ particles to be merged into two super-particles in Particle-in-Cell codes. The work also proposed a detailed methodology for particle selection for merging in spatial and momentum phase space, which is additionally constrained by the conservation laws of energy and momentum. In the shown example, however, an assumption is made such that the weight and momentum magnitude partition is equivalent between the two resulting super-particles. This, in turn, introduces fractional weights to super-particles should an odd number of merging candidates are involved during the merging process. While it is not inherently detrimental, careful consideration is required when simulating super-particle scattering events which yield ionisation outcomes.

The proposed algorithm in this work aims to combine the nearest-neighbour search via the tree structure from the Barnes-Hut algorithm in PEPC with a particle merging methodology that respects the particles' spatial, energy and momentum distribution which allows for variable weights in the resulting merged super-particles. Ideally, this scheme should also preserve the charged particle growth rate of the original simulation as well as minimising the changes introduced to the particles' momentum distribution.

4.2 Particle selection for merging

This section first covers the details related to the selection of merging candidates followed by the derivation of the weights and momentum distribution expressions between the resulting merged super-particles. Merging candidate selection aims to narrow the choice of particles for merging in order to preserve the original charged particle collective's spatial, energy and momentum distribution. Since the simulation also includes H^+ and H_2^+ ions as byproducts of e-H_2 impact ionisation, the selected candidates to be merged must also be of the same species to avoid unphysical recombination instances.

The methodology of imposing multiple selection criteria uses a filter for each criterion that is applied sequentially to the global collection of particles. The first selection criterion is the spatial proximity filter as this works well with the way particle data is sorted and stored during the simulation. This will be discussed in detail in the following Sec. 4.2.1. Once the particles are grouped based on their spatial proximity, each local process (MPI rank) can apply additional selection criteria to its assigned grouped particles within a parallelised compute region. This specific ordering of selection criteria ensures that the merging algorithm will have a good parallel scaling efficiency, which is crucial so that > 250 compute processes can be used concurrently.

4.2.1 Spatial proximity selection

Among the considered merging candidate selection criteria, the spatial proximity selection criterion is the most complex. At the same time, it provides a straightforward implementation of the other selection criteria if done well. The core idea of this selection criterion is to allow merging of particles that are in close proximity to each other.

A brief explanation of the spatial particle sorting is given here to illustrate how each particle's coordinate can be used to derive proximity information among neighbours. A detailed description of the mapping from 3D coordinates into 1D 64-bit integer binary keys for each particle can be found in the work by Warren *et al.* [65].

In this example, the particles are distributed on a 2D ($m = 2$) plane and mapping from mD to 1D is done via Morton space filling curve. Note that the actual implementation of the mapping function in PEPC is performed using the Hilbert space-filling curve, which is obtained by applying another layer of transformation onto the initial Morton order.

Fig. 4.1 shows a cell structure of an n-level subdivisions performed on a square domain. A quick clarification is made here, that the cells shown in this section are only for visualisation purposes and they are not stored variables during the simulation runs. Integer coordinates in both x and y are assigned for each of the cells at every level and further represented in binary notation. The number of subdivisions proceeds until all of the particles belong in their own cell. For this example, an assumption is made without loss of generality such that 3 levels of subdivision are sufficient. The particle's x and y coordinates are mapped to a 1D integer particle key and it is the chosen mapping function that determines the space-filling curve traversal pattern across all individual cells.

This is illustrated from the n_1 subdivided domain by first representing the four cells'

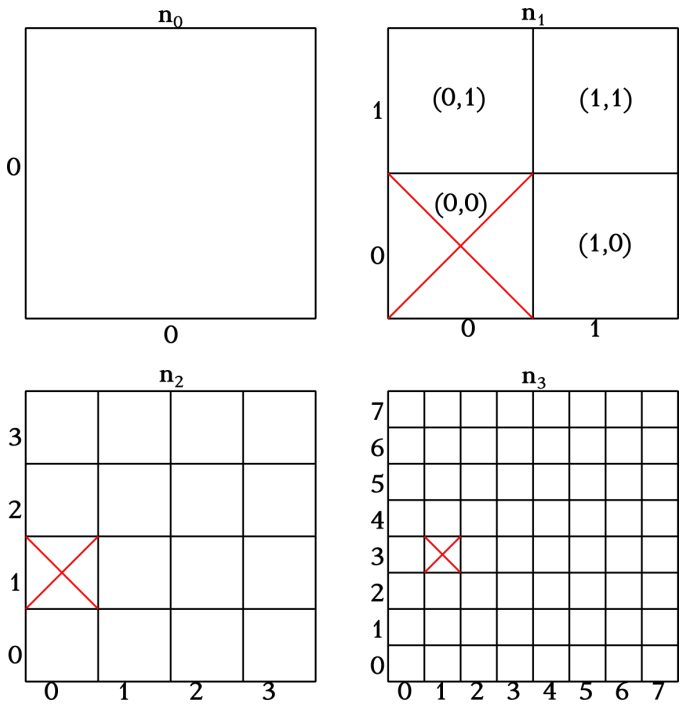

FIGURE 4.1: 2D cell structure of 3 levels of subdivisions. The red crosses corresponds to the domains that house the particle located in (1,3) at n_3 level.

integer coordinates with binary numbers, the binary number should have the number of bits that is equivalent to the maximum subdivision level (which is $n_{\text{lev}} = 3$ in this example). Taking the cell with coordinate of (1,0), the corresponding binary number for the x coordinate is then $b_{x,1} = x_3x_2x_1 = 001$ and the y coordinate is $b_{y,1} = y_3y_2y_1 = 000$. The next step is to map the binary coordinates into one binary number by interleaving the x and y bits with the following rule

$$\texttt{particle\_key} = (y_{n_{\text{lev}}}, x_{n_{\text{lev}}}, y_{n_{\text{lev}}-1}, x_{n_{\text{lev}}-1}, \ldots, y_1, x_1)_2. \tag{4.1}$$

Hence, the resulting key is 000001. If the operation is repeated for all the cells in n_1 subdivision and the keys are sorted in an ascending order, this corresponds to the flipped "Z" letter of Morton space-filling curve pattern. This shows that conversion from Morton to Hilbert space filling curve is possible with a different mapping function than the presented bit interleaving, provided that the transformation routine only allows pathways which follow the production rule of Hilbert space-filling curve [77]. While the Morton space-filling curve seems to provide a pathway for the nearest neighbour search, there are intermittent spatial "jumps" for high subdivision levels which don't necessarily respect spatial proximity. An example is the jump from (7,3) to (0,4) as one goes through

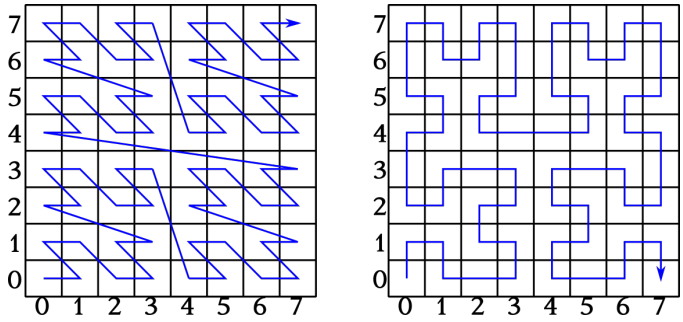

FIGURE 4.2: a) Morton space-filling curve traversal pattern at n_3 level. b) The corresponding Hilbert space-filling curve.

the sorted particle keys at n_3 subdivision (as seen in Fig. 4.2a).

This problem is largely prevented in a Hilbert space-filling curve traversal that provides a better locality property, which ensures particles that are close to each other in the sorted 1D key are also in similar proximity once reverse mapped to a higher dimension. At this point, one could possibly utilise the sorted 1D keys to select merging candidates by simply truncating the key traversal length to a user-defined particle count. However, the downside to this fixed-length candidate selection is the inability to correctly gauge the physical distance between particles, especially when the spatial distribution of particles is sparse. A clear statement has to be made here, that traversing the 1D sorted keys only provides a nearest neighbour search. An additional measure is required to actually determine the distance between particles. In order to avoid merging particles that are separated beyond a user-defined length scale, the merging candidate selection criterion must also include the parent-child relation between particles. Establishing such relation helps provide additional control over the size of the volume that particles share, thus selected as potential merging candidates.

The implementation follows the idea of using the cell size at the user-defined parent's level to limit the selection of merging candidates. In short, only particles that share the same parent will be considered for merging. Identification of the parent for each particle is an important but trivial step before such measure can be taken. Referring to Fig. 4.1, a particle in (1,3) at n_3 level is used as an example to demonstrate that the computed 1D particle key from bit interleaving can recover the parent node key through simple bit operation. The red crosses at n_1 and n_2 levels are the cells which encompass the considered particle at n_3. The particle keys resulting from Eq. 4.1 for the highlighted

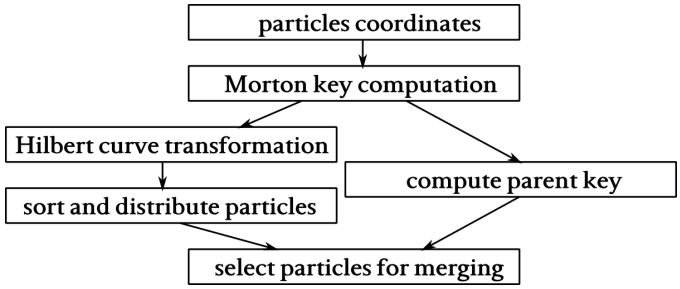

FIGURE 4.3: Flowchart for merging candidate selection by spatial proximity.

cells are

$$\begin{aligned}\text{key}_{n_1}(0,0) &= 000000\\ \text{key}_{n_2}(0,1) &= 000010\\ \text{key}_{n_3}(1,3) &= 001011.\end{aligned}$$

In order for a particle to compute its parent's key, a simple right shift bit operation is sufficient. Specifically,

$$\text{key}_{\text{parent},n_3\to n_2}(1,3) = \text{key}_{n_2}(0,1) = \texttt{RIGHTSHIFT}(\text{key}_{n_3}(1,3), m)$$

where m is the number of bits to right shift and it corresponds to the spatial dimensionality of the simulation. Similarly, given the 1D integer key, its parent key at the chosen number of subdivision level n can be computed via $n_{\text{diff}} = n_{\max} - n$ multiples of m bit shifts.

$$\text{key}_{\text{parent},n_3\to n}(1,3) = \texttt{RIGHTSHIFT}(\text{key}_{n_3}(1,3), n_{\text{diff}}\ m) \tag{4.2}$$

It is worth a reminder at this point that the examples shown have limited the key's number of bit representations corresponding to the maximum subdivision level of $n_{\max} = 3$. In the actual application, the maximum subdivision level is dependent on the bit-length of the variable that stores the particle key, which is set as a 64-bit integer variable in this case. For a simulation in a 3D domain, this works out to be a maximum of 20 subdivision levels (or 21-bits per coordinate, giving 63 bit integer keys with 1 placeholder bit). Another notable mention is that the subdivisions are applied to a parent domain which is a cuboid that encompasses all the simulated particles.

All the required components for merging candidate selection based on spatial proximity have been briefly explained so far. The simplified overview of the selection process is illustrated in Fig. 4.3. All the particles first undergo the 1D integer key computation (Morton space-filling curve step followed by Hilbert curve transformation). Now that

the particle keys are stored, the sorting process occurs before the particle collective is distributed across all participating compute units. The sorting process ensures that all the particles that are eventually handled by individual compute units are in the same spatial vicinity (locality property from Hilbert space-filling curve) as well as ensuring proper load balancing between all compute units. Once the particles are distributed, each unit loops over all its particles to compute the parent key at chosen n-level subdivision via Eq. 4.2, grouping of the particles is then done by the resulting parent keys.

There exists a minor drawback when the particles are distributed across all compute units (which will now be referred as processes). Specifically, there will be particles that are spatially close to each other but separated by artificial boundaries as a result of such distribution, since the processes only handle the set of particles given to them. In order to remove such artificial boundaries, additional communication between neighbouring processes is required such that particles that share a parent across the boundaries can be moved onto the same process. However, having additional communication between processes introduces further computation overhead. Thus, a decision was made to ignore such artificial process boundaries. This allows a better parallel efficiency of the merging algorithm, with the drawback of introducing additional groupings of merging candidates within the same parent (which spatially span more than one process).

Now that the particles are grouped into their local proximity, subsequent selection criteria can be applied within the same group by individual processes in a straightforward manner.

4.2.2 Species selection

As mentioned before, there will be multiple species of charged particles that are simulated throughout the Townsend avalanche breakdown scenario. The selection of the merging candidate by species is rather straightforward compared to the spatial selection methodology. The general idea is to restrict the merging of particles to those of the same species at all times.

Following from the spatially grouped particles in the previous subsection, the particles are sorted based on the nearest neighbour criteria (a direct result of 1D particle key sorting via Hilbert space-filling curve traversal pattern). However, the performed sort does not respect the species type of the particles. In order to separate the particles according to their species, an additional merge sort algorithm is applied to the grouped

particles. Merge sort has comparatively the least complexity among comparison sorting algorithms at $\mathcal{O}(n \log n)$ (n is the number of entries) in both best and worse case scenarios [78]. It also has the advantage of being highly parallelisable, bringing the complexity down to $\mathcal{O}(\log n)$ [79]. The fact that the sorting algorithm is not limited to sorting integer entries made it a compelling choice as the de facto sorting algorithm throughout this breakdown avalanche solver. Admittedly, Radix sort would be a better choice for species sorting as the particle species identifier is an integer based variable. The algorithm has the complexity of $\mathcal{O}(n)$ in this case since the number of species types is not more than 10 [80] (only 1 digit is required to identify all species). Both merge and Radix sort are stable sorting algorithm, meaning that the sequential order of repeated values is preserved. This ensures that the particles with the same type still preserve the nearest neighbour ordering from the spatial proximity criterion.

An example of the merging candidate selection by species is as follows. Each particle carries the information of its species type via an integer based variable. Electrons are labeled with species tag of 0, H^+ ions with 1 and H^{2+} is 2. If the simulation includes more particle types, the identifier can be extended to accommodate the need. Given an initial collection of local particles that a process handles, the sorting algorithm is applied to the particle array to either sort in ascending or descending order based on the species tag. Once it is done, further grouping of merging candidates based on other criteria is carried out within the sorted group.

4.2.3 Energy proximity selection

In general, selection of merging candidates based on their proximity in momentum phase space is sufficient to minimise the changes to the collective's momentum distribution [74]. The current strategy of achieving the same goal involves the combination of two selection criteria, namely the grouping of merging candidates based on energy proximity and the unit vector of the candidates' velocities. This is motivated by the need to preserve the energy distribution specifically as it dictates the charged particle population growth rate in time during avalanche breakdown. In order for the super-particle to better represent the energy distribution of its merging candidates, it is helpful that the energy range of the merging candidates themselves is narrow. This way, the merging candidates' average energy (which the super-particle inherits) can be a good representation for the eventual calculation of collision outcomes. Otherwise, the super-particles would have to store the information of the candidates' original energy distribution to provide a good approximation of electron-neutral collision outcomes (via convolution with the given cross sections). A super-particle may not be able to properly represent its merging

candidates' energy distribution as well when the super-particle represents a low number of merging candidates.

In the current implementation, the choice of the energy groupings is based on the energy resolution of all considered cross sections (refer to App. A). The rationale behind this definition is based on two points. First is the requirement that the merging process fulfils conservation of energy and momentum, therefore the energy of the super-particle per weight lies within the same energy group. Secondly, the knowledge that the changes in the cross section values are negligible (a maximum difference of approximately 4 % relative to each cross section's maximum value.) between two adjacent energy levels. Thus, while the difference of averaged energy between the merging candidates and the resulting super-particle falls within the width of the cross sections' energy resolutions, the changes to the resulting cross section are regarded as negligible.

As an example of the implementation, unique energy entries from all considered cross sections are combined into a single array in ascending order which is then the energy levels used to group merging candidates. In the combined energy level table, there is an energy group in the range of $[0.35\,\mathrm{eV}, 0.4\,\mathrm{eV}]$ which all particles whose energy fall within the range are collected into that group. The resulting super-particle's energy per weight would ideally also fall within that range, and such energy will be used to compute the collision outcomes. Particles whose energies are above the final entry in the energy grouping will not be merged.

In order to retain the focus of the discussion on the merging candidate selection criteria, the derivation of the momentum of the merged super-particles will be detailed later in Sec. 4.3, as well as considerations taken to fulfil the above assumptions.

4.2.4 Momentum unit vector selection

The simulation domain of the tokamak breakdown scenario is a simplified 3D torus in which the charged particles are confined. Since the torus is subjected to a toroidal background electric field $E_{\mathrm{tor.}}$, it is expected that the particles have preferred momentum directions which are dependent on their charge. Not to mention that each particle experiences scattering events with the background neutral molecules, further contributing to backscattering or generating momentum perpendicular to the toroidal direction. Selection of the merging candidates becomes important in order to avoid merging of particles

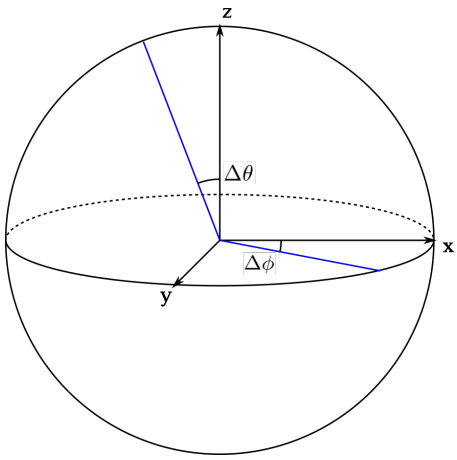

FIGURE 4.4: Schematics of the angle extents $(\Delta\theta, \Delta\phi)$ for unit vector merging candidate grouping.

with strongly diverging momentum unit vectors. The previous subsection already covered the merging candidate selection based on energy, the discussion here focuses on the implemented grouping of particles by their momentum vector.

Referring to Fig. 4.4, it is clear that $\theta = [0, \pi]$ and $\phi = [0, 2\pi]$. In the current implementation, the unit vector groupings are defined by equally spaced angle $\Delta\Omega = \Delta\theta = \Delta\phi$. The method of grouping merging candidates starts by calculating each particle's momentum orientation in θ and ϕ angle. It is then followed by assigning the particles to the appropriate discretised unit vector orientation groups.

There are a total of 4 selection criteria and the flow chart of how the selection criteria are applied to a given particle system is shown in Fig. 4.5. Starting from the given overall particle system, the spatial proximity selection filter is first applied. A localised group of particles are created for each 'parent'. From this local particle system, further 3 selection criteria are applied sequentially, each time selecting an ever shrinking number of particles that met each selection criterion. It should be mentioned again that the 3 selection criteria can be applied in any order. Once all the previously discussed merging candidate grouping is done, the merging algorithm detailed in Sec. 4.3 is applied.

4.3 Particle merging and momentum partitioning

This section details the derivation of the resulting merged particles' momentum vectors, assuming there are n merging candidates and results in 2 super-particles. The following variables are introduced for the derivation that follows:

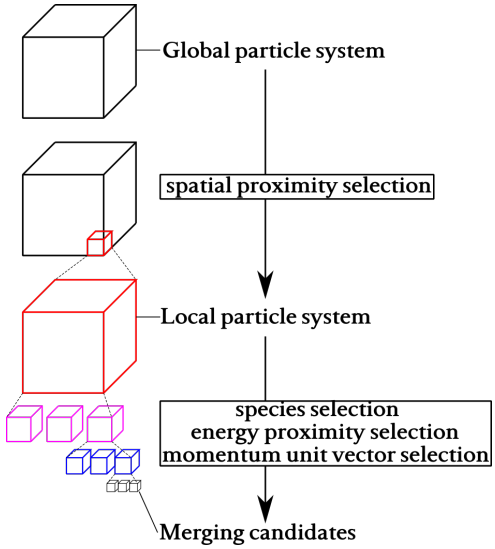

FIGURE 4.5: Sketch of the flow chart describing the order of applied selection filters to the initial charged particle system.

- w_i, weight of each merging candidate (particles to be merged).
- m_i, mass of each merging candidate.
- W_n, total weight of n particles
- $\mathbf{p}_\mathrm{t} = \sum_{i=1}^{n} w_i \mathbf{v}_i$
- $\epsilon_\mathrm{t} = \sum_{i=1}^{n} w_i \|\mathbf{v}_i\|^2$
- W_1, weight of the first merged super-particle
- W_2, weight of the second merged super-particle
- $\mathbf{V}_1$, velocity vector of the first merged super-particle
- $\mathbf{V}_2$, velocity vector of the second merged super-particle

Since the merging candidates are selected via the species selection (Sec. 4.2.2), all instances of m_i considered here have the same value. The following derivation is done in non-relativistic framework as the targeted merging candidates are below 1 keV (electron velocity at approximately 0.06c). Conservation of mass, momentum and energy before

(LHS) and after (RHS) merging gives

$$\begin{aligned}\sum_{i=1}^{n} w_i m_i &= W_\mathrm{n} m_i = W_1 m_i + W_2 m_i \\ \sum_{i=1}^{n} w_i m_i \mathbf{v}_i &= m_i \mathbf{p}_\mathrm{t} = W_1 m_i \mathbf{V}_1 + W_2 m_i \mathbf{V}_2 \\ \frac{1}{2}\sum_{i=1}^{n} w_i m_i \|\mathbf{v}_i\|^2 &= \frac{1}{2} m_i \epsilon_\mathrm{t} = \frac{1}{2} W_1 m_i \|\mathbf{V}_1\|^2 + \frac{1}{2} W_2 m_i \|\mathbf{V}_2\|^2.\end{aligned}$$

Factoring the above equations yield

$$\begin{aligned}W_\mathrm{n} &= W_1 + W_2 \\ \mathbf{p}_\mathrm{t} &= W_1 \mathbf{V}_1 + W_2 \mathbf{V}_2 \\ \epsilon_\mathrm{t} &= W_1 \|\mathbf{V}_1\|^2 + W_2 \|\mathbf{V}_2\|^2.\end{aligned} \tag{4.3}$$

Starting with momentum equation in Eq. 4.3, perform a dot product with $\mathbf{V}_2$ yields

$$\mathbf{p}_\mathrm{t} \cdot \mathbf{V}_2 = W_2 \|\mathbf{V}_2\|^2 + W_1 \mathbf{V}_1 \cdot \mathbf{V}_2.$$

Substituting the above expression into the energy equation will obtain

$$\epsilon_\mathrm{t} = W_1 \|\mathbf{V}_1\|^2 + \mathbf{p}_\mathrm{t} \cdot \mathbf{V}_2 - W_1 \mathbf{V}_1 \cdot \mathbf{V}_2.$$

Continue by substituting the expression of $\mathbf{V}_2$ and W_2, thus getting

$$\epsilon_\mathrm{t} = \left(W_1 + \frac{W_1^2}{W_\mathrm{n} - W_1}\right)\|\mathbf{V}_1\|^2 - 2\frac{W_1}{W_\mathrm{n} - W_1}\mathbf{p}_\mathrm{t} \cdot \mathbf{V}_1 + \frac{\|\mathbf{p}_\mathrm{t}\|^2}{W_\mathrm{n} - W_1}.$$

Rearranging the expression into

$$0 = \left(W_1 + \frac{W_1^2}{W_\mathrm{n} - W_1}\right)\|\mathbf{V}_1\|^2 - 2\frac{W_1}{W_\mathrm{n} - W_1}\|\mathbf{V}_1\|\mathbf{p}_\mathrm{t} \cdot \hat{\mathbf{V}}_1 + \frac{\|\mathbf{p}_\mathrm{t}\|^2}{W_\mathrm{n} - W_1} - \epsilon_\mathrm{t}.$$

Thus obtaining the solution to $\|\mathbf{V}_1\|$ as

$$\|\mathbf{V}_1\| = \frac{1}{W_\mathrm{n}}\left(\mathbf{p}_\mathrm{t} \cdot \hat{\mathbf{V}}_1\right) \pm \frac{1}{W_\mathrm{n}}\sqrt{\left(\mathbf{p}_\mathrm{t} \cdot \hat{\mathbf{V}}_1\right)^2 - \frac{W_\mathrm{n}}{W_1}\|\mathbf{p}_\mathrm{t}\|^2 + \left(\frac{W_\mathrm{n}^2}{W_1} - W_\mathrm{n}\right)\epsilon_\mathrm{t}}. \tag{4.4}$$

Shifting the attention to the second term in the solution, ensuring the expression remains real yields

$$0 \leq (\mathbf{p}_\mathrm{t} \cdot \hat{\mathbf{V}}_1)^2 - \frac{W_\mathrm{n}}{W_1}\|\mathbf{p}_\mathrm{t}\|^2 + \left(\frac{W_\mathrm{n}^2}{W_1} - W_\mathrm{n}\right)\epsilon_\mathrm{t}.$$

Noting that

$$\mathbf{p}_\mathrm{t} \cdot \hat{\mathbf{V}}_1 = \|\mathbf{p}_\mathrm{t}\| \cos\hat{\theta},$$

the expression becomes

$$\begin{aligned} 0 &\leq \|\mathbf{p}_\mathrm{t}\|^2 \cos^2\hat{\theta} - \frac{W_\mathrm{n}}{W_1}\|\mathbf{p}_\mathrm{t}\|^2 + \left(\frac{W_\mathrm{n}^2}{W_1} - W_\mathrm{n}\right)\epsilon_\mathrm{t} \\ \cos^2\hat{\theta} &\geq \frac{W_\mathrm{n}}{W_1} - \left(\frac{W_\mathrm{n}^2}{W_1} - W_\mathrm{n}\right)\frac{\epsilon_\mathrm{t}}{\|\mathbf{p}_\mathrm{t}\|^2} \\ \hat{\theta} &\geq \cos^{-1}\sqrt{\frac{W_\mathrm{n}}{W_1} - \left(\frac{W_\mathrm{n}^2}{W_1} - W_\mathrm{n}\right)\frac{\epsilon_\mathrm{t}}{\|\mathbf{p}_\mathrm{t}\|^2}} \end{aligned} \tag{4.5}$$

Naturally, the next step is to ensure that the expression within the square root is greater than zero. As W_n, ϵ_t, and $\mathbf{p}_\mathrm{t}$ is already known, this provides a limit to the values that can be assigned to w_1.

$$\begin{aligned} \frac{W_\mathrm{n}}{W_1} - \left(\frac{W_\mathrm{n}^2}{W_1} - W_\mathrm{n}\right)\frac{\epsilon_\mathrm{t}}{\|\mathbf{p}_\mathrm{t}\|^2} &> 0 \\ W_\mathrm{n} - W_\mathrm{n}^2\frac{\epsilon_\mathrm{t}}{\|\mathbf{p}_\mathrm{t}\|^2} &> -W_\mathrm{n}W_1\frac{\epsilon_\mathrm{t}}{\|\mathbf{p}_\mathrm{t}\|^2} \\ W_1 &> W_\mathrm{n} - \frac{\|\mathbf{p}_\mathrm{t}\|^2}{\epsilon_\mathrm{t}}. \end{aligned} \tag{4.6}$$

It is interesting to note that

$$W_\mathrm{n} - \frac{\|\mathbf{p}_\mathrm{t}\|^2}{\epsilon_\mathrm{t}} \geq 0 \tag{4.7}$$

is always true and the proof is provided in the following discussion. The idea is to compare the maximum possible value of $\|\mathbf{p}_\mathrm{t}\|^2/\epsilon_\mathrm{t}$ with the total merging candidate's weight W_n. Should such maximised value be equal to W_n, Eq. 4.7 is unconditionally fulfilled.

Assuming the case with two merging candidates (with w_1, $\mathbf{v}_1$ and w_2, $\mathbf{v}_2$ respectively) and consider once again the expressions of $\mathbf{p}_\mathrm{t}$ and ϵ_t, which are

$$\begin{aligned} \sum_{i=1}^{n} w_i\mathbf{v}_i &= \mathbf{p}_\mathrm{t} \\ \sum_{i=1}^{n} w_i\|\mathbf{v}_i\|^2 &= \epsilon_\mathrm{t} \end{aligned}$$

$$\frac{\|\mathbf{p}_\mathrm{t}\|^2}{\epsilon_\mathrm{t}} = \frac{w_1^2\|\mathbf{v}_1\|^2 + w_2^2\|\mathbf{v}_2\|^2 + 2w_1w_2(\mathbf{v}_1\cdot\mathbf{v}_2)}{w_1\|\mathbf{v}_1\|^2 + w_2\|\mathbf{v}_2\|^2}. \tag{4.8}$$

As the candidate selection by energy (Sec. 4.2.3) provides a narrow variance in the candidate's energy range, a simplifying assumption is made such that the candidates' velocity magnitudes are equal ($\|\mathbf{v}_1\| = \|\mathbf{v}_2\|$). It is known from the Cauchy-Schwarz inequality that

$$\mathbf{v}_1\cdot\mathbf{v}_2 \leq \|\mathbf{v}_1\|\|\mathbf{v}_2\|. \tag{4.9}$$

Hence, in order to maximise the third term of the numerator in Eq. 4.8, the merging candidates' velocity vectors are necessarily parallel to each other. This results in

$$\frac{\|\mathbf{p}_\mathrm{t}\|^2}{\epsilon_\mathrm{t}} = \frac{(w_1^2 + w_2^2 + 2w_1w_2)}{(w_1 + w_2)} = W_\mathrm{n}. \tag{4.10}$$

In reality, it is highly unlikely that the merging candidates' velocity vector is parallel to each other. Inferring from Eq. 4.8, Eq. 4.9 and Eq. 4.10,

$$\frac{\|\mathbf{p}_\mathrm{t}\|^2}{\epsilon_\mathrm{t}} \leq W_\mathrm{n}$$

is true (which is identical to Eq. 4.7).

Eq. 4.10 remains true for an arbitrarily large n merging candidates. Finally, the expression in Eq. 4.6 shows that $W_1 = W_\mathrm{n}/2$ is a valid choice in most cases during merging events and it is defined as the default weight distribution between super-particles. Should the condition be violated, W_1 is redefined to be at least $W_\mathrm{n} - \frac{\|\mathbf{p}_\mathrm{t}\|^2}{\epsilon_\mathrm{t}}$. Since this derivation doesn't enforce equal splitting of the super-particles' weights, merging of odd numbered candidates will always allow integer weight splits between the super-particles while still respecting the conservation laws. This simplifies the calculation of weight splitting of such super-particles in the future, without having to consider fractional weights.

At this point, W_1 and $\hat{\theta}$ is obtained (Eq. 4.5 and Eq. 4.6) which enables the calculation of $\hat{\mathbf{V}}_1$. The method to compute $\hat{\mathbf{V}}_1$ borrows from the work of Vranic *et al.*. Introducing unit vector $\hat{\mathbf{d}}$, which is parallel to the n candidates' maximum absolute value in v_x, v_y, and v_z while retaining the signs. $\hat{\mathbf{V}}_1$ then deviates from $\hat{\mathbf{p}}_\mathrm{t}$ by angle $\hat{\theta}$ along the plane bounded by both $\hat{\mathbf{p}}_\mathrm{t}$ and $\hat{\mathbf{d}}$ vectors. The velocity magnitude of the first super-particle can now be calculated from Eq. 4.4. The solution to $\mathbf{V}_2$ is then

$$\mathbf{V}_2 = \frac{1}{W_2}(\mathbf{p}_\mathrm{t} - W_1\mathbf{V}_1) \tag{4.11}$$

with W_2 follows directly from mass conservation. Finally, the super-particle's spatial location is chosen at random from the pool of merging candidates.

4.4 Benchmark of the merging algorithm

A series of tests are presented here to gauge the performance of the implemented merging algorithm. The tests aim to analyse the impact of two discussed candidate selection criteria, namely the energy and momentum unit vector selection, on simulated particles' overall energy and momentum distribution preservation. The series of tests are split

into two setups.

The first is purely on repeated merging instances of artificially created merging candidates, a setup which allows complete control over the merging candidates' energy and momentum distribution. In this setup, the created candidates have all passed the locality and species filters. The results for this setup are presented in Sec. 4.4.1, Sec. 4.4.2, and Sec. 4.4.3.

The second setup involves merging tests on a charged particle system in a tokamak setting, where the merging candidates are extracted from a prior plasma initiation simulation. Conservation of the energy distribution after the merging process is tested. The particles are assumed to be collisionless and are not accelerated by any electric field, this ensures that the total energy of the system is constant in time. Only the background magnetic field is active, confining the particles within the toroidal geometry. The results for this setup are discussed in Sec. 4.4.4.

4.4.1 Influence of merging candidates sample size on total energy and momentum

The focus of this benchmark is to test the merging algorithm's ability to conserve the merging candidates' total energy and momentum, when S number of merging candidates with the same mass are merged into 2 super-particles. The tests are also conducted with all S merging candidates sharing the same energy $\varepsilon_{\mathrm{mc}}$, mimicking the candidates that have passed the energy selection criterion. Referring to Fig. 4.4, all particles are initiated with a random velocity vector oriented in the range of $\phi = [0, \pi/2]$ and $\theta = [0, \pi/2]$. This specific setup is a simplified representation of the merging candidates that have passed all of the discussed selection criteria in Sec. 4.2. Specifically, a defined energy proximity of $\varepsilon_{\mathrm{mc}}$ and the angular resolution of $\Delta\Omega = \pi/2$ for the momentum unit vector selection.

The merging candidates themselves are all fixed to the weight of 1 as well, representing the first instance of merging event during a simulation. The test is conducted with $\varepsilon_{\mathrm{mc}} = [10\,\mathrm{eV}, 100\,\mathrm{eV}, 1000\,\mathrm{eV}]$ and $S = [10, 50, 100, 500, 1000]$. For each of the combinations of S and $\varepsilon_{\mathrm{mc}}$, the difference of total energy and momentum before and after merging is plotted.

Fig. 4.6 and Fig. 4.7 show the mean and standard deviation of the total energy and

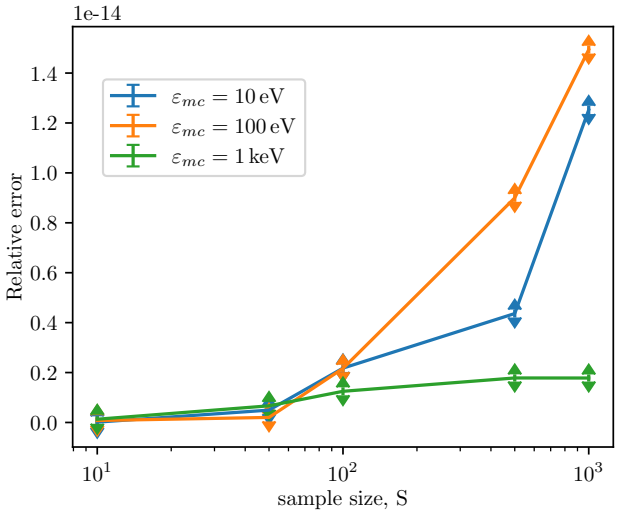

FIGURE 4.6: Relative error of total energy for $S = [10, 50, 100, 500, 1000]$ at various $\varepsilon_{\mathrm{mc}}$.

momentum magnitude differences after merging. The measure of relative error is calculated by

$$\begin{aligned} \text{Relative error}_{\text{energy}} &= \frac{(\epsilon_{\mathrm{t}} - \varepsilon_{\mathrm{mc}} S)}{\varepsilon_{\mathrm{mc}} S} \\ \text{Relative error}_{\text{momentum}} &= \frac{(\mathbf{p}_{\mathrm{t}} - \sum_i^S \sqrt{2 m_i \varepsilon_{\mathrm{mc}}})}{\sum_i^S \sqrt{2 m_i \varepsilon_{\mathrm{mc}}}}, \end{aligned} \tag{4.12}$$

where ϵ_{t} and $\mathbf{p}_{\mathrm{t}}$ are the super-particles' total energy and momentum respectively (see Eq. 4.3). In Fig. 4.6, a general trend of deterioration in the conservation of total energy is observed as S increases. It is also observed that $\varepsilon_{\mathrm{mc}}$ has minor impact on the magnitude of relative error for $S = 50$ and below. This helps confirm that having a smaller sample S for each merging instance yields better performance in energy conservation. On the other hand, Fig. 4.7 shows that the momentum conservation of the merging process is largely independent of both S and $\varepsilon_{\mathrm{mc}}$. Relative error magnitude of both energy and momentum suggests that the computed values are near machine-precision, which is interpreted as the algorithm's ability to conserve energy and momentum. It is worth mentioning that all the resulting super-particles across all scenarios have the same weights, which is exactly $W_1 = W_2 = S/2$. Thus, implying that the conservation of mass is satisfied as well.

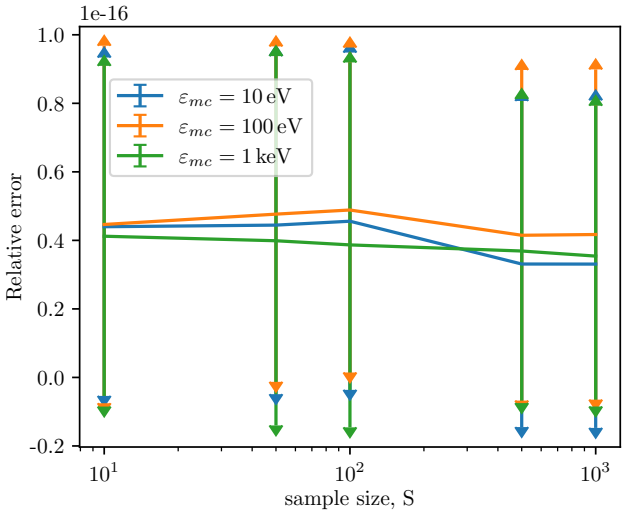

FIGURE 4.7: Relative error of total momentum magnitude for $S = [10, 50, 100, 500, 1000]$ at various $\varepsilon_{\mathrm{mc}}$.

4.4.2 Influence of $\Delta\Omega$ on super-particle $\Delta\varepsilon$

The previous section had proven that the algorithm preserves the total energy and momentum of the merging candidates, but did not explore how the candidates' energy is distributed among the two super-particles. The aim of this section is to examine the impact of the chosen angular resolution $\Delta\Omega$ in the momentum unit vector selection criterion on the shift of the resulting super-particles' energy per weight. The energy per weight of a super-particle is labelled as $\varepsilon_{\mathrm{sp}}$ in this section.

First, revisiting the merging algorithm in Sec. 4.3 is helpful to understand the motivation of using the $\varepsilon_{\mathrm{sp}}$ (energy per weight) measure. The energy balance equation in Eq. 4.3 is equivalent to

$$\sum_{i=1}^{n} w_i \|\mathbf{v}_i\|^2 = W_1 \|\mathbf{V}_1\|^2 + W_2 \|\mathbf{V}_2\|^2. \tag{4.13}$$

By creating merging candidates which all have the same energy $\varepsilon_{\mathrm{mc}}$, velocity magnitudes of all merging candidates are also the same $\|\mathbf{v}_i\| = \|\mathbf{v}\|$. Eq. 4.13 can be simplified to

$$W_{\mathrm{n}} \|\mathbf{v}\|^2 = W_1 \|\mathbf{V}_1\|^2 + W_2 \|\mathbf{V}_2\|^2.$$

The choice was made in Sec. 4.3 that the weights of the super-particles are distributed equally $W_1 = W_2 = W_n/2$, thus further simplifying the equation to

$$2\|\mathbf{v}\|^2 = \|\mathbf{V}_1\|^2 + \|\mathbf{V}_2\|^2. \tag{4.14}$$

Noting that the total energy before and after merging is conserved (from Sec. 4.4.1), implying that should $\|\mathbf{V}_1\|^2 = \|\mathbf{v}\|^2 + \Delta\varepsilon$, $\|\mathbf{V}_2\|^2 = \|\mathbf{v}\|^2 - \Delta\varepsilon$ must be true. Eq. 4.14 can be augmented into

$$\|\mathbf{v}\|^2 + \|\mathbf{v}\|^2 = \left(\|\mathbf{V}_1\|^2 - \Delta\varepsilon\right) + \left(\|\mathbf{V}_2\|^2 + \Delta\varepsilon\right). \tag{4.15}$$

Therefore, if energy deviation $\Delta\varepsilon$ exists between the super-particles, it is obtained through the difference between the energy of the merging candidate $\varepsilon_{mc}(\|\mathbf{v}\|)$ and the energy per weight of the super-particles $\varepsilon_{sp}(\|\mathbf{V}\|)$.

The first test involves obtaining the distribution of $\Delta\varepsilon$. A small sample of merging candidates $S = 4$ is once again created with their unit vectors distributed randomly in $\phi = [0, \pi/2]$ and $\theta = [0, \pi/2]$ (corresponding to $\Delta\Omega = \pi/2$), while defining the $\varepsilon_{mc} = 10\,\text{eV}$. The $\Delta\varepsilon$ for each super-particle is computed and recorded. This process is then repeated for $N_{rep} = 10\,000$ times and the histogram of $\Delta\varepsilon$ for each super-particle is plotted in Fig. 4.8. The symmetry at $\Delta\varepsilon = 0$ is expected from the total energy conservation. As such, the following results report the $|\Delta\varepsilon|$ of only one super-particle.

Increasing the number of merging candidates $S = 100$ and 1000 showed that the mean $\Delta\varepsilon$ is independent of S, but only reduces its standard deviation (seen from Fig. 4.9 and 4.10). It would be interesting now to study the impact of $\Delta\Omega$ and ε_{mc} on the $\Delta\varepsilon$ mean, the goal is to identify the variables that can minimise such deviations. Therefore, the next set of tests is conducted with $\Delta\Omega = [\pi/2, \pi/4, \pi/8, \pi/16, \pi/32]$ in combination with $\varepsilon_{mc} = [1, 10, 100, 1000]$.

Fig. 4.11 shows that $\Delta\varepsilon$ scales proportionally with ε_{mc}. At the same time, the mean $\Delta\varepsilon$ reduces in accordance with convergence of $\mathcal{O}(\Delta\Omega^2)$. In particular, $\Delta\Omega = \pi/16$ consistently results in mean $\Delta\varepsilon$ that is 2 orders of magnitude lower than the given ε_{mc} (mean $\Delta\varepsilon \approx 10\,\text{eV}$ for $\varepsilon_{mc} = 1\,\text{keV}$).

The choice of $\Delta\Omega$ during a merging process can now be determined from the resolution of the energy groupings itself. As an example, examining all the cross sections listed in App. A, it is clear that the finest energy resolution at the energy level of approximately 1 keV is 50 eV. Therefore, the choice of $\Delta\Omega = \pi/2$ or $\pi/4$ isn't suitable, as they introduce $\Delta\varepsilon \approx 400\,\text{eV}$ and 140 eV respectively. One is then free to choose from $\Delta\Omega = \pi/8$ or

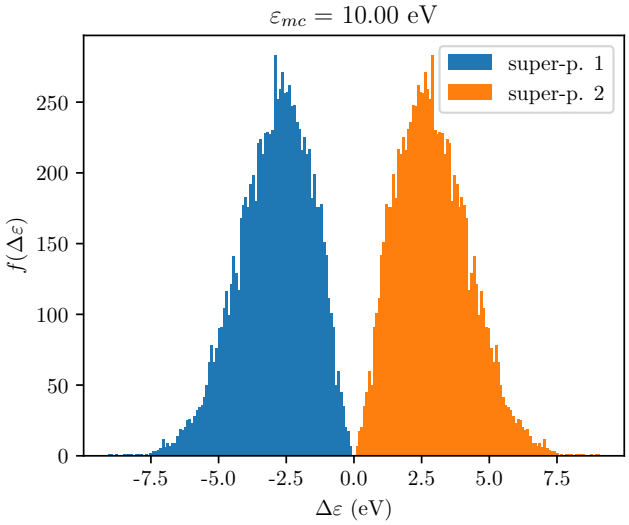

FIGURE 4.8: Histogram of $\Delta\varepsilon$ for super-particle 1 and 2 where $N_{\text{rep}} = 10\,000$ with $\varepsilon_{\text{mc}} = 10\,\text{eV}$ and $S = 4$. The initial merging candidates are initiated with their unit vector distributed in the range of $\phi = [0, \pi/2]$ and $\theta = [0, \pi/2]$.

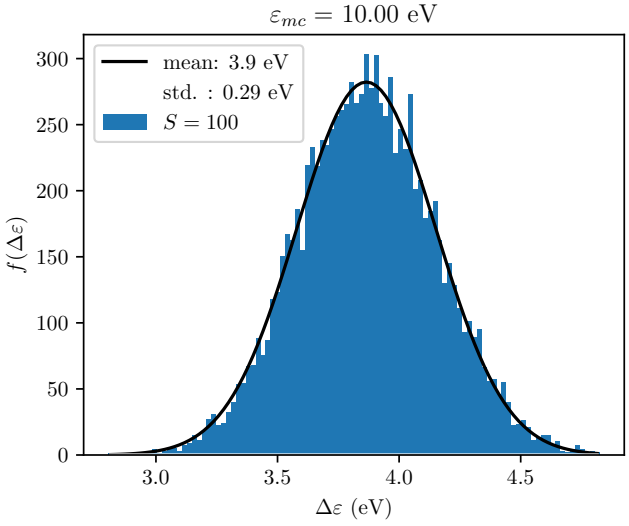

FIGURE 4.9: Distribution of $\Delta\varepsilon$ with $S = 100$, accompanied by a fitted Gaussian.

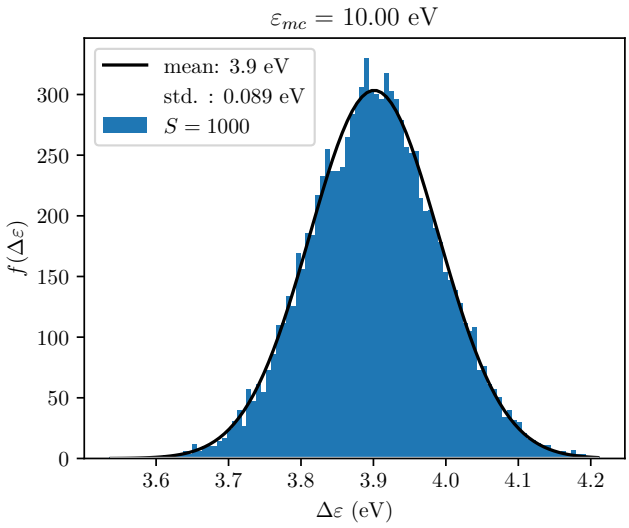

FIGURE 4.10: Distribution of $\Delta\varepsilon$ with $S = 1000$, accompanied by a fitted Gaussian.

less, in order to ensure that the resulting $\Delta\varepsilon$ stays within the resolution of the available cross section data. A minor caution is mentioned here, that the merging algorithm's effectiveness in reducing the number of simulated particles diminishes with finer angular resolution.

4.4.3 Influence of $\Delta\Omega$ on super-particle momentum

The previous section explored the changes in the super-particles' energy per weight when compared to the initial $\varepsilon_{\mathrm{mc}}$ of the merging candidates. In this section, another aspect of the alteration is explored, specifically the orientation of the merged super-particle momentum. Recall in Eq. 4.5 that an angle $\hat{\theta}$ is introduced, which is a by-product of momentum conservation. While one could not avoid such deviation, it is helpful to establish the relationship between $\hat{\theta}$ distribution and $\Delta\Omega$. This ensures that the resulting trajectories of the super-particles are approximately aligned to the orientation of the momentum selection group. As mentioned before, all instances of merging will split the weight between the super-particles evenly and this would mean that the angle between $\hat{\mathbf{p}}_{\mathrm{t}}$ and $\hat{\mathbf{v}}_2$ will also be approximately the same. Introducing a new variable

$$\theta' = \cos^{-1}(\hat{\mathbf{v}}_1 \cdot \hat{\mathbf{v}}_2), \tag{4.16}$$

this measures the angle between the velocity unit vectors of the two super-particles and it should be approximately double the value of $\hat{\theta}$. The test will also compute this value

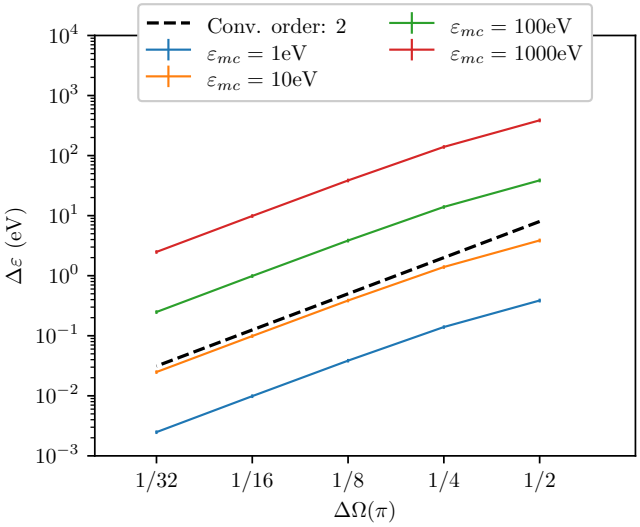

FIGURE 4.11: Fitted $\Delta\varepsilon$ mean with $S = 100$ at various $\varepsilon_{\mathrm{mc}}$, compared with ideal scaling of convergence order $\mathcal{O}(\Delta\Omega^2)$.

for comparison and verification. The test is conducted in similar fashion to Sec. 4.4.2, except that the resulting angles are found to be independent of $\varepsilon_{\mathrm{mc}}$ (thus not plotted). Since the distribution of both $\hat{\theta}$ and θ' are Gaussians, the mean value of both parameters is obtained via Gaussian fitting. The result is plotted along with its standard deviation in Fig. 4.12. Both $\hat{\theta}$ and θ' have the order of convergence of approximately $\mathcal{O}(\Delta\Omega^1)$. The values of $\hat{\theta}$ are indeed approximately half of θ' as well. Even though the resulting total momentum magnitude is conserved during the merging process, the introduced angular deviation from $\hat{\mathbf{p}}_{\mathrm{t}}$ is something to be aware of.

4.4.4 Conservation of energy in tokamak scenario

The goal of this test is to determine the merging algorithm's ability to preserve the energy distribution of the particle system after multiple instances of merging. This will also be the first test conducted within a toroidal geometry, where the particles are moving around the torus with a predefined velocity distribution. This is different from the tests done in Sec. 4.4.1 and 4.4.2, as those already assumed that the merging candidates have passed all the discussed selection criteria in Sec. 4.2. As such, this section presents the first instance where the whole process from merging candidates selection to the merging algorithm is applied to a toroidal domain.

A description of the tokamak setup is given here, before the results are discussed. A

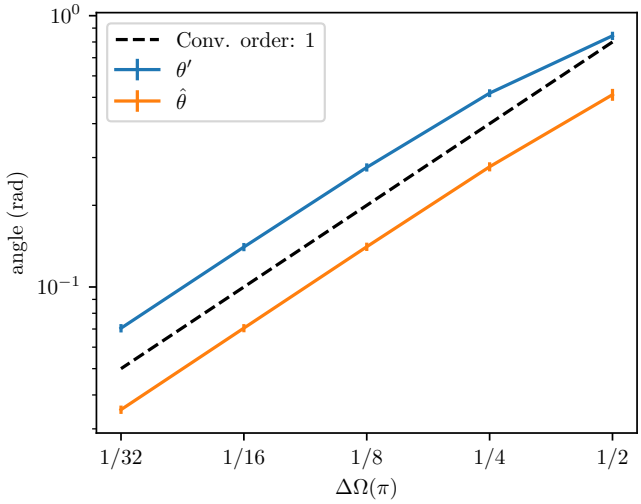

FIGURE 4.12: Fitted mean values with $S = 100$ at various $\Delta\Omega$, compared with ideal scaling of convergence order $\mathcal{O}(\Delta\Omega^1)$.

H_2 Pressure (Pa)	0.002
Wall temperature (K)	373.15
Initial electron number	1000
Major radius (m)	5.8
Minor radius of simulated domain (m)	1.75

TABLE 4.1: ITER-like tokamak parameters and operating condition.

numerical simulation of Townsend avalanche breakdown is conducted in a tokamak with dimensions and the initial conditions listed in Tab. 4.1. The electrons are seeded within the torus homogeneously, while continuously subjected to a background electric field with an averaged strength of $0.6\,\mathrm{V\,m^{-1}}$, aligned in the toroidal direction. The electrons are also subjected to a static background magnetic field in the toroidal direction, and its magnitude distribution shown in Fig. 4.13. The simulation included cross sections listed in App. A. At the simulated time of approximately 0.767 ms, the simulation reached approximately 4×10^6 charged particles (half of which are electrons).

This set of particles is then subjected to extended simulation run, but the background electric field and the cross sections are removed. As such, the charged particles will retain their energy distribution while having zero collisions. The particles are allowed to traverse their confined pathway around the torus over a duration of 8.75 µs and a total of 3 merging processes are applied at equal time intervals. Repeated merging performed onto the given electron population should preserve the initial total energy. Hence, this

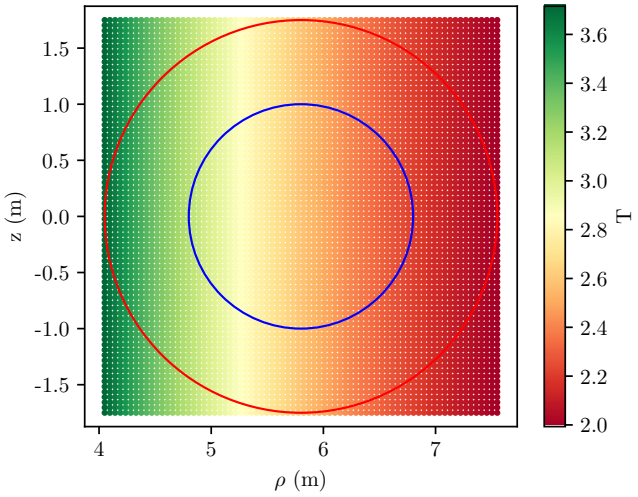

FIGURE 4.13: Toroidal magnetic field strength in the poloidal plane. $B_\phi = 2.6\,\mathrm{T}$ at $\rho = 5.8\,\mathrm{m}$.

can be a good measure to check if any 'heating' or 'cooling' due to merging algorithm can be identified.

Before deciding on the spatial resolution for the spatial proximity selection criterion, the averaged number of local particles at each parent (subdivision) level are computed. The final choice of subdivision level for merging is made based on the ratio of local particles and merging groups, satisfying

$$r_{\mathrm{merge}} \geq \frac{\text{local particles count}}{\text{merging group count}}. \tag{4.17}$$

The number of merging groups is a product of number of species (species selection criterion), number of energy groups (energy proximity selection), and number of angular groupings (momentum unit vector selection). As an example, assuming the particle system included 3 species, with a total of 200 energy groups and a total of 8 angular groups (at chosen angular resolution of $\pi/2$), the total number of merging groups is 4800. The r_{merge} is set to 4, such that the number of minimum merging candidates is $S = 4$ merging into two super-particles. In the case when the particle system has a low number density, there is a possibility that the chosen level only has eight spatial groups (or less) subdividing the whole simulation domain. Therefore, a minimum subdivision level of 6 (or $\left(2^6\right)^3$ spatial groups) is enforced so that there are at least 7 spatial groups across radial and z direction of the torus section with a minor radius of 1.75 m. The test is also conducted with two different $\Delta\Omega$ at $\pi/2$ and $\pi/16$ (for both ϕ and θ) in the

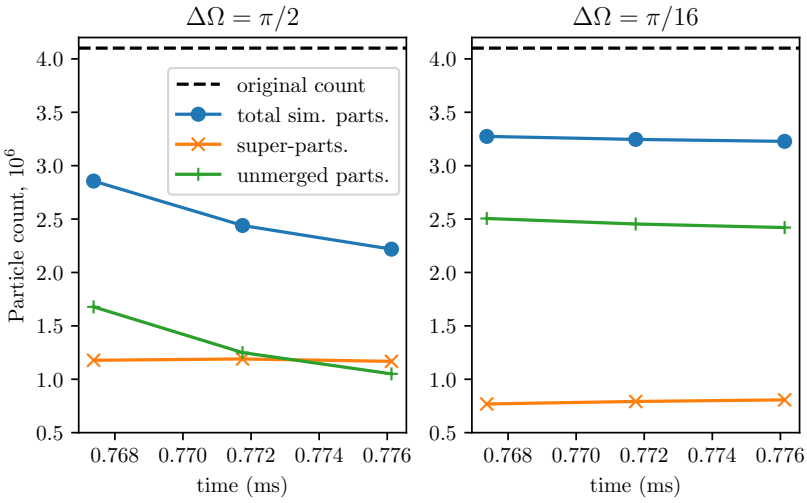

FIGURE 4.14: Breakdown of the merged super-particles and the unmerged individual particles population after each merging process.

momentum selection step.

The results shown in Fig. 4.14 depict the number of simulated particles after each merging process. It has to be mentioned that both the case of $\Delta\Omega = \pi/2$ and $\pi/16$ ended up performing spatial proximity selection at subdivision level 6 due to the low particle number density (at approximately $10^5\,\mathrm{m}^{-3}$). It is observed that the merging setting that uses $\Delta\Omega = \pi/2$ shows a larger reduction of simulated particles per merging step. In comparison, the case of $\Delta\Omega = \pi/16$ shows that the number of simulated particles remained stagnant after the first instance of merging. Looking at the total super-particle count for both $\Delta\Omega = \pi/2$ and $\pi/16$, both remained stagnant after the first merging step with $\Delta\Omega = \pi/2$ reporting a higher number of super-particles. This can be explained by the difference in number of candidate groupings between the two cases during the momentum unit vector selection step. At the angular resolution of $\pi/2$, the total number of momentum groups created is at 8 while the resolution of $\pi/16$ amounts to 512. Both cases have the same initial local particle number (from spatial proximity selection), but there are higher number of particles in the $\pi/16$ case which occupies its own merging candidate group, thus cannot be merged (higher unmerged particles, lower super-particles). The number of super-particles in the case of $\Delta\Omega = \pi/2$ doesn't increase despite reporting lower unmerged particles over time, it is due to the particles merging into existing super-particles (raising the weights of the super-particles).

On the aspect of total energy conservation, it is shown in Fig. 4.15 that the relative error

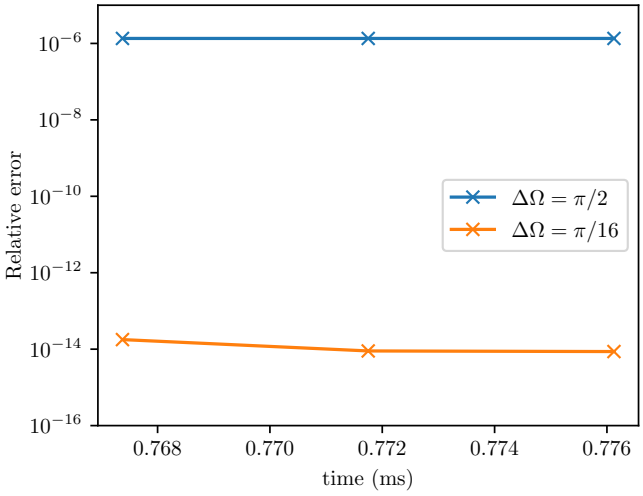

FIGURE 4.15: Relative error of total energy with different $\Delta\Omega$.

remains relatively constant after the first instance of merging. Among the two merging setups, the case with an angular resolution of $\pi/16$ shows a lesser degree of deviation from the initial set of particles, only having its relative errors at the order of magnitude of 10^{-14}. This meant that the $\Delta\Omega$ plays a larger role in affecting the total energy conservation when the global particles are non-monochromatic in energy. This is further reinforced by Fig. 4.16, showing the error comparison of energy across the initially given energy distribution. It is clear that $\Delta\Omega = \pi/2$ is unable to properly preserve the original energy distribution, introducing changes of up to $-95\,\%$ of the original electron population with approximately 1 keV. This is the direct consequence of $\Delta\varepsilon$ as described in Sec. 4.4.2. The effect of the energy deviation doesn't expand past kinetic energy of 1 keV for the sole reason that merging doesn't occur for particles that are above 1 keV. There are occasional spikes of error above 1 keV, but that can be attributed to the initially low population of energetic particles (poor statistical significance).

The result in Fig. 4.16 clearly shows that having $\Delta\Omega = \pi/16$ largely avoided the issue of energy deviation. This further agrees with the conclusion made in Sec. 4.4.2, that a proper choice of $\Delta\Omega$ (which limits the $\Delta\varepsilon$ below the energy resolution of considered cross section data) can preserve the energy distribution of the given particle system. However, the cost of conducting the merging at such resolution is the reduced effectiveness of total simulated particles reduction.

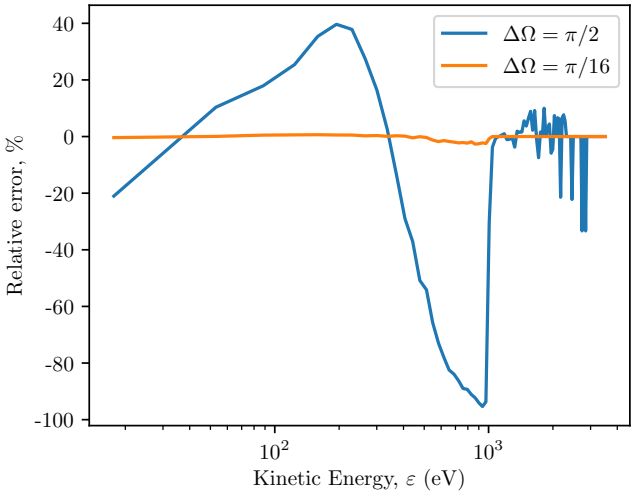

FIGURE 4.16: Relative error of electron kinetic energy distribution between the benchmark and the merging cases with its respective $\Delta\Omega$.

4.5 Super-particle collision events

With the introduction of super-particles to the simulation, special care is required to handle the $e-H_2$ collision events. One could simply evaluate Eq. 3.10 once for every super-particle and replicate the results based on its weight W. This method is predicated on the assumption that the number of super-particles is abundant enough to correct the crude evaluation of the collision outcome. Therefore, a conscious choice was made to repeat the evaluation for the collision outcome corresponding to the weight of the super-particle instead. For example, a super-particle with the weight of 10 would then have 10 evaluations of its collision probability, using the super-particle's energy per weight. The total number of each collision outcome is recorded and the splitting of the super-particle is done. The newly created super-particles will have their weights defined by the number of evaluated outcomes. Revisiting the example of a super-particle with a weight of 10, assuming that 5 evaluations return elastic scattering and the rest resulted in vibrational excitation, two new super-particles with the weight of 5 each will be created. One of the two super-particles will have diminished energy due to the energy loss from the excitation. For each resulting super-particle, the treatment of the post-collision velocity vector follows the chosen scattering angle implementation described in Sec. 3.4.2.

While it is true that repeated collision evaluations based on the weight of the super-particle once again introduce computational costs, it represents less than 1 % of the overall cost involved within a time step. The computation cost of electrostatic field among

charged particles far exceeds the collision evaluations, stemming from the $\mathcal{O}(n \log n)$ scaling of the Barnes-Hut algorithm. The time saved on the field evaluation from reduction of n due to merging far outweighs the collision evaluations.

4.6 Benchmark of the super-particle ionisation

In this section, the impact of merging to charged particle growth over time due to impact ionisation is shown. The initial set of particles is once again the same as those described in Sec. 4.4.4. The initial time of the data set is at 0.767 ms and continues to be simulated to the end point of 0.942 ms. Instead of removing the toroidal electric field and the cross sections as in Sec. 4.4.4, all of the simulation components remain active. Additionally, the merging algorithm described in Sec. 4.3 as well as the merging candidate selection criteria in Sec. 4.2 is applied. Specifically, the momentum unit vector selection is done with $\Delta\Omega = [\pi/2, \pi/4, \pi/8, \pi/16]$.

In order to provide the time for particles at all levels of energy to gain sufficient energy (thus shuffling the merging candidates during energy grouping) before the next merging step, the merging is limited to once every 4.375 µs. The interval spacing is also required as the effectiveness of merging greatly diminishes if done at every step, since the merging candidates are almost the same set from the previous step. The simulations of both with and without merging are then compared in the aspect of the electron population over time as well as their overall energy distribution. As a reference, the resulting time between collisions obtained from Eq. 3.14 would be in the order of 1.451 µs assuming the electron carries an energy of 3.25 eV (peak total scattering cross section value of $16.6 \times 10^{-20}\,\mathrm{m}^{-2}$) with the listed parameters in Tab. 4.1. This would mean that all electrons would have collided with a background neutral molecule at least once by the time the merging process is performed once, further shuffling the set of particles within the momentum unit vector selection criterion. Finally, the simulations of both with and without merging are then compared in the aspect of the electron population over time as well as their overall energy distribution.

Fig. 4.17 shows the comparison of electron population over time between the merging tests with various $\Delta\Omega$ and the benchmark unmerged simulation. It shows that all the merging cases manage to approximate the exponential growth rate of the benchmark to some varying degree of success. It would seem that the case of $\Delta\Omega = \pi/4$ and $\pi/8$ performed the worst. It is difficult to decide the best approximation between the remaining two cases. It seems that the growth rate is artificially exaggerated initially but then

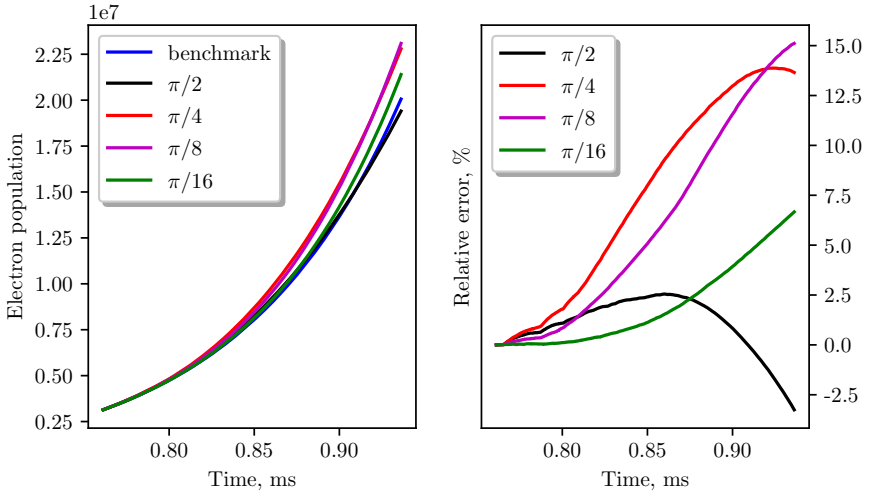

FIGURE 4.17: The electron growth over with various $\Delta\Omega$ in the momentum selection resolution, the respective relative errors compared to the case without merging are also shown.

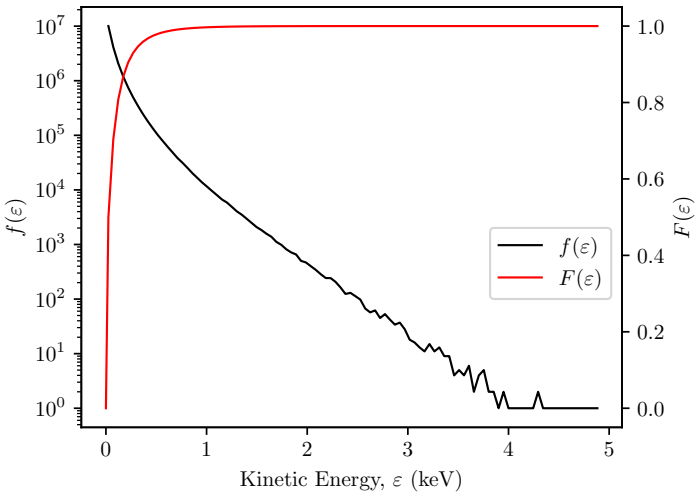

FIGURE 4.18: Electron energy distribution from scenario 0 of the tokamak avalanche breakdown simulation at 0.942 ms. Left axis denotes the electron energy distribution $f(\varepsilon)$ and the right axis is the corresponding cumulative distribution function $F(\varepsilon)$.

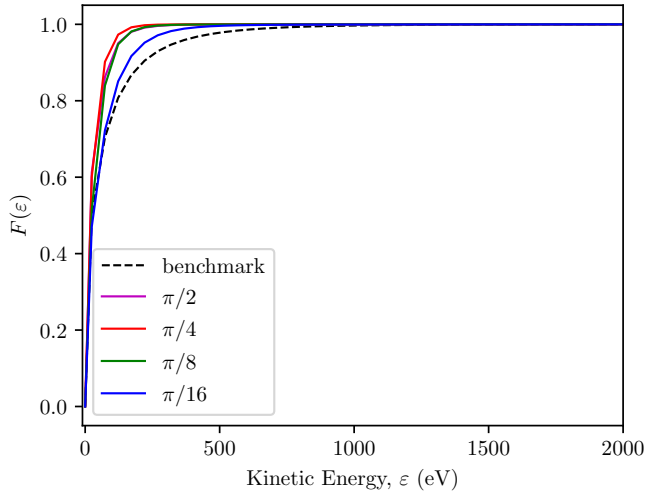

FIGURE 4.19: Cumulative distribution functions of the aforementioned comparisons.

underestimated over time (observed from the case of $\Delta\Omega = \pi/2$ and $\pi/4$). However, the simulated time is limited and proper extrapolation of the growth rate still requires more information from longer simulation runs.

Even though the limited simulation duration provided an inconclusive outcome of which $\Delta\Omega$ yields the best approximation, the comparison of electron kinetic energy distribution can help shed some light. Fig. 4.18 shows the kinetic energy distribution of the electrons for the benchmark unmerged case, as well as its cumulative distribution function. Similar distribution functions are obtained for each $\Delta\Omega$ case and the results are compared in Fig. 4.19.

The results show that the deviation of the electron energy distribution is predominantly in the energy range below 1 keV, which corresponds to the final entry of the candidate selection by energy. While the electron population over time approximation is among the more reasonable by $\Delta\Omega = \pi/2$, the energy distribution approximation is the worst. Most notably, the electron population with energies below ionisation is much higher than the benchmark case, thus suggesting that the growth rate is diminished moving forward in time. The merging case of $\Delta\Omega = \pi/16$ in contrast has the best approximation of the benchmark energy distribution. Thus, able to capture the growth rate more accurately.

This demonstrates that, in the scenario where stochastic scattering and ionisation events are involved, fulfilling the conservation laws (during individual merging events) is insufficient in ensuring the preservation of the energy distribution over time. This is true

even for the case of $\Delta\Omega = \pi/16$, which shows that the energy distribution preservation is good in a scenario when scattering events are removed (see Fig. 4.16). Poor preservation of energy distribution introduces a knock-on effect on the eventual ionisation rate as any minor deviation in the energy distribution will continuously build up. A conscious decision to not extend the tests with $\Delta\Omega < \pi/16$ is made, due to the data set's low initial particle number at only $\sim 4 \times 10^6$. Further increase to the resolution of $\Delta\Omega$ could yield negligible reduction in total simulated particles count (observed from a stagnant count of total simulated particles over time for $\Delta\Omega = \pi/16$ case in Fig.4.14). Existing results are too limited to provide a future estimate of the accuracy of the approximation. The next step is to implement an alternative merging algorithm to see the impact on the growth rate approximation.

4.6.1 Unphysical merge test

The unsatisfactory results shown in Fig. 4.17 open the question of Sec. 4.3 merging algorithm's effectiveness in approximating the correct ionisation rate. In the work of Teunissen *et al.*, it was concluded that scaling the randomly chosen velocity from a pool of merging candidates to fulfil the energy conservation criterion yielded results that provide good approximation of the system's original energy and momentum distribution. As such, the merging algorithm used for this ionisation test follows the same line of thought.

This version of the merging algorithm assumes that both super-particles inherit the same kinetic energy after merging. An assumption is also made such that the weights are both equal, thus $W_1 = W_2 = W_\mathrm{n}/2$. The velocity unit vector for each super-particle is then randomly chosen among its merging candidates. Finally, the velocity magnitude for each of the super-particles is

$$\|\mathbf{V}_1\| = \|\mathbf{V}_2\| = \sqrt{\frac{\epsilon_\mathrm{t}}{W_\mathrm{n}}}. \tag{4.18}$$

This assignment of the super-particles' velocity magnitude and weight distribution guarantees the conservation of charge and energy, but does not respect the momentum of the merging candidates. This method is then tested in a similar setup as described in Sce. 4.6. Additionally, the merging process is conducted with the angular resolution of $\Delta\Omega = \pi/16$. The difference in electron population over time between the benchmark simulation and the unphysical merge case is shown in Fig. 4.20. The prior results from Sec. 4.6 are also included for easy reference.

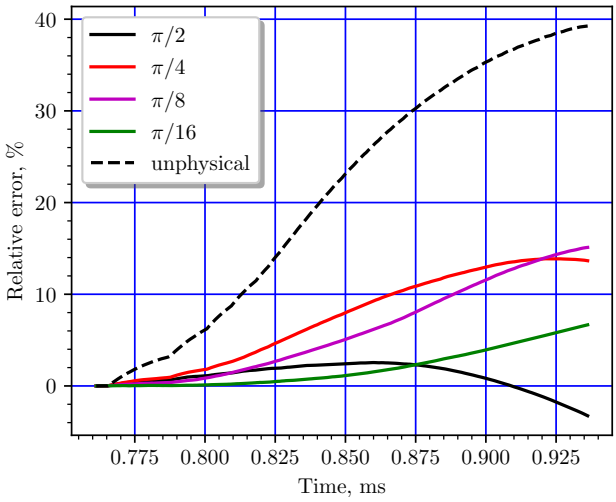

FIGURE 4.20: The comparison of the computed errors in electron population compared to the benchmark unmerged plasma initiation simulation.

Unfortunately, the relative error of electron population's growth rate for this merging algorithm is the worst performing among the merging simulations. The result suggests that the merging algorithm discussed in Sec. 4.3 remains the better option. The focus of further study perhaps lies in the improvement of the super-particle collision and ionisation treatment.

4.7 Compute resources comparison

Even though the growth rate approximation in merging cases is not satisfactory, it is still of interest to examine the potential savings in computational resources. The result presented in Fig. 4.21 is a measure of the total core-hours (defined as the number of hours that a number of compute cores took to complete the simulation) required to complete the simulations, using various $\Delta\Omega$ for the merging events. The set of data is obtained from the simulations described in Sec. 4.6. As a point of reference, the benchmark simulation from the time of 0.767 ms to 0.942 ms required approximately 158k core-hours in total to complete, performed on the JURECA-DC module in Jülich Supercomputing Center.

Fig. 4.21 shows that the coarsest of the chosen $\Delta\Omega$ consumed the smallest amount of core-hours, approximately 41 % of the benchmark case. Even the finest resolution of $\Delta\Omega$

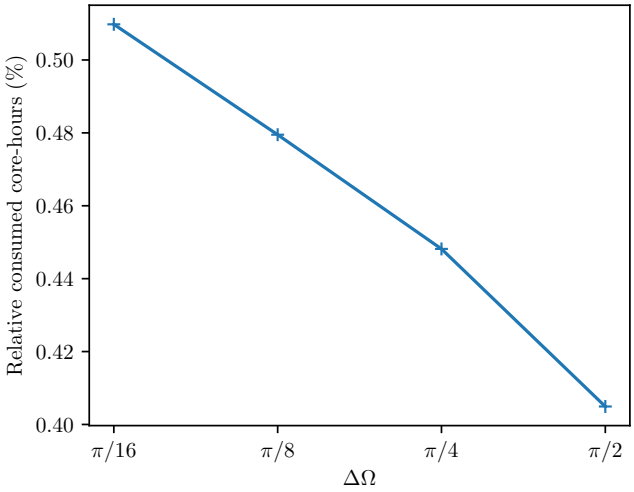

FIGURE 4.21: The relative consumed core-hours for the ionisation simulations with various $\Delta\Omega$, compared to the benchmark case over the same simulated duration.

only required approximately 51 % of the benchmark's core-hours consumption. Naturally, this points to the fact that a more aggressive reduction of simulated particles' number will reduce the corresponding computational cost as well. While one might be tempted to employ aggressive merging for a large reduction in computational cost, there is a theoretical hard limit to the minimal number of simulated particles. Each one of the introduced selection criteria in Sec. 4.2 raises the minimum super-particle counts.

A theoretical count of the final merging candidate groups is presented here, this is an important consideration since each group will have a minimum of 2 super-particles. Assuming that the spatial proximity selection is applied to a collection of particles in 3D at subdivision level 6, the total number of groups is at $(2^6)^3 = 262144$. Further assuming that the particles occupy only one third of the cuboid volume, the number of groups that contain particles then reduces to $\sim$ 87381. Next, assuming that the resolution of $\Delta\Omega = \pi/2$ is chosen for momentum selection, this results in 8 groups for each individual spatial group (resulting in $\sim$ 699048 groups). Finally, assuming that the defined energy resolution has 200 groupings, the total merging candidate group now stands at $\sim 1.4 \times 10^8$ groups. Thus, the minimum number of simulated particles after merging is $\sim 2.8 \times 10^8$, if the following conditions are met:

- There is only one species of simulated particles.
- The particles' momentum orientation is isotropic.

- The particles' energy distribution is uniform in the range of the considered energy selection groups.

However, the specific simulation case of tokamak avalanche breakdown means that the orientation of charged particles momentum is approximately aligned with the background electric field. The minimum super-particle number is then greatly reduced. In addition, the particle's energy distribution in a electron-neutral collision dominant scenario is centred at low energy ranges. This means that the super-particle counts are further reduced as most of the energy groups will not have merging candidates in them. Regardless, it is important to note that a minimum limit of the simulated particle exists.

4.8 Conclusion

A new merging algorithm for meshless methods is proposed and its various aspects are studied in detail. The proposed merging algorithm is able to conserve mass, energy and momentum of the merging candidates in scenarios where particle scattering is absent. However, preservation of the merging candidates' energy distribution is not satisfactory when scattering and ionisation are involved. As such, this introduces a knock on effect where smaller deviations in electron energy distribution in earlier times are exaggerated as simulation continues. The approximation of the growth rate slowly worsens as a result (see Fig. 4.17).

It is clear at this point that the merging test in Sec. 4.6 is too limited in time. Further continuation of the simulation will be helpful in understanding the growth rate approximation and its dependence on $\Delta\Omega$ or the defined energy grouping resolution. It is also imperative to improve the treatment of super-particle collisions and scattering discussed in Sec. 4.5. The poor preservation of electron energy distribution with scattering/ionisation scenarios may point to the inadequacy of the super-particle collision models to accurately represent the scattering interactions. As the simulation is centred around persistent exponential growth of the charged particle medium in the early stage of plasma initiation, *a posteriori* correction of the energy distribution from merging could be possible if assumptions about the expected plasma parameters at the end of the avalanche breakdown process are made.

On a more positive note, results in Sec. 4.7 show that even the finest $\Delta\Omega$ (which results in the least effective particle number reduction) consumed only 51 % of the total compute resources for the benchmark simulation. This is a worthwhile endeavour that

could accelerate the simulation runs and extend the range of possible mesh-free tokamak plasma numerical studies.

Chapter 5

Townsend avalanche benchmark

5.1 Introduction

As discussed in Sec. 3.4, a Monte-Carlo collision model is chosen to simulate the discharge process. Several key components in discharge simulation such as the numerical representation of charged particles, determination of electron-neutral collision likelihoods, calculation of the self-consistent electric field arising from spatial distribution of charges and numerical integration of equation of motion follow conventional treatments described in Ch. 3. For the ionisation process, there are some aspects that require more scrutiny, namely the choice of the scatter angle model and the electron-H_2 cross-sections.

It is important to assess the impact of the scatter angle models on the α and the electron drift velocity V_e by comparing with existing experimental results before choosing one suitable for the tokamak scenario. This is rather crucial for a few reasons, first among them is the fact that two established models by Vahedi and Okhrimovskyy were derived for larger and heavier nonpolar neutral targets (Ar, CH_4 and N_2 etc.). This means that the resulting scatter angle distribution might be unsuitable for smaller and lighter molecules such as H_2 (whose Van der Waals radius is approximately 120 pm compared to Argon's 188 pm [81], and approximately 40 times lighter). Additionally, different scatter angle distribution introduced by each model will alter the mean collisional drag experienced by electrons. For example, a model that has a strong forward scattering bias will introduce less mean collisional drag than a purely isotropic model. The altered collisional drag can affect the obtained α and V_e. Lack of prior numerical experiments in electron-H_2 collision applications signifies the need to conduct such study before committing to the tokamak scenario.

The choice of cross section will naturally affect the effective α measured throughout the discharge simulation, because its magnitude dictates the likelihood of collision outcomes. Since the neutral target is a molecule, there exist a number of channels of metastable excitations and ionisation paths. Inclusion of all available electron-H_2 impact cross sections would be ideal to represent the collision processes best, but unnecessary here since the focus is on the current amplification from the discharge process. Therefore, one of the goals of this numerical benchmark is to ensure the chosen selection of cross sections sufficiently approximates the expected α from experimental records. This study also serves as a proof-of-concept of a complete discharge simulation with all charged particles (electrons and positive ions that arise from ionisation events) simulated and tracked in 3 dimensions in both space and momentum, in combination with a parallel tree code algorithm in the evaluation of the self-consistent electric field. Comparisons of the numerically obtained α with those from parallel plate experiments will help choose the most suitable scattering angle model to approximate the avalanche breakdown process in tokamak geometry.

Before getting into the details of the numerical study, this chapter will first discuss the prior experimental work forming the benchmark for the numerical setup to compare with. This is then followed by the description of the numerical configuration. The considered electron-H_2 collision cross sections in the numerical setup are explained afterwards. Finally, a comparison of the obtained α and V_e between the scatter angle models is made to determine the most suitable choice for the Townsend avalanche simulation in a tokamak setting. The results of this numerical study are published in Plasma Physics and Controlled Fusion [82].

5.2 Parallel plate experiment

As noted in Sec. 2.2 where Eq. 2.11 was derived, the ion confinement time scale in a tokamak during plasma initiation phase is at least two orders of magnitude longer than the electron confinement time. This allows us to assume that secondary electron emission due to ion-surface impact ionisation is negligible. In this case, the γ factor is treated as 0 in Eq. 2.10, repeated here for convenience

$$\frac{I}{I_0} = \frac{e^{\alpha d}}{1 - \gamma(e^{\alpha d} - 1)}.$$

Adopting this assumption severely limits the number of relevant prior experimental works that we can compare with. Majority of the parallel plate experiments measure the overall current between the electrode plates, which include contributions of both

α and γ. The respective contributions of α and γ are difficult to be distinguished. This difficulty arises naturally since parallel plate experiments are conducted with a limited distance between electrode plates (order of cm in length). Ions that came from electron-neutral impact ionisation will gain energy from the potential difference between electrodes, until eventual impact with the cathode causing further secondary ionisation. Thus, studies that purely measure α have to operate at a low range of potential differences in order to limit the ion energy gain below the secondary emission threshold.

It turns out that works by D. J. Rose [83] and Tagashira *et al.* [84] fit the above criteria perfectly, both obtaining experimentally measured α parameters in a range of E/p ratios. The significance of E/p arises from the fact that this parameter can be interpreted as the ratio of energy gain through electric field acceleration and loss via collisional drag, dictated by the collisional frequency as a function of the prefill gass pressure p. Recall that both α and V_e are also functions of this E/p parameter (See Eq. 2.12 and Eq. 2.22), repeated here for convenience

$$\alpha = Ap \exp\left(-\frac{Bp}{E}\right)$$
$$V_\mathrm{e} \sim \frac{ek_\mathrm{B}T}{m_\mathrm{e}\mathcal{C}}\frac{E}{p}.$$

Fig. 5.1 illustrates two parallel electrodes separated by a distance of d, connected to a variable voltage source that creates a potential difference between them. Free charges that lie between the plates are then accelerated by the resulting electric field E. In Rose's work, the electrodes are 5 cm in diameter and placed in a glass vacuum tube. The anode is perforated, allowing ultraviolet light to shine through and interact with a molybdenum cathode to produce free electrons via photoemission. One of the operating scenarios of the ITER tokamak startup is E/p value of approximately $300\,\mathrm{V\,m^{-1}\,Pa^{-1}}$, which happens to fall within the range of the experiment. A benchmark numerical simulation at the relevant range is certainly most helpful to determine the proper setting for the eventual tokamak simulation. Fortunately, Rose's work reports α values over a large range of E/p and the numerical results will be compared against it. The following sections will provide explanation on the choice of cross sections followed by the setup of the numerical experiment.

5.3 Electron-Hydrogen cross sections

The cross sections of electron-H_2 molecule collisions used in the plate experiment are based mainly on the reported values from J. S. Yoon *et al.* [4]. They are a compilation

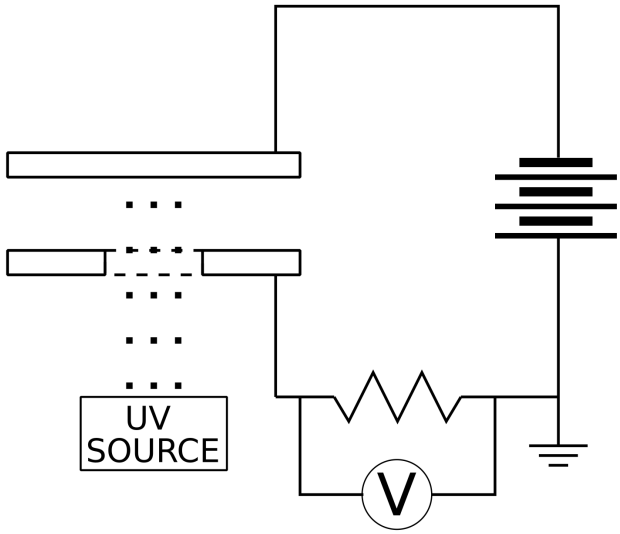

FIGURE 5.1: Townsend avalanche experiment setup.

of decades of experimental work and recommended cross sectional data for an electron energy ranging from 0.001 eV to 1000 eV as shown in Fig. 5.2. Aside from the case of elastic scattering, a portion of the incident electron's kinetic energy is spent ($\varepsilon_{\text{redux}}$) during the collision event as described by Eq. 3.17. For the current work, the following reactions and corresponding $\varepsilon_{\text{redux}}$ [85] are included for the simulated collision outcomes:

- $e + \text{H}_2 \rightarrow e + \text{H}_2$
  (elastic scattering)
- $e + \text{H}_2 \rightarrow e + \text{H}_2^*$
  (vibrational level transition, $\varepsilon_{\text{redux}} = 0.516\,\text{eV}$)
  (rotational level transition, $\varepsilon_{\text{redux}} = 44.1\,\text{meV}$)
- $e + \text{H}_2 \rightarrow 2e + \text{H}_2^+$
  (non-dissociative ionisation, $\varepsilon_{\text{redux}} = 15.426\,\text{eV}$)
- $e + \text{H}_2 \rightarrow 2e + \text{H} + \text{H}^+$
  (dissociative ionisation, $\varepsilon_{\text{redux}} = 18.075\,\text{eV}$)

The included collision cross sections are chosen to focus primarily on the ionisation of zero-point ground state of hydrogen molecules, where its rovibrational level v and J is both at 0. The cross sections for rovibrational level transition for $v = 0 \rightarrow 1$ and $J = 0 \rightarrow 2$ are also included, considering the sizeable cross sections in the lower energy range between 10^{-1} and $10^{1}\,\text{eV}$. It should be noted that the prefilled neutral gas

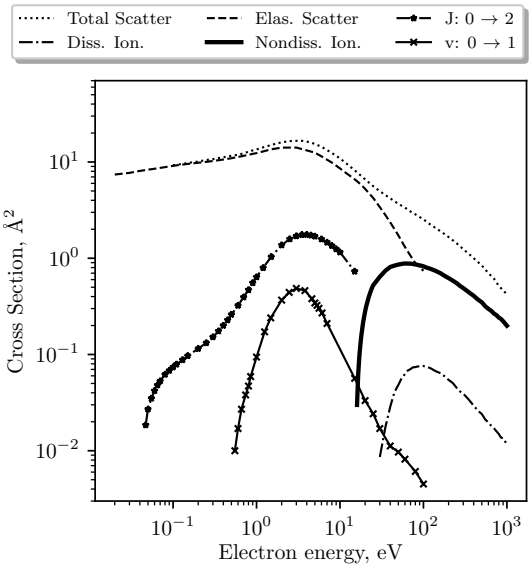

FIGURE 5.2: Cross section values of electron-H_2 molecule collision reaction types plotted over electron energy of 0.001 - 1000 eV [4].

molecules are not explicitly simulated in general, in an effort to save computational resources.

Note that the $e + H_2 \rightarrow e + H + H$ cross section is absent in this work. A deliberate choice is made not to include this, since its overall contribution to α via ionisation of hydrogen atoms is negligible due to its low number density compared to H_2 molecules. At the end of a typical simulation run, the estimated number density of H is at least 10^{11} times smaller than for H_2 at 273.15 K and 333.31 Pa. The hydrogen molecule number density is also assumed to be constant throughout the simulation. This assumption is made since the simulated currents reach an equilibrium at a time scale of $\mathcal{O}(1\,\mu s)$, thus it is assumed that the ionisation fraction is negligible.

The cross section for total scattering σ_T is included in Fig. 5.2, as it plays a role in the computation of electron - H_2 collision probabilities which is presented previously in Section 3.4.1. More specifically, the value of σ_T is used in the calculation of the null collision frequency.

5.4 Numerical experiment

In our model setup, the simulation domain is a cylinder geometry with a diameter of 7 cm and height (aligned in the z direction) equivalent to the plate separation d. The position of the cathode is assumed to be at $z = 0$, while the anode is simply a numerical offset d in the $-z$ direction, prescribed at the start of the simulation. A preset number of electrons to be "added" at $z = -0.01$ for every time step is used to emulate the photoemitted current from the cathode due to ultraviolet radiation. These electrons are only inserted in a circular area with diameter of 5 cm similar to the electrodes' dimension used by Rose [83]. Tagashira *et al.* [84] reported a photoemitted current at the order of 5×10^{-12} A, due to the nature of time discretisation in numerical simulations, it would mean that the number of photoemitted electrons per time step at a resolution of picoseconds is less than one. Instead, a series of convergence tests found that a prescribed 20 electrons per time step is sufficient to reach statistical stability for the obtained mean value of first Townsend coefficient α. Their x and y coordinates are resolved by a process of rejection sampling to ensure a uniform spatial distribution of electron source from the cathode.

Considering the fact that there will be at least four random numbers required for each simulated electron for every time step (two in the determination of the collision likelihood and its outcome, two in the calculation of the incident electron's post-collision velocity vector), a pseudo random number generator that has sufficiently long period and is highly parallelisable has to be chosen. As such, every instance of random number used in this work is generated through 'Random123', a counter-based random number generator [86]. For ease of comparison with Rose's work, the physical units used until the end of this chapter will be in Torr for pressure and cm for length.

Determination of the electrode separation d used in the simulation is derived from reported values of Rose's experimental work, with E/p value ranging between 15 and 1000 $\mathrm{V\,cm^{-1}\,Torr^{-1}}$ and pressure at the range of $0.5 < p < 10.5$ Torr. One set of reported parameters is $E/p = 156\,\mathrm{V\,cm^{-1}\,Torr^{-1}}$ with voltage across electrodes measured at 50 V and the pressure of 2.7 Torr. As such, the electrode separation d worked out to be approximately 0.12 cm. All simulations presented in this work are performed at a temperature of 0 °C which then determines the neutral number density. The electric field created by potential difference between separated electrodes is simulated by prescribing a constant $\mathbf{E}_{\mathrm{ext}}$ which all simulated charged particles will experience. In all the presented simulation cases, $\mathbf{E}_{\mathrm{ext}}$ is parallel to the $+z$ direction.

Each of the added electrons near the cathode is assumed to carry an initial energy

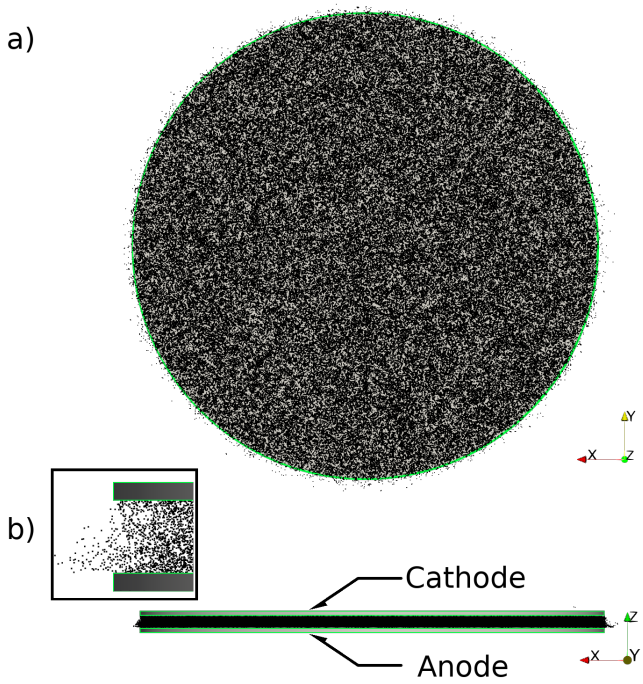

FIGURE 5.3: a) X-Y plane view of electrons, anode in background. Each individual electron is represented by a black dot. Note that the electrode edges are highlighted as a visual guide. They are only charge collection boundaries in simulations. b) X-Z plane view of electrodes and electron spatial distribution in a typical simulation run. Close up view of the electrode edge shown in the box.

of 1 eV, travelling in the $-$z direction. Any particle that crosses the boundary of z $= 0$ or z $= -d$ and within the 5 cm diameter area is removed from the simulation and subsequently counted for the calculation of the current amplification factor. The electrons that have moved laterally away from the 5 cm diameter area are removed but ignored for the current amplification factor counts. Fig. 5.3a shows the typical spatial distribution of the simulated electrons in the x-y plane during a simulation run. It is worth mentioning that H^+ and H_2^+ ions are not shown in this figure to avoid cluttering. Of interest in Fig. 5.3b are the electrons that are scattered away from the electrode regions (outside of the 5 cm diameter area) as they near the anode, which arises naturally from the electron-neutral elastic scattering and Coulomb scattering effects experienced by the electrons as they travel between the electrodes. These electrons will not be counted toward the measure of α value.

At every time step, the sum of all the charges carried by charged particles (electrons, H^+ and H_2^+) that cross the anode boundary is recorded as q_{an}. Fig. 5.4 shows the recorded sum of the charges (measured with the unit of $1e$) at the anode under E/p

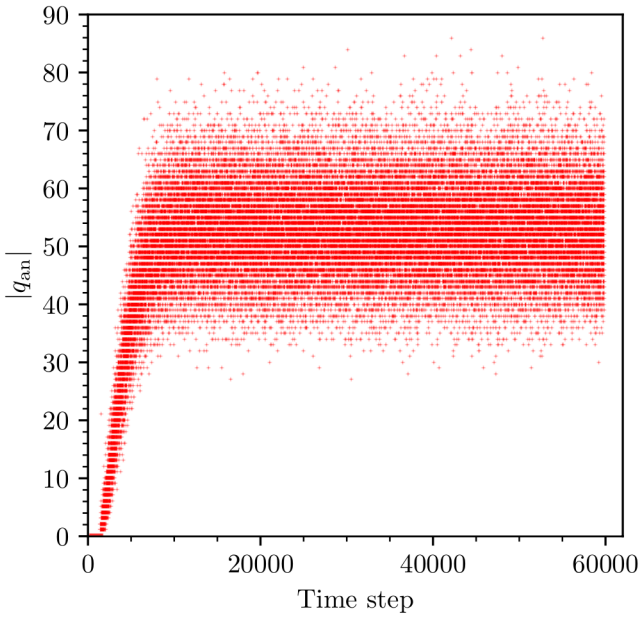

FIGURE 5.4: Recorded charge at the anode (with unit of 1 e) for each simulation time step, simulation performed at a total time step count of 60,000. Data shown for the $E/p = 400\,\mathrm{V\,cm^{-1}\,Torr^{-1}}$ case.

of $400\,\mathrm{V\,cm^{-1}\,Torr^{-1}}$, note that the recorded q_{an} is mostly from electrons. It can be observed that the recorded charge settles to a steady fluctuation about a constant mean value.

It was shown in Section 3.4.2 that the implemented scattering angle models allow backscattering. As such, rather than the expected 20 photoemitted electrons at every time step as described earlier, the measured net photoemitted electrons q_0 also fluctuate as shown in Fig. 5.5. The expression for q_0 at every time step is

$$q_0 = 20 - q_{\mathrm{b.s.}}, \tag{5.1}$$

where $q_{\mathrm{b.s.}}$ describes the number of back-scattered electrons recorded at the cathode. It should be noted that the spread of the recorded q_0 reduces as E/p increases. Higher E/p can be achieved by either increasing $\mathbf{E}_{\mathrm{ext}}$ or reducing gas pressure p. Having larger $\mathbf{E}_{\mathrm{ext}}$ will cause electrons to experience larger downward acceleration (away from the cathode at z = 0). As such, electrons are less likely to reach the cathode after back-scattering events. On the other hand, lowering the pressure p effectively reduces the collision frequency between electrons and neutrals, allowing electrons to move unobstructed over a

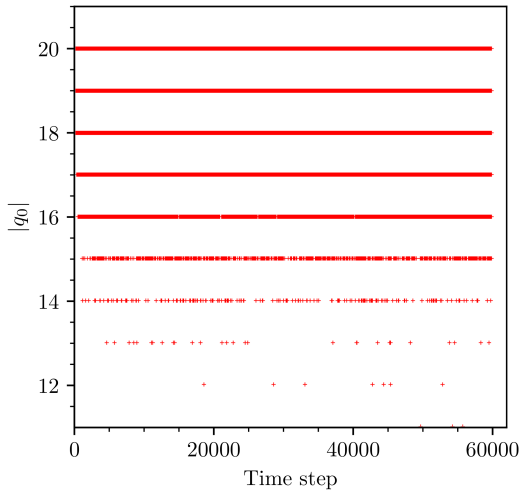

FIGURE 5.5: Net photoemitted electrons ($|q_0|$) at each simulation time step, simulation performed at a total time step count of 60,000. Data shown for the $E/p = 400\,\mathrm{V\,cm^{-1}\,Torr^{-1}}$ case.

longer distance.

The mean charges at the anode Q_{an} and the mean net photoemitted electrons Q_0 are computed (along with their standard deviations), followed by the first Townsend coefficient α obtained through

$$\alpha = \frac{1}{d}\ln(I/I_0) = \frac{1}{d}\ln(Q_{\mathrm{an}}/Q_0). \tag{5.2}$$

The uncertainty of α is then calculated through propagation of errors.

5.5 Results

The explicit representation of electrons enables a detailed study of their spatial distribution, as well as the influence of cross sections and scattering angle calculations on the energy at any chosen time step. Fig. 5.6 shows the electron number density and averaged energy over distance for $E/p = 400\,\mathrm{V\,cm^{-1}\,Torr^{-1}}$.

An interesting observation can be made regarding the high electron number density near the cathode, which diminishes rather abruptly over a short distance. This is explained by the lack of low energy electrons' mobility as they are initially introduced into the system. As they travel along the accelerating electric field, a spread in the energy

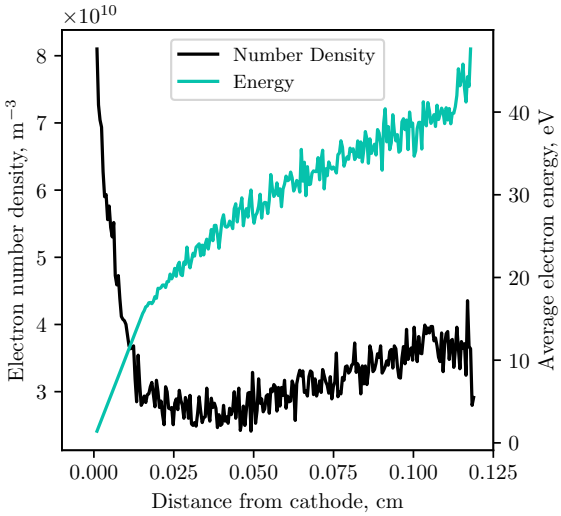

FIGURE 5.6: Electron number density and average energy over distance. Measurement is taken from $E/p = 400\,\mathrm{V\,cm^{-1}\,Torr^{-1}}$ case at the simulation time step of 60,000.

distribution occurs due to the probability of collisions with the neutral background (determined by collision frequency ν) and the distribution of the resulting scattering angle. This spread affects the spatial distribution of electrons since they do not move at the same velocity.

It is noted that the electron energy gain over distance is smooth up to approximately 15 eV, which can be attributed to the lack of major energy sink within that energy range. Referring to the cross section plot in Fig. 5.2, the only other reactions that can act as energy sink in the energy range below 15 eV are vibrational and rotational level transitions. However, their impact on electron energy is small as the rotational level transition $\Delta\varepsilon$ is 44.1 meV and the cross section for vibrational level transition is 1 order of magnitude smaller than elastic scattering at best.

Once the electron's energy threshold goes above the requirement for ionisation, additional cross sections are considered during collision events. The number density and the average electron energy continue to rise as the travel distance increases. There is a small but noticeable drop in number density beginning from a distance of approximately 0.11 cm as well as a rise in average electron energy. This can be attributed to slightly diminishing cross sections above 40 eV, meaning that the electrons encounter fewer collisions thus more likely to move unimpeded.

5.5.1 Influence of Δt on obtained α

Recall that the choice of time step size has an upper bound given in Eq. 3.14. This implies that a pre-filled pressure of 2.5 Torr (0.33 kPa) would require a maximum time step size of $\mathcal{O}(1\,\text{ps})$ in order to keep the probability of more than one collision per time step per particle below 1%. The influence of electric field strength on time step size is also considered. However, the corresponding limit is much larger than the suggested picosecond scale.

In order to choose the proper time step size for the simulation, a set of tests is done with the initial choice of 1 ps, 0.4 ps, 0.25 ps and finally 0.1 ps. The convergence tests are done at $E/p = 400\,\text{V cm}^{-1}\,\text{Torr}^{-1}$ with pressure of 2.5 Torr, using the presented random scatter model. A comparison of the obtained α/p for each of the chosen time step sizes is made and the result is tabulated in Table 5.1.

TABLE 5.1: Mean α/p values for $E/p = 400\,\text{V cm}^{-1}\,\text{Torr}^{-1}$

Time Step Size [ps]	Mean α/p [$\text{cm}^{-1}\,\text{Torr}^{-1}$]
1.0	3.46 ± 0.51
0.4	3.53 ± 0.51
0.25	3.56 ± 0.51
0.1	3.57 ± 0.52

The tabulated results show that the obtained mean values are within 1 standard deviation of each other. This suggested that the choices of time step sizes are all acceptable. However, the variation of obtained mean α/p values as the step sizes get smaller do show a trend of convergence. In light of that, the lower time step size choices of 0.25 ps and 0.1 ps are preferred. For the following simulation cases, 0.25 ps is chosen to help reduce the total time required to complete the simulations.

5.5.2 Influence of E/p on obtained α

Rose performed the experiment with various combinations of electric field strengths E and pre-filled gas pressures p. In order to compare with those results, appropriate values for electric field strength and pressure are chosen for the numerical simulations. Specifically, the chosen E/p are 60, 100, 200, 400 and $600\,\text{V cm}^{-1}\,\text{Torr}^{-1}$. All the cases were benchmarked at a plate separation of $d = 0.12\,\text{cm}$.

Note that the simulation severely underestimates the mean α/p at the E/p ratio of $60\,\text{V cm}^{-1}\,\text{Torr}^{-1}$ for all three implemented scattering angle models. However, good

TABLE 5.2: Comparison of obtained mean α/p values. The columns labeled with 'Rose', 'Random', 'Vahedi', and 'Okhrimovskyy' denote values obtained from D. J. Rose's experiment, numerical experiments using Random Scatter model, Vahedi model and Okhrimovskyy model to describe scattering angle distribution respectively.

	Mean α/p [$\mathrm{cm^{-1}\,Torr^{-1}}$]			
E/p	Rose	Random	Vahedi	Okhrimovskyy
60	0.50	0.10 ± 1.19	0.09 ± 1.06	0.08 ± 1.30
100	1.26	1.24 ± 0.89	1.07 ± 0.82	0.97 ± 0.97
200	2.55	2.57 ± 0.62	2.18 ± 0.59	2.00 ± 0.67
400	3.60	3.56 ± 0.51	2.94 ± 0.52	2.71 ± 0.57
600	4.10	3.85 ± 0.40	3.14 ± 0.44	2.95 ± 0.47

agreement with Rose's reported α/p is observed in the range of 100 to 400 $\mathrm{V\,cm^{-1}\,Torr^{-1}}$ for the newly proposed random scatter model, while the models by Vahedi and Okhrimovskyy result in lower mean α/p values. Another interesting observation is that the uncertainty of α/p reduces as E/p increases. This is due to diminishing value of $q_{\mathrm{b.s.}}$ in Eq. 5.1, thus giving a narrower spread of q_0 as E/p increases. Similar trend of reduction in the uncertainty of recorded q_{an} is observed as well. The obtained mean α/p are also noticeably lower compared to Rose's reported value at E/p of 600 $\mathrm{V\,cm^{-1}\,Torr^{-1}}$, this could be attributed to the neglected hydrogen dissociations that produce hydrogen atoms, which in turn provide another channel for additional impact ionisation.

One could attempt to explain the underestimation of α/p by both Vahedi and Okhrimovskyy's model via the anisotropic scattering angle distribution in Fig. 3.5 and Fig. 3.7 respectively. In the event of ionisation, random scatter model enforces a forward scatter of the incident electrons, which is markedly different from the other two models. Should the ionisation event occur for an incident electron that is just above the ionisation energy threshold, there is a non-negligible probability that the incident electron will backscatter after the energy is spent to ionise an H_2 molecule. For example, Vahedi's model would have equal chance for forward and backward scatter for electrons that have approximately 0.01 eV while Okhrimovskyy's model actually favours backward scatter for electrons below 1 eV. This causes a markedly higher drag experienced by low energy incident electron that is fresh from ionisation events compared to the random scatter model, leading to longer time intervals when electrons reach the energy threshold required for further ionisation (thus, the diminished α/p value). This suggests that Vahedi's and Okhrimovskyy's models require different methods to account for energy partitions during ionisation events, other than the classical treatment of energy and momentum conservation presented at Eq. 3.18.

In the current work, the mean electron drift velocity $\mathrm{V_{DE}}$ is obtained by taking the last

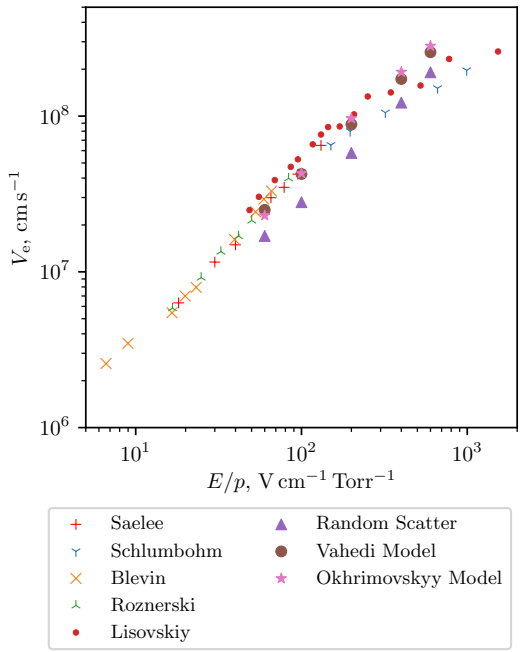

FIGURE 5.7: Comparison of our results for the mean electron drift velocity using all three models to reported values from: Simulation data obtained from Saelee *et al.* [5], derived data from Schlumbohm [6] and Lisovskiy *et al.* [7], measured data from Blevin *et al.* [8], and Roznerski *et al.* [9].

simulated time step of the electron population, followed by averaging all the electrons' velocities. Fig. 5.7 shows the comparison of measured V_{DE} from presented scattering angle models and the various prior works [5–9]. It can be observed that the models for calculating the scattering angle by Vahedi and Okhrimovskyy give good agreement to other previously reported results. Note that the measured drift velocity using Okhrimovskyy's model gives a slightly lower mean result when compared to Vahedi's model at $E/p = 60\,\mathrm{V\,cm^{-1}\,Torr^{-1}}$ whereas it exhibits a higher value above $100\,\mathrm{V\,cm^{-1}\,Torr^{-1}}$, while the random scatter model gives an overall lower estimation. It might seem to be a direct contradiction to the arguments made in the diminished α/p value for Vahedi and Okhrimovskyy's model, as one could come to the belief that higher V_e should correspond to higher α. Reality is less straightforward, since the majority of the electron population is below the ionisation energy threshold. This can be seen in the case of $400\,\mathrm{V\,cm^{-1}\,Torr^{-1}}$, as Okhrimovskyy's model (which gives the highest recorded V_e among the three models) reports a mean drift velocity of $1.92 \times 10^8\,\mathrm{cm\,s^{-1}}$, which corresponds to approximately 10.5 eV. This can also be observed from Fig. 5.6 where the low energy electrons dominate the simulated population. The resulting V_e is mostly affected

by the scattering angle distribution at energy range below the ionisation threshold. Since the random scatter model assumes isotropic angle distribution for non-ionising case, V_e in such model is naturally lower than Vahedi's model (which is consistently forward scatter biased for electrons above 0.01 eV). Comparison between Vahedi and Okhrimovskyy's model also shows noticeable correspondence of the resulting V_e with the angle distribution of respective models at low eV values. More specifically, Okhrimovskyy's model reports lower V_e at lower E/p range and overtakes the reported values at higher range. This is a result of the extremes in angle distribution seen in Fig. 3.7

Even though the random scatter model underestimates reported values of previous works at $E/p \leq 200\,\mathrm{V\,cm^{-1}\,Torr^{-1}}$, it is seen that the agreement improves at 400 and $600\,\mathrm{V\,cm^{-1}\,Torr^{-1}}$. The comparison between the three presented models shows that both energy dependent scattering angle calculations give a better approximation of $\mathrm{V_{DE}}$.

5.5.3 Discussion

In the simulations, electrodes are only defined as boundaries where charge collection occurs. Intricate interaction between charged particles and electrodes taking place in actual experiments, such as charged particle sheath formation in close proximity to electrodes or secondary electron creation through ion collision on cathodes, are not captured. With that in mind, the current study chooses to benchmark the proposed model with experimental work focusing on measuring the first Townsend coefficient α. As such, the presented set of benchmark simulations are performed with the shortest separation distance d derived from Rose's work as well as using the lower ranges of operating pressure.

A number of modifications to the numerical setup are required to extend the pressure and electric field range of validity for α measurements in electrode plate experiments. Chief among them is the modelling of the electric field via potential difference over a defined separation distance rather than a prescribed constant $\mathbf{E}_{\mathrm{ext}}$. Electric potential changes across the electrodes at longer separation distances would then be modelled correctly.

However, the current model is suitable in the simulation of tokamak ohmic breakdown since the electric field experienced by charged particles is induced by the current ramp up in the central solenoid rather than the potential difference between electrodes. Establishing a method to predict the rise of electron population via electron-neutral collisions, as demonstrated in this work, is one of the components required to capture the

very early phases of tokamak plasma initiation where the electron number density is well below $10^3\,\mathrm{m}^{-3}$. Since the obtained α presented in this work has good agreement with reported values in high E/p ranges, it fits the ohmic breakdown phase of tokamak devices such as NSTX at $E/p \approx 500\,\mathrm{V\,cm^{-1}\,Torr^{-1}}$ [17] or ITER at a predicted $E/p \approx 400\,\mathrm{V\,cm^{-1}\,Torr^{-1}}$ [18].

On a separate note, Townsend's work [39] reported different values of current amplification with experiments at the same E/p ratio with differing operating pressure. This trend is noted in the simulation as well, but not explicitly reported in studies conducted by different authors [87]. More work could be done to study the effect on obtained α at different pressure settings while maintaining a constant E/p ratio as well as constant electrode separation d.

This study showed that the choice of implemented scattering angle model plays a major role in the simulated Townsend discharge in a full 3D application. In light of the eventual simulation of an ITER-like tokamak breakdown, a conscious choice is made to implement the random scatter model to simulate the electron-H_2 ionisation events as it provides the best approximation of α value among the considered models as well as acceptable accuracy of V_e.

5.6 Conclusion

A 3D first principles simulation of Townsend discharge is presented and benchmarked against prior experimental work. The study shows that the choice of implemented scattering angle model plays a major role in the simulated Townsend discharge in a full 3D application. It is found that the proposed random scatter model produces good agreement in obtained α/p values when compared to Rose's reported values. However, the random scatter model produced mean electron drift velocities that are lower than reported values from other works for $E/p < 400\,\mathrm{V\,cm^{-1}\,Torr^{-1}}$. Both Vahedi *et al.* and Okhrimovskyy *et al.* scattering model produced α/p that is lower than the results presented in Rose's work, while producing good approximations of the resulting mean electron drift velocities. In order to improve the approximation in both α/p and $\mathrm{V_{DE}}$ further, a combination of forward scatter restriction presented in Section 3.4.2.1 during ionisation events, with Eq. 3.19 or Eq. 3.21 in other scenarios could be studied further.

It should be reiterated that the recorded current amplifications are for situations where the primary means of ionisation is through electron-neutral collisions. The implemented

ionisation model is then suitable for tokamak breakdown scenario where secondary ionisation sources are absent near the magnetic null (breakdown region). A decision was made to adopt the random scatter model in modelling the ionisation fraction growth rate during the plasma initiation phase of tokamak ohmic breakdown. The E/p for the following tokamak simulations is approximately $400\,\mathrm{V\,cm^{-1}\,Torr^{-1}}$. Among the three considered scattering models, the random scatter model is found to approximate both α/p and V_e the best in the given E/p.

Chapter 6

ITER-like breakdown scenario

The previous chapters (specifically Ch. 3 and Ch. 5) laid the foundation for a large scale simulation of the plasma initiation process in a tokamak geometry. The discussed 0D ionisation fraction model (reproduced in Sec. 6.1) does not consider the geometry of the volume that the charged particles inhabit. The main goal of this study is to provide a first-principles 3D simulation of the Townsend avalanche process in ITER-like tokamak scenario. In this chapter, we introduce a benchmark simulation to produce an initial picture of 3D breakdown dynamics with the new model. The obtained results are compared to the 0D model to further understand the differences between theory and simulation. Parts of the results presented in this chapter were reported in the 47th EPS Conference on Plasma Physics [88]. Before proceeding with the content of the chapter, a clarification of terminologies is made here to avoid confusion. Any mention of external or background fields refers to induced fields created via the tokamak's superconducting magnets and current ramp up in the central solenoid. In contrast, internal or self-consistent fields denote those that arise from space charge distribution and currents from charged particle motions.

6.1 0D ionisation fraction equation

The 0D model is first described in Sec. 2.5, where the interpretation of the equation as well as the variable definition is given. Additional detailed consideration is provided here. For the sake of convenience, Eq. 2.19 is repeated here

$$\frac{1}{f_\mathrm{i}}\frac{\mathrm{d}f_\mathrm{i}}{\mathrm{d}t} = \frac{1}{n_\mathrm{e}}\frac{\mathrm{d}n_\mathrm{e}}{\mathrm{d}t} = \alpha V_\mathrm{e} - \frac{V_\mathrm{e}}{L}.$$

The right hand side of the equation is equivalent to the exponential coefficient of the analytical solution of either $f_{\mathrm{i}}(t)$ or $n_{\mathrm{e}}(t)$,

$$f_{\mathrm{i}}(t) = f_{\mathrm{i},0} \exp\left(\alpha V_{\mathrm{e}} - \frac{V_{\mathrm{e}}}{L}\right) t.$$

As such, a variable is introduced as the growth constant, representing the exponential coefficient with

$$\gamma_{0\mathrm{D}} = \alpha V_{\mathrm{e}} - \frac{V_{\mathrm{e}}}{L}. \tag{6.1}$$

During the operation of the ITER tokamak, the wall temperature of the vacuum vessel will initially be baked at 100 °C. Eq. 2.22 is then found to be

$$V_{\mathrm{e}} \sim 5730 \frac{E}{p}. \tag{6.2}$$

Furthermore, it is assumed that the vacuum vessel is filled with hydrogen molecules and the corresponding α parameter is determined via Eq. 2.12. Next, ITER's first plasma operation will have $E/p \approx 300\,\mathrm{V\,m^{-1}\,Pa^{-1}}$ and this parameter is sufficient to describe the ionisation fraction growth rate. Finally, it is usually assumed that the charged particles will have a connection length L of approximately 1 km in such a model. Clearly, the variables in Eq. 2.19 completely neglect both the spatial dimensionality that the charged particles inhabit and their velocity distribution, thus the 0D naming of the model. With the stated parameters, the ionisation fraction over time is plotted in Fig. 6.1.

Early on in the plasma initiation process (before 4 ms), the electric field E experienced by charges is dominated by the imposed external fields due to low ionisation fraction f_i. However, as the number density of charged particles (as well as the current density j) rises, E drops due to mutual-inductance of rising plasma current and the surrounding magnetic components [18]. To account for this, a correction factor to E given by

$$E = E_{\mathrm{loop}} \left(1 + \frac{L_{\mathrm{tor}}}{R} \frac{1}{I} \frac{\mathrm{d}I}{\mathrm{d}t}\right)^{-1}, \tag{6.3}$$

can be introduced, where E_{loop} refers to the electric field strength of external field, L_{tor} denotes the inductance of the torus, R represents the total resistance experienced by charged particles and I the corresponding plasma current. Substituting Eq. 6.3 into Eq. 6.2 then causes the observed tapering of the f_i in Fig. 6.1.

The focus of this study is up to ~ 1 ms time scale, allowing a study of ionisation fraction in time comparing to Eq. 2.19 in a simplified 3D model which neglects the aforementioned inductance influence (partly due to lack of information in the actual electrical

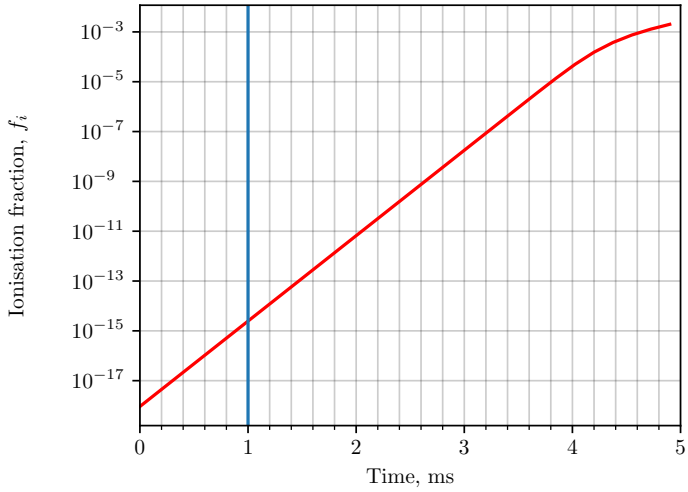

FIGURE 6.1: Ionisation fraction in time, calculated from Eq. 2.19 with $E/p \approx 300\,\mathrm{V\,m^{-1}\,Pa^{-1}}$. Blue vertical line refers to the time scale of this study.

current profile of ITER's superconducting magnets during operation). This restricted timescale nevertheless provides insight into several key properties, such as the resulting mean electron drift velocity V_e distribution, the space charge and current distributions, and lastly their corresponding self-consistent electric and magnetic field structures respectively.

6.2 Numerical setup of the benchmark case

The simulation domain throughout this numerical study is a simplified torus as shown in Fig. 6.2. Following consultation with collaborators at ITER's plasma operations and control division, a benchmark numerical setup for a breakdown scenario was proposed with parameters given in Tab. 6.1, representing a simplified version of the first plasma scenario for the upcoming ITER tokamak. An assumption is made here that there are preexisting free electrons present within the torus at the start of the simulation. Since the regime of tokamak operation considered here is the very initial phase of Townsend avalanche breakdown, a low number density of initial electrons at $10\,\mathrm{m^{-3}}$ is seeded within the blue torus. Considering that there could be continuous source of free electrons within the tokamak device in reality (possibly from muon decay, since muon flux is estimated to be $1\,\mathrm{cm^{-2}\,min^{-1}}$ at sea level [89]), only having an initial free electron population at the start of the simulation will serve as a lower bound of the required free charges population for plasma initiation if successfully demonstrated.

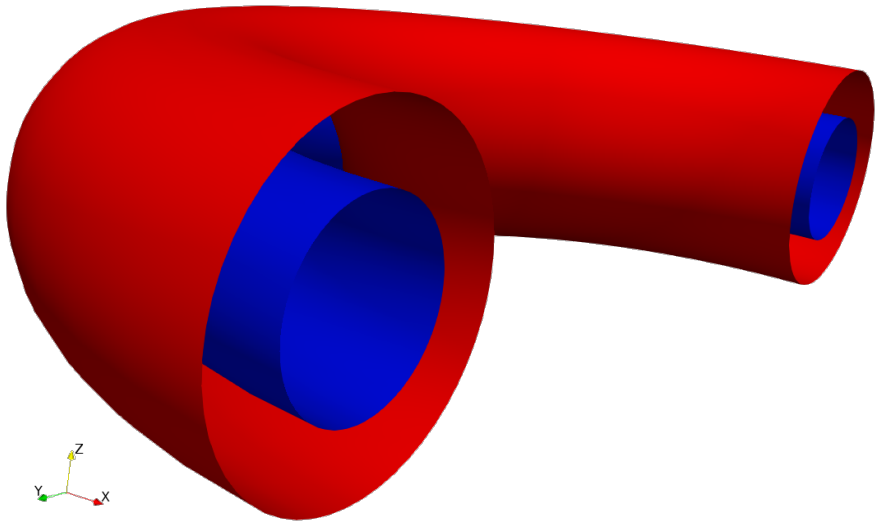

FIGURE 6.2: Bisected view of the torus domain used in the numerical simulation. Torus with red surface denotes the simulation domain, the blue surface denotes the boundary where initial electrons are seeded.

TABLE 6.1: ITER-like tokamak parameters and operating condition.

H_2 Pressure (Pa)	0.002
Wall temperature (K)	373.15
Initial electron number density (m^{-3})	10
Major radius (m)	5.8
Minor radius of electron seeding (m)	1.0
Minor radius of simulated domain (m)	1.75

6.2.1 Field configurations

The configuration of the external electric and magnetic fields is discussed in this section. The numerical implementation for these fields has already been discussed in detail in Sec. 3.5. Specifically, the toroidal magnetic field is expressed with Eq. 3.35. In order to yield 2.6 T at major radius $\rho = 5.8$ m, the value of $I = 75.24$ MA is used. Since $\mathbf{B}_\phi$ is an inverse ρ function, there is a field strength gradient anti-parallel to the radial direction as seen in Fig. 6.3. The toroidal magnetic field vector is aligned in the clockwise direction when viewed from the top. Correspondingly, the vector points out from the image in Fig. 6.3.

The poloidal magnetic field B_θ is then a combination of magnetic fields created via predefined currents running through 4 field coils. The derived expression for such field

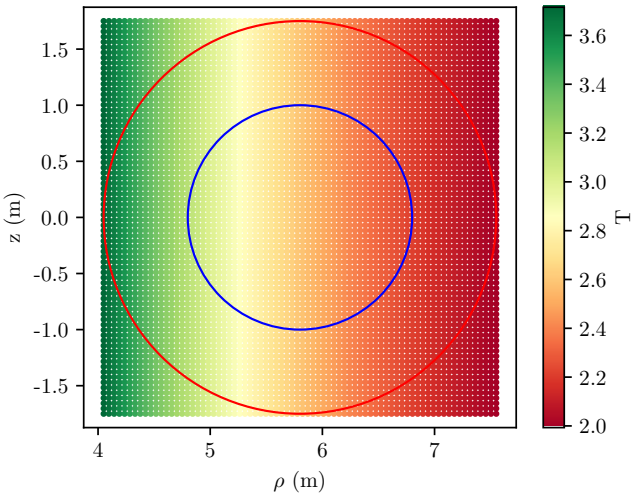

FIGURE 6.3: Toroidal magnetic field strength in the poloidal plane. $B_\phi = 2.6\,\mathrm{T}$ at $\rho = 5.8\,\mathrm{m}$.

TABLE 6.2: Coil positions/dimensions and the corresponding current for quadrupole poloidal magnetic field configuration

Coil no.	z' (m)	R (m)	I (A)
1	3.0	5.8	2357.366
2	-3.0	5.8	2357.366
3	0.0	3.0	100 000.0
4	0.0	8.3	15 230.96

definition is detailed in Sec. 3.5.2, only the parameters are reported in Tab. 6.2 for the sake of brevity. One important point is mentioned here, Eq. 3.34 assumes that the coil is located at $z = 0$. Therefore, the poloidal magnetic field experienced by charged particles is determined simply by particle's vertical coordinate z. The coil positions in this benchmark simulation are not strictly at $z = 0$, a new variable z' is defined to denote the vertical offset of the poloidal coil. Thus, the variable z in Eq. 3.34 is then

$$z = z_p - z', \tag{6.4}$$

where z_p refers to the particle's vertical coordinate. The resulting poloidal magnetic field due to the 4 poloidal field coils is shown in Fig. 6.4. This creates a single null point at $\rho = 5.8\,\mathrm{m}$ and $z = 0.0\,\mathrm{m}$ with the strength of $\sim 3.5 \times 10^{-5}\,\mathrm{T}$. The averaged poloidal magnetic field strength at the red boundary is $B_{\theta,\mathrm{edge}} = 3.613\,\mathrm{mT}$.

Finally, the electric field strength is computed with Eq. 3.36 which is very similar to the toroidal magnetic field equation. $V_{\mathrm{loop}} = 22\,\mathrm{V}$ is chosen such that the toroidal electric

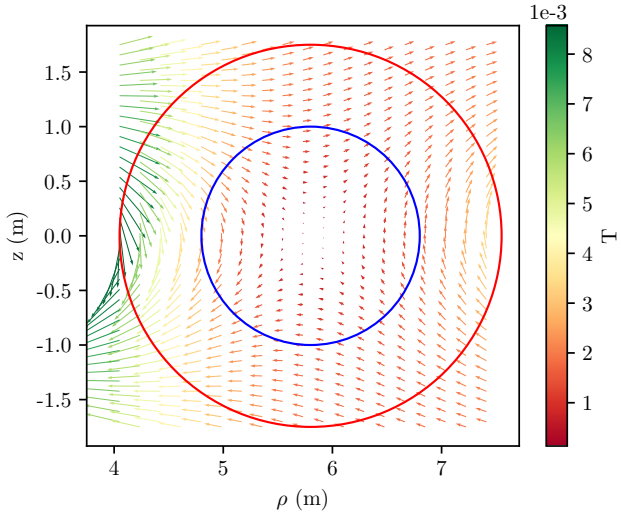

FIGURE 6.4: $\mathbf{B}_\theta$ in the poloidal plane.

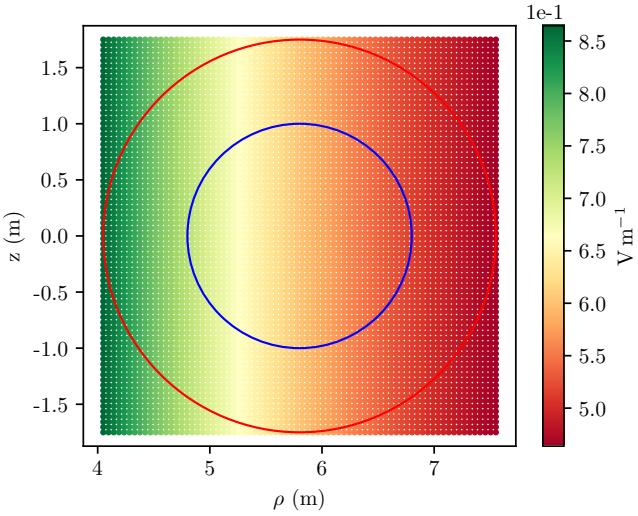

FIGURE 6.5: Toroidal electric field strength in the poloidal plane, $\mathbf{E}_\phi$ is pointing out of the figure.

field strength $E_\phi = 0.6\,\mathrm{V\,m^{-1}}$ at $\rho = 5.8\,\mathrm{m}$. The E_ϕ distribution in poloidal plane is shown in Fig. 6.5 and the field is parallel to $\mathbf{B}_\phi$. The combination of the stated pressure and E_ϕ gives $250 < E/p < 425\,\mathrm{V\,m^{-1}\,Pa^{-1}}$.

The electric and magnetic fields involved in this benchmark simulation run are now fully described. The accompanying numerical details are explained in the following section.

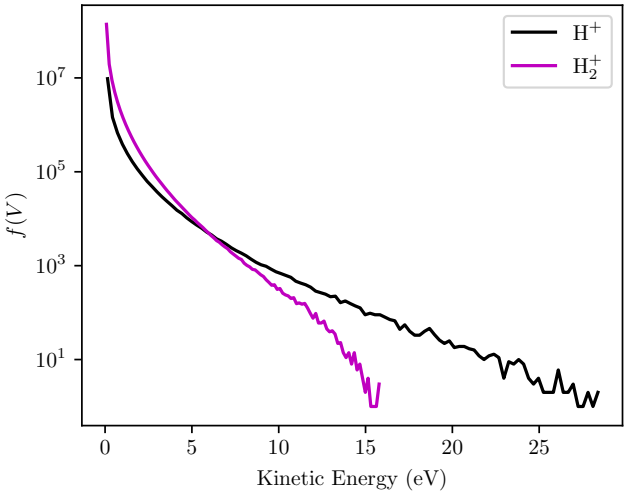

FIGURE 6.6: Ion kinetic energy distribution at the time of 1.1375 ms.

6.2.2 Electron - H_2 impact cross sections

Since the simulation now involves a toroidal magnetic field geometry, confinement properties experienced by charged particles are now vastly different from the plate experiment scenario discussed in Ch. 5. Specifically, the charged particles are now subjected to the background magnetic fields within the torus with the field line length scale upwards of kilometres, as opposed to centimetres in the plate experiment setting. This alone extends the lifetime of charged particles within the system significantly. The longer confinement time enables the existence of highly energetic particles and additional cross sections that can alter the energy distribution of charged particles should be considered.

An additional caveat here is that the ionisation in this study is purely from electron-H_2 collisions. It is true for this study (as seen in Fig. 6.6) since it is found *a posteriori* that H^+ and H_2^+ ions' kinetic energy peaks around 29 eV and 16 eV respectively at ∼1.14 ms. The energies are well below the ionisation threshold for ion-H_2 impact ionisations [90]. Regarding the collision cross sections of electron-H_2, the main reference of the cross section values is the data from Yoon *et al.*. While there are other more extensive databases (such as EIRENE's hydhel [91] and NIST's Binary-Encounter-Bethe (BEB) model [92]), a conscious choice was made to follow Yoon's data as it is the most recent and a result of compilation/comparisons of prior experimental measurements. In the instances where a cross section has limited range of electron's energy, it is then supplemented by EIRENE's fitted data. This is the case for the neutral dissociation of hydrogen molecules.

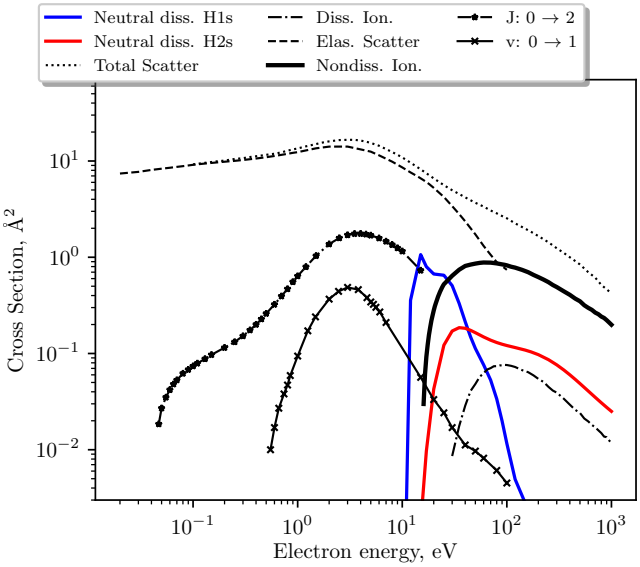

FIGURE 6.7: Black lines are cross sections from Yoon *et al.* published data. Coloured lines are from EIRENE's hydhel data fittings.

- $e + H_2 \rightarrow e + 2H(1s)$
- $e + H_2 \rightarrow e + H(1s) + H(2s)$

Dissociative attachment cross-sections are ignored in this study, due to the cross section values being at least 3 orders of magnitude smaller than the elastic scattering cross-section. Thus, it is highly unlikely for such responses to occur. Assuming that the initial electron population is at 1000 in a toroidal volume of 115 m^3, Eq. 2.19 predicts that electron number density $n_e \approx 5 \times 10^4\,m^{-3}$ at 1.1 ms. This translates to attachment frequency in the order of $\sim 10^{-14}$ Hz, making it negligible for consideration. The emission cross section in Yoon's work is also ignored because the cross section values are 3 orders of magnitude smaller than elastic scattering. Finally, the excitation cross sections are neglected as the hydrogen molecules are not explicitly simulated, so it is assumed that all molecules are at the ground state. Finally, the included cross sections in this study are plotted in Fig. 6.7.

There is one other consideration that is specific to the tokamak scenario. Since the connection length is in the order of kilometres, electrons will have the possibility to gain energy above the 1 keV threshold. Should the cross sections presented in Fig. 6.7 be applied to the simulation, there is then a rise in the population of highly energetic electrons above 1 keV (seen in Fig. 6.8) due to such electrons having a free unobstructed continuous

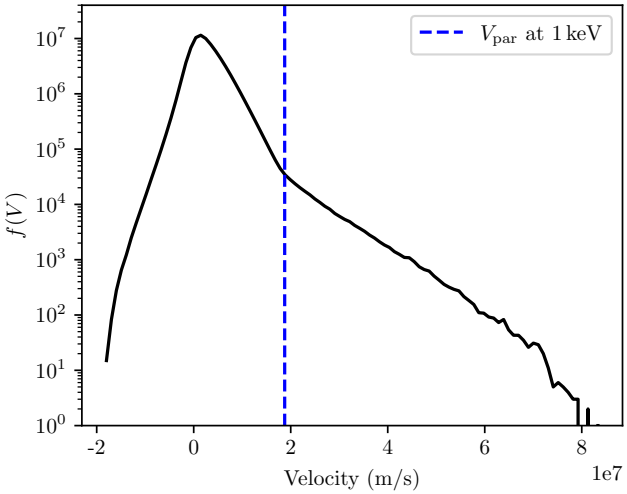

FIGURE 6.8: Electron parallel velocity V_{par} distribution at time of ∼1.14 ms. The distribution is a result of cross section values set to 0 for energetic electrons with energies above 1 keV.

TABLE 6.3: Gradient m_g for each considered cross section.

Cross section	m_g
Dissociative ionisation	-0.994
Nondissociative ionisation	-0.753
Elastic scattering	-1.311
J: $0 \rightarrow 2$	-1.073
v: $0 \rightarrow 1$	-1.281
Total scattering	-0.941

acceleration. The negative velocity sign is assigned to electrons that are moving against the direction of acceleration arising from the time independent background electric field.

Rather than introducing a zero cross section value directly for electrons with energies above available data range, an assumption is made such that the cross sections diminish exponentially as energy increases. In order to make such extrapolations, numerical fit of a linear function to the logscale of both cross section and energy from existing data points is done. The key parameter from this fitting is the gradient m_g for each cross section, from which the extrapolation from the last known data values can be done easily. The result of the fitting is tabulated in Tab. 6.3. It is worth mentioning that the data from EIRENE doesn't require such treatment, other than making sure that the electrons' energies are within the valid range of the fit given in the database.

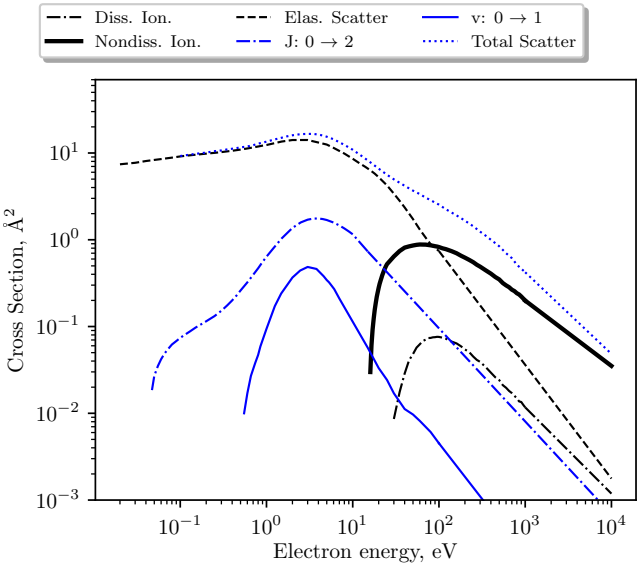

FIGURE 6.9: The extended cross sections.

The extrapolation of cross section σ to arbitrary electron energy $\varepsilon_{\text{kin.}}$ larger than the last known data point $\varepsilon_{\text{last}}$ is then calculated with

$$\log_{10}\sigma(\varepsilon_{\text{kin.}}) = m_{\text{g}}\left(\log_{10}\left(\frac{\varepsilon_{\text{kin.}}\sigma_{\text{last}}}{\varepsilon_{\text{last}}}\right)\right), \tag{6.5}$$

where σ_{last} denoting the cross section value of the last known data point. One can refer to the appendix to obtain $\varepsilon_{\text{last}}$ and σ_{last} for each cross section. The extended cross sections are plotted in Fig. 6.9.

6.2.3 Time step restriction

The next numerical consideration is the choice of time step size. In this specific case, there are several competing factors to be considered. Chief among them is the collision frequency between electrons and neutral particles. Assuming that the neutral gas pressure and temperature remain constant in time, the collision frequency then depends on the energy of the electron (collision cross section solely depended on the electron energy). In order to provide an estimate of the minimum time scale between collisions, an electron with energy which corresponds to the maximum total scattering cross section with background H_2 is used as an example. Referring to Eq. 3.14, the resulting time between collisions would be in the order of 1.451 µs assuming the electron carries energy of 3.25 eV (peak total scattering cross section value of $16.6 \times 10^{-20}\,\text{m}^{-2}$) with the listed

parameters in Tab. 6.1. As such, a time step size in the order of µs is sufficient to ensure that not more than one collision has occurred for an electron per step on average.

Next, the time step sizing is also dependent on the gyrofrequency of the electron subjected to the background magnetic field. Should one attempt to capture at least 3 points of the gyromotion in one period, the time step size is then limited to

$$\Delta t \leq \frac{3m_{\mathrm{e}}}{|q|\|\mathbf{B}\|}, \tag{6.6}$$

where m_{e} refers to the electron rest mass, q denoting the electron charge and $\mathbf{B}$ the magnetic field experienced by said electron. A further simplification is made such that $\|\mathbf{B}\|$ is purely a function of the toroidal magnetic field strength. This is justified by the magnitude of the poloidal field strength relative to the toroidal component. Referring to Fig. 6.3, it is clear that the time step size is in the order of picoseconds. Thus, this provides an upper bound to the chosen Δt for the simulation.

Due to the picosecond scale of the time step size, reaching the end time of ∼1 ms would require number of time steps in the order of 10^9 and above. Resolving the self-consistent electric field among the charged particles at every time step would be too expensive computationally. As such, a less frequent calculation of the internal fields is performed. The time between such computations is initially bound to the plasma frequency of the system. Consider an electron number density of $10^5\,\mathrm{m}^{-3}$ once again and assuming majority of the electrons are stationary, the resulting plasma frequency would be at 2839.30 Hz via

$$f_{\mathrm{plasma}} = \frac{1}{2\pi}\sqrt{\frac{n_{\mathrm{e}}q^2}{m_{\mathrm{e}}\varepsilon_0}}. \tag{6.7}$$

Even if the electron number density increases to $10^7\,\mathrm{m}^{-3}$, this results in a frequency of ∼30 kHz. This then corresponds to a step size upper limit of ∼33 µs between each computation for the self-consistent electric field. Even though this step size provides relief to the overall computational cost of the simulation, another careful consideration is made here. Assuming an electron with energy of 10 eV travelling in the toroidal direction, it would have travelled 624 m in the span of 33 µs (or have made ∼17 revolutions in a torus with a major radius of 5.8 m). The significance of 10 eV is suggested by Papoular as the energy barrier that electrons cannot overcome in an electron-neutral collision dominated setting [40]. As such, a specific choice of computing the internal fields at an interval of ∼ 2 µs is made, so that the updates are done at least once every revolution for the fast moving electrons. In the case of a scenario with $10^{17}\,\mathrm{m}^{-3}$, the plasma frequency assuming stationary electrons is then ∼3 GHz. Even so, the gyrofrequency of electrons is still higher. As such, saving computational costs by not computing the internal electric

fields at every step is possible. One should also come to the realisation that the charged particle medium is far from the familiar plasma medium after the burn-through phase. Given a charged particle density of the order of $10^7\,\mathrm{m}^{-3}$, the Debye length is found to be approximately 7.4 m assuming quasi-neutral charge temperature at $T = 10\,\mathrm{eV}$. This is already longer than the major radius of the torus, far longer from what is conventionally recognised as a plasma Debye length scale within a tokamak device.

6.3 Results and discussions

In this section, various physical aspect of the charged particle collective is presented. Comparisons with the 0D model will be made where possible. Since the simulation results are obtained from a 3D spatial setting, some variables could not be compared directly in a meaningful way. As such, specific definitions are proposed and explained. In order to distinguish the values from both 0D model and the numerical simulation, subscript notations will be used. Specifically, subscript of $_{\mathrm{sim.}}$ is used to denote results from simulation and the subscript of $_{\mathrm{0D}}$ refers to values from 0D model.

6.3.1 Electron velocities

First of the comparisons with 0D model is the mean electron drift velocity V_{e}. In the 0D model, $V_{\mathrm{e,0D}}$ is derived from the balance between collisional drag and background field acceleration. This implies that $V_{\mathrm{e,0D}}$ is an averaged electron velocity that is along the subjected electric field. Since the simulation study is carried out in a domain with 3 spatial dimensions, there will be a velocity distribution in both parallel V_{par} and perpendicular V_{perp} direction w. r. t. the torus' minor axis. Furthermore, a positive sign is assigned to velocities that are parallel to the direction of acceleration. Since it is expected that some electrons will be back-scattered, portions of the electron population will have negative velocities. The definition of $V_{\mathrm{e,sim.}}$ in the context of 3D simulation is then the averaged electron V_{par}. With this, the discussion moves onto the time evolution of $V_{\mathrm{e,sim.}}$.

6.3.1.1 $V_{\mathrm{e,sim.}}$ over time

Fig. 6.10 shows the time evolution of $V_{\mathrm{e,sim.}}$ over the course of the simulation. The jagged data points at the early time steps are due to low electron population present in the simulation. Losses of energetic electrons are reflected in the slight drops in $V_{\mathrm{e,sim.}}$. As the simulation proceeds, electron losses persist (as seen later in Fig. 6.13) but the high

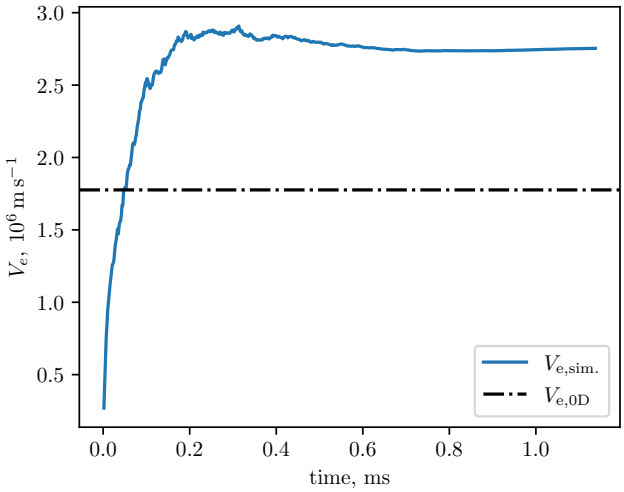

FIGURE 6.10: $V_{\mathrm{e,sim.}}$ over time plot. At the last time step, $V_{\mathrm{e,sim.}}$ is calculated to be $2.74 \times 10^6\,\mathrm{m\,s^{-1}}$ while $V_{\mathrm{e,0D}} = 1.776 \times 10^6\,\mathrm{m\,s^{-1}}$.

population count of electrons average out the impact of such losses on overall $V_{\mathrm{e,sim.}}$. It is seen that $V_{\mathrm{e,sim.}}$ settles to a constant value after peaking at about 0.2 ms, settling at $2.740 \times 10^6\,\mathrm{m\,s^{-1}}$. As previously mentioned, the 0D model also predicts $V_{\mathrm{e,0D}}$ via Eq. 6.2. With the given distribution of E_ϕ in Fig. 6.5, the averaged value within the red boundary is $\sim 0.62\,\mathrm{V\,m^{-1}}$, thus giving $E/p \approx 310\,\mathrm{V\,m^{-1}\,Pa^{-1}}$. As such, the resulting drift velocity is then $V_{\mathrm{e,0D}} = 1.776 \times 10^6\,\mathrm{m\,s^{-1}}$. This value is approximately 35.2 % lower than $V_{\mathrm{e,sim.}}$. The cause for the lower $V_{\mathrm{e,0D}}$ value arises from the assumption that the averaged electron energy in a neutral collision dominated system is at 20 eV. This can be seen in Eq. 2.21, where this assumption is used in the calculation of collisional drag force experienced by electrons.

6.3.1.2 Velocity distribution

The electron's velocity distributions $f(V_{\mathrm{par}})$ and $f(V_{\mathrm{perp}})$ from the simulation are plotted at the same time of 1.1375 ms in Fig. 6.11. It should be noted that the perpendicular velocity distribution is strictly positive since there isn't a preferred orientation due to the periodic nature of electron's V_{perp} velocity vector, arising from the gyration motion centring around the background magnetic field (recall that toroidal electric and magnetic fields are parallel to each other). The electron energy distribution is also shown on the right plot of Fig. 6.11 with an averaged kinetic energy of 98 eV. It should be mentioned here that the value is noticeably higher than the 20 eV assumed in the derivation of Eq. 2.22 (subsequently Eq. 6.2).

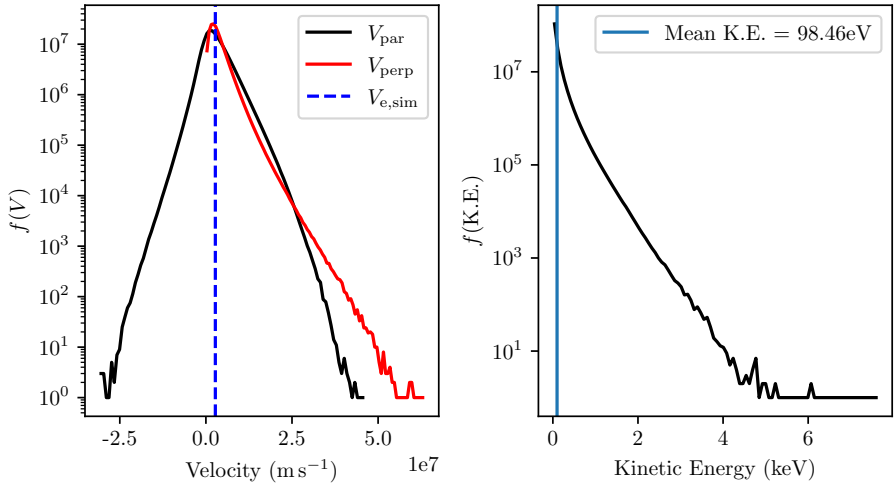

FIGURE 6.11: Plot on the left shows distribution of $f(V_{\mathrm{par}})$ and $f(V_{\mathrm{perp}})$ at $t = 1.1375\,\mathrm{ms}$. Right plot is the corresponding electron energy distribution f(K.E.).

It is important to note that the simulation is performed with the random scatter model described in Sec. 3.4.2.1 since it matched closely with the experimental results discussed in Sec. 5.5.2. The major drawback of this model is the use of a simplified classical interpretation of a hard sphere model to describe the scattering angle distribution. One should be aware that the observed $f(V)$ in Fig. 6.11 would be different should another scattering model is applied instead. An example of such distribution is shown in Fig. 6.12, where the scattering angle distribution arises from the first Born approximation calculation using Ohkrimovvsky *et. al.* model. In such a model, electrons with energies above 12 eV will almost certainly scatter forward which contributes to a much lower population of electrons which are back-scattered (assigned a negative sign). This observation signifies the need for future refinements in which the scattering angle model is derived from a quantum mechanical framework while being able to match the experimentally obtained α in Tab. 5.2.

6.3.2 Growth rate comparison

Fig. 6.13 shows the growth of various charged particle species in time. One notable feature is the discrepancy between the growth rate of electron population as predicted by the theoretical model and the result from simulation. The analytical solution to Eq. 2.19 is

$$n_{\mathrm{e}}(t) = n_{\mathrm{e},0} \exp\left(\gamma_{0\mathrm{D}} t\right). \tag{6.8}$$

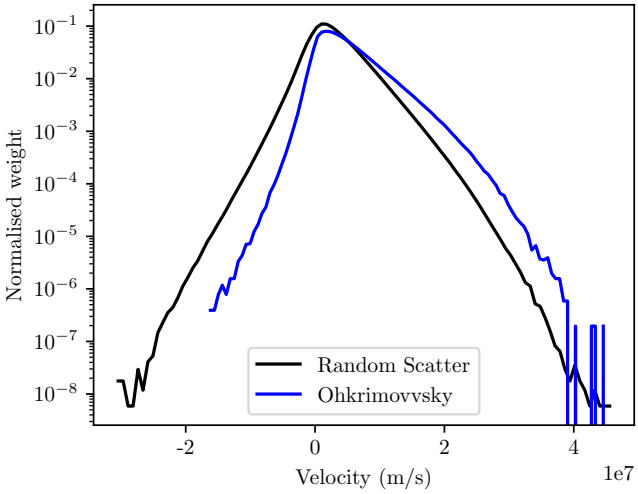

FIGURE 6.12: Comparison of the resulting electron parallel velocity distribution $f(V_{\text{par}})$ scaled by total electrons between the two implemented scattering angle model.

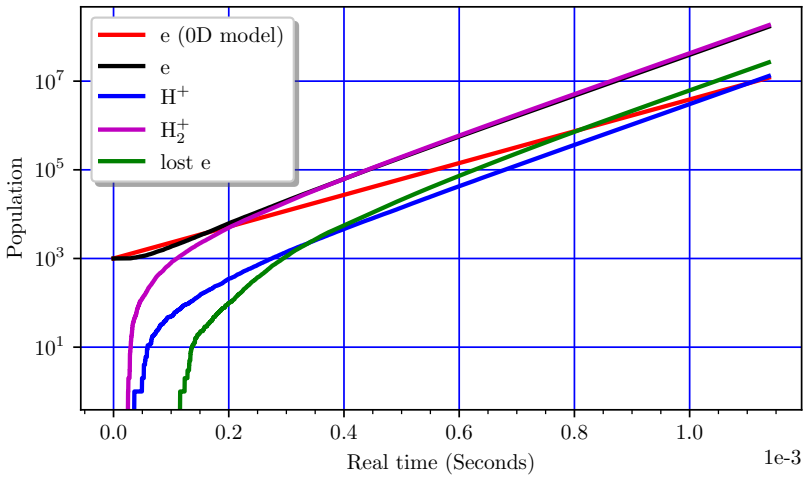

FIGURE 6.13: Population count of electrons, H^+ and H_2^+ ions in time, compared with the electron population growth predicted by Eq. 2.19. The total lost electrons over time is also plotted as well.

TABLE 6.4: Growth constants for both ions and electron, as well as the value from 0D model. All values are in the unit of s^{-1}

γ_{0D}	$\gamma_{i,sim.}$	$\gamma_{e,sim.}$
8257.85	10604.226(16)	10591.848(19)

Applying the operating conditions listed in Tab. 6.1 to Eq. 6.1 yields the value of $\gamma_{0D} = 8257.85\,s^{-1}$. The growth rate of f_i (equivalent to n_e in Eq. 2.19) in this study can be obtained by calculating $\gamma_{e,sim.}$, the growth constant of electron density in time. It is obtained via numerical fitting with a test function that has a similar form to Eq. 6.8, that is

$$n_{e,sim.}(t) = n_{e,sim.}(t_0) \exp\left(\gamma_{e,sim.} t\right). \tag{6.9}$$

The extent of numerical data used for the fitting is determined from Fig. 6.10. Specifically, only the data which the $V_{e,sim.}$ has settled to a constant is used (that is, from the time of $t_0 = 0.8\,ms$ onward). Similar numerical fit can be applied to the ions to obtain $\gamma_{i,sim.}$ using a function akin to Eq. 6.9. Instead of obtaining γ for each species of positive ions, a deliberate choice of combining all ion species in the fitting is made. This is driven by the interest of eventually deriving the electron loss constant $\gamma_{e,loss}$. The result of the numerical fitting is shown in Tab. 6.4.

In the 0D ionisation fraction model, the electron density growth factor in Eq. 6.1 is the difference between the rate of ionisation and the electron loss rate. Following this idea, noticing that $\gamma_{e,sim.}$ represents the net growth of electrons that remain in the simulation domain, it is straightforward to see that this value implicitly includes the electron loss factor as well. As such, the electron loss constant $\gamma_{e,loss}$ is then

$$\gamma_{e,loss} = \gamma_{i,sim.} - \gamma_{e,sim.}. \tag{6.10}$$

Eq. 6.10 is valid, so long as the following conditions hold true. Firstly, the considered ionisation channels only produce one ion-electron pair per event, so that the total ions represent the total electrons produced as if there were no electron losses. Secondly, $\gamma_{i,sim.}$ is obtained from the created ions over time throughout the numerical simulation, rather than the net ion population over the time measure. Eq. 6.10 works well since there were no ion losses up to the time of $\sim$1.14 ms (as seen in Fig. 6.13).

The value of $\gamma_{e,sim.}$ is approximately 28 % higher than γ_{0D}. Assuming that α from Eq. 2.12 holds true for both 0D model and 3D simulation, the difference in V_e is a substantial contributing factor to the diminished γ_{0D}. In the discussion in Sec. 6.3.1.1, the lower value of $V_{e,0D}$ is a result of an overestimation of the collisional drag experienced by the electrons in the 0D model. 3D scattering events introduce perpendicular component

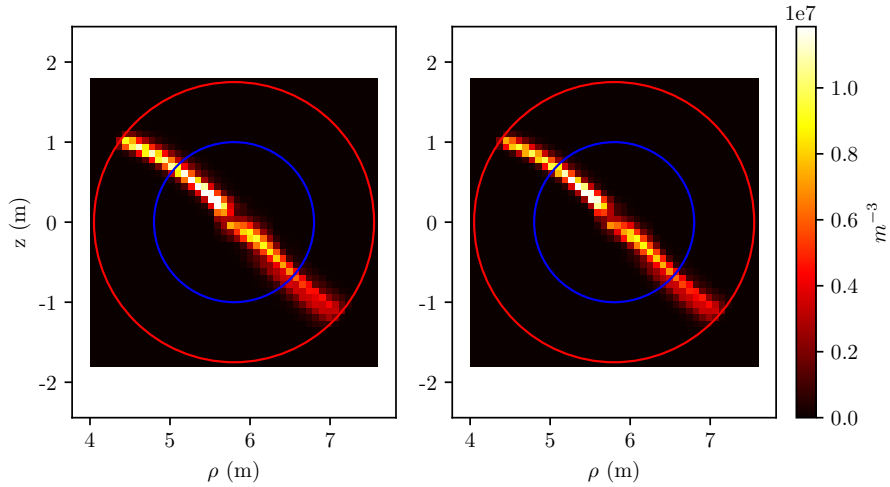

FIGURE 6.14: Density of charges in the poloidal plane. The left shows the ion density while the right plot displays the electron density spatial distribution. The densities are obtained at the time of 1.1375 ms.

to the electrons' velocity vector in the event of scattering, rather than imposing a strict back-scatter which exaggerates the drag force. Lastly, the difference in the assumed connection length L between the 0D model (Eq. 6.1) and the numerical simulation hasn't been examined. This will be covered in the following section.

6.3.3 Charged particle spatial distribution

The definition of the external fields as discussed in Sec. 3.5 implies toroidal symmetry in the simulated domain. As such, the charged particle's density distribution in the poloidal plane is assumed to also inherit such symmetry. The result in Fig. 6.14 shows the distribution of positive ions and electrons respectively at the time of 1.1375 ms. The shape of the charge concentration is influenced by two factors. The first influence is from the poloidal magnetic field $\mathbf{B}_\theta$, and can be represented by a measure akin to the conventional connection length. The second is the internal electric field due to charge imbalance between electrons and ions, which will rise in strength as loss of electrons persists while the heavier ions remain within the simulation domain.

6.3.3.1 Backtraced connection length $L_{\mathbf{bt}}$

There are multiple definitions of connection length L, depending on the context. In the study of scrape-off layers, connection length is defined as the shortest path length of

the field line, which connects the outer midplane and the divertor target in the tokamak [47, 48]. Conversely, the connection length in the study of tokamak startup is the approximated distance along magnetic field line which charged particles are accelerated before coming into contact with the vessel wall [17, 93]. The L by this definition is scaled by

$$L \propto a\frac{B_\phi}{B_\theta},$$

where a refers to the minor radius of the vacuum vessel (or the transverse distance to the vessel wall). The computed L is often a single measure which does not fully represent the spatial distribution of B_θ.

In an attempt to explain the charge distribution as shown in Fig. 6.14, it is found that the backtraced connection length L_{bt} provides a good measure to predict spatial distribution of charges over time. The backtraced connection length L_{bt} is defined as the path length of the background magnetic field line in the orientation parallel to $\mathbf{E}_\phi$, connecting an arbitrarily chosen poloidal plane to the boundary of the domain (e. g. vessel wall). This definition is motivated by the fact that the charged particle spatial distribution is a result of electron-H_2 impact ionisation, meaning that the electron's trajectory will dictate the locations where one can find positive ions. Additionally, the positive ions are found to have energies of less than 29 eV (referring once again to Fig. 6.6). Considering the mass ratio between the electrons and ions, one can safely assume that the ions' motion in a span of ∼1 ms is minimal. This implies that ionisation events determine the distribution of ion density in Fig. 6.14, rather than the ion's own motion. For additional context, it takes a stationary H_2^+ ion approximately 3.4 ms to gain 100 eV, which then only travels at approximately $\sim 133\,\mathrm{m\,s^{-1}}$ in the transverse direction (along the poloidal plane). Consider the time scale of the simulation at 1 ms, a H_2^+ ion with 100 eV will only travel a total of 13.3 cm transversely in that duration.

The computed L_{bt} for the given fields in Sec. 6.2.1 is shown in the left plot of Fig. 6.15, which also shows the different L_{bt} one can obtain by simply flipping the orientation of $\mathbf{E}_\phi$ while keeping the definition of $\mathbf{B}_\phi$ identical. First thing to note is that L_{bt} can reach 10 km, much higher than the assumed $L = 1$ km used in the 0D model. Should L_{bt} be used in Eq. 6.1, this would help increase γ_{0D} value. Revisiting the case where $\mathbf{E}_\phi$ is flipped, the resulting electron density spatial distribution is shown in Fig. 6.16. It corresponds to an earlier time at 0.65 ms and the charge concentration agrees with the L_{bt} map shown in the right plot of Fig. 6.15. The diagonal band of the electron density is wider than seen in Fig. 6.14. This is due to the influence of the second factor mentioned earlier, which is the charge imbalance between electrons and ions. This topic will be discussed further in the following section.

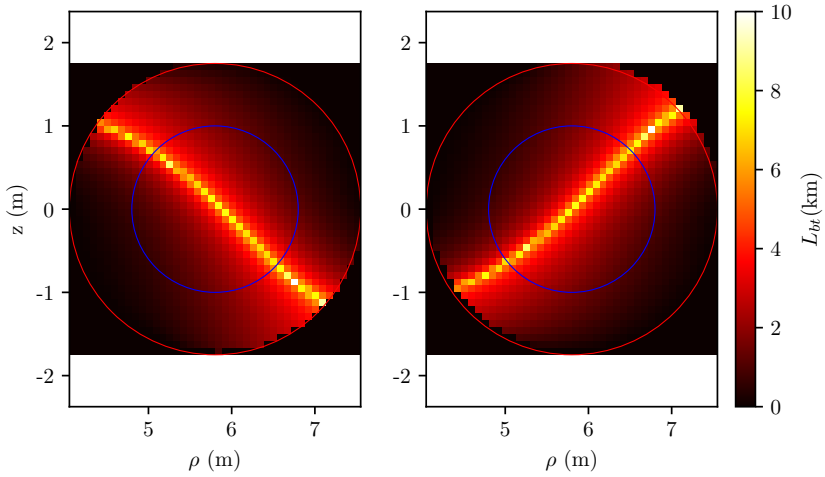

FIGURE 6.15: Map of L_{bt} in the poloidal plane. $\mathbf{E}_\phi$ is parallel to $\mathbf{B}_\phi$ in the left plot, while $\mathbf{E}_\phi$ is anti-parallel on the right plot.

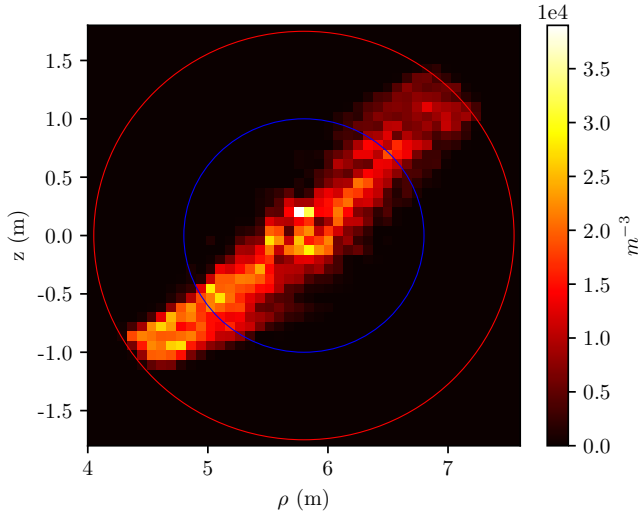

FIGURE 6.16: Electron density in the poloidal plane at 0.65 ms, $\mathbf{E}_\phi$ is anti-parallel to the prescribed $\mathbf{B}_\phi$.

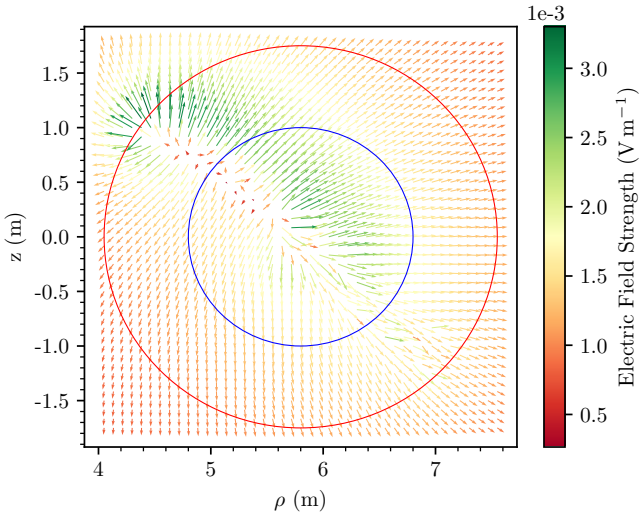

FIGURE 6.17: $\mathbf{E}_{\text{int.}}$ due to charge imbalance between electrons and ions.

6.3.3.2 Internal fields

While Fig. 6.14 shows similar magnitude of density between the electrons and ions, there is in fact a charge imbalance. Specifically, electron density is lower than ion density due to the continuous electron loss in time (seen in Fig. 6.13). The charge imbalance is clearly demonstrated by the resulting internal electric field $\mathbf{E}_{\text{int.}}$ shown in Fig. 6.17. Such field then encourages the electrons to move toward the diagonal axis. The impact of the resulting $\mathbf{E}_{\text{int.}}$ on the spatial distribution of electrons is demonstrated via an identical simulation setup, but with the absence of such field. The result is shown in Fig. 6.18, which shows a larger concentration of electrons at the edge of the simulation domain. Due to the internal field, the electron loss rate is reduced. This can be seen in Fig. 6.19, when the recorded number of lost electrons (blue solid line) is compared to a data fitted reference exponential losses in time (black dashed line). The plot on the right highlights the reducing electron loss over time when compared to a purely exponential function. This shows the importance of computing $\mathbf{E}_{\text{int.}}$, even though the field strength is two orders of magnitude smaller than the dominant toroidal electric field.

Aside from the internal electric field, another important consideration is the resulting internal magnetic field $\mathbf{B}_{\text{int.}}$ due to the current density J. Fig. 6.20 shows the measured current density and the corresponding internal magnetic field. Considering that the magnitude of $\mathbf{B}_\theta$ is of mT, $\mathbf{B}_{\text{int.}}$ is negligible as it is approximately 10 orders of magnitude lower. Thus, neglecting the computation of $\mathbf{B}_{\text{int.}}$ is justified up to the order of $\sim$1 ms. This means that the magnetic stray field $\mathbf{B}_\theta$ continuously causes the loss of electrons,

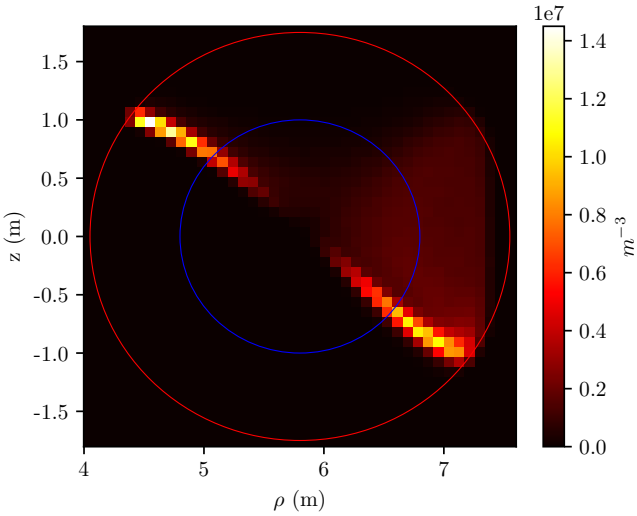

FIGURE 6.18: Density of electron in the poloidal plane in the absence of $\mathbf{E}_{\text{int.}}$.

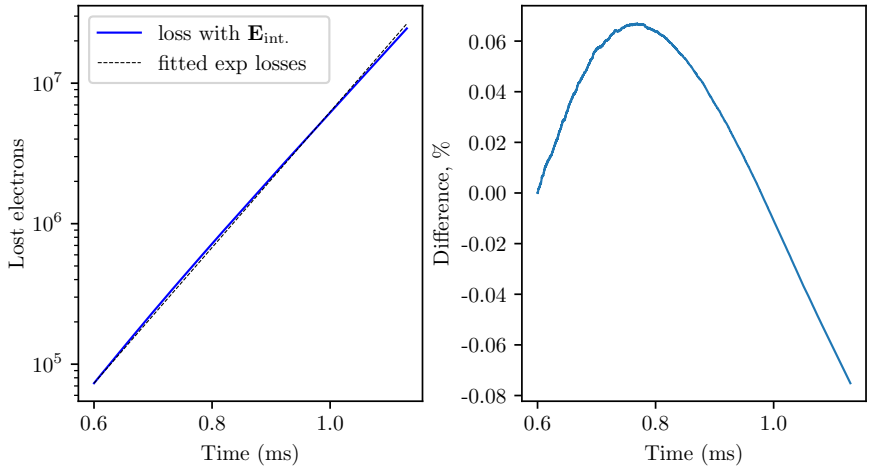

FIGURE 6.19: The left plot shows the electron losses with $\mathbf{E}_{\text{int.}}$ and the data fitted exponential losses. Right plot is the percentage difference between the two to highlight the slowing electron loss rate.

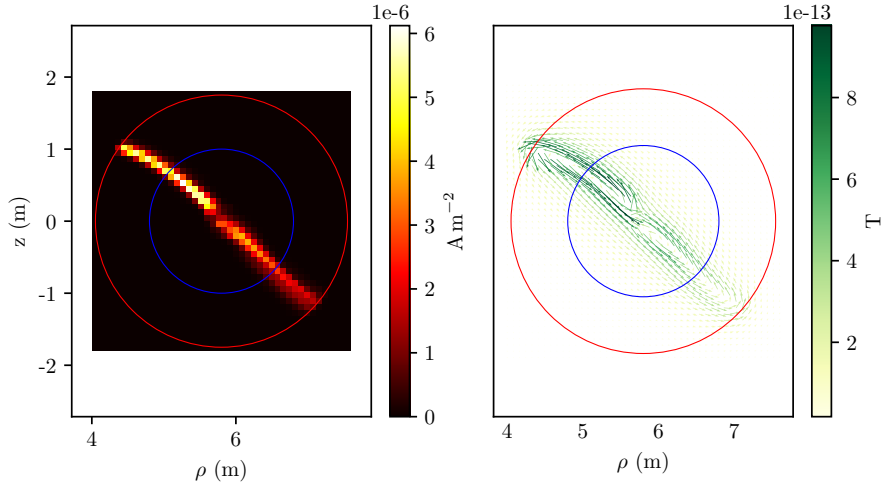

FIGURE 6.20: Left plot is the measured current density J (A m^{-2}), followed by the corresponding internal magnetic field $\mathbf{B}_{\text{int.}}$ (T) at the time of 1.1375 ms.

until the current density develops to the threshold needed to form a closed magnetic flux surface (which the confinement property of charges drastically improves). Referring to Fig. 6.20, one can surmise that the first location of such closed flux surface is likely to form at the top left quadrant of the poloidal plane. For this numerical study to remain valid while neglecting the computation of the internal magnetic field, an estimate of the time when $\mathbf{B}_{\text{int.}}$ becomes comparable in magnitude with $\mathbf{B}_\theta$ is required. This will be discussed in the following section.

6.3.4 Extrapolation in time

The results shown so far mostly focused on the very last time step of the simulation, which corresponds to the time of ∼1.14 ms. However, the time evolution of the charged particle system is recorded throughout the simulation. Thus, it is possible to extrapolate the various quantities to a future time.

6.3.4.1 Time evolution of electron V_{par}

The 0D ionisation fraction model considered the velocity component parallel to the field of acceleration as the electron drift velocity. As such, the time evolution of electrons' V_{par} distribution is of interest and the result at the time of 1.1375 ms were presented in Fig. 6.11. The V_{par} result suggests that the electrons settle to a Gaussian distribution. However, study on the variations of background $\mathbf{B}_\theta$ (later in Ch. 7) yielded V_{par}

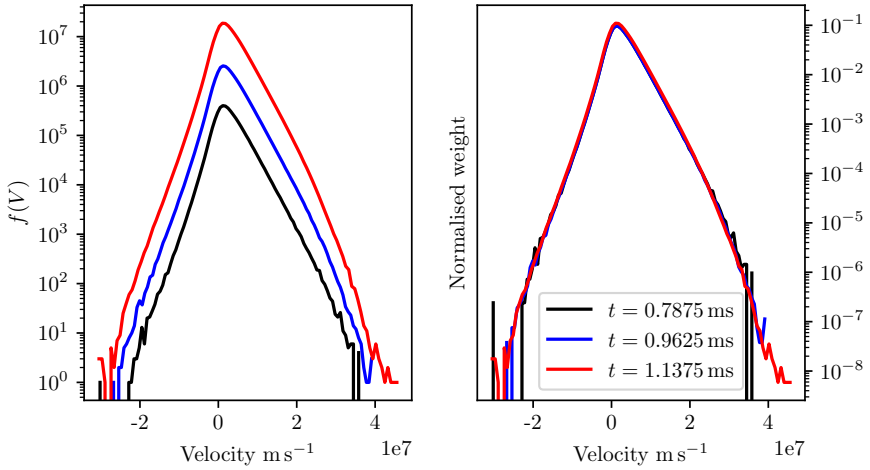

FIGURE 6.21: V_{par} distribution of electrons ($f(V'_{\text{par}})$) at different times. The right plot is the corresponding velocity distribution scaled by the total electron population of respective times.

distributions that deviate from Gaussian distribution. This showed that the Gaussian distribution cannot be generalised to the obtained V_{par} distribution. Even so, parameterisation of the distribution can be useful to project the expected velocity distribution to future times. Since the larger sample size of electrons at later times suit better for numerical fit, the data from the time of 1.1375 ms is the chosen candidate for parameterisation.

It is found that the distribution of V_{par} remains consistent over time after the value of $V_{\text{e,sim.}}$ has settled, as shown in Fig. 6.21. The major difference is the vertical offset between the measured times, which can be predicted if $\gamma_{\text{e,sim.}}$ is known. The scaled V_{par} distribution of electrons ($f'(V'_{\text{par}})$) is fitted using the help of Padé approximant, which has the following form

$$f'(V'_{\text{par}}) = \frac{\sum_{i=0}^{m} c_i V'^{i}_{\text{par}}}{1 + \sum_{j=1}^{m} d_j V'^{j}_{\text{par}}}, \tag{6.11}$$

where

$$f'(V'_{\text{par}}) = \log\left(f(V'_{\text{par}})^2/N_{\text{e}}\right)$$
$$V'_{\text{par}} = (V_{\text{par}} - V_{\text{par, min}})10^{-7},$$

$f(V'_{\text{par}})$ is the number of electrons that moves at a scaled velocity of V'_{par}. A deliberate choice is made here to cap the terms of denominator and numerator by the same number m, in order to reduce the number of variables for the numerical fitting process. Once the fitting parameters c_i and d_j are found, the fitted electron numbers can be computed

TABLE 6.5: Fit parameters to reconstruct electron $V_{\parallel}$ distribution at $t = 1.1375\,\mathrm{ms}$. $V_{\parallel}$ range is also provided.

c_0	-1.87662460e+01	d_1	-9.63739644e+00
c_1	1.99571755e+02	d_2	5.98349954e+00
c_2	-2.32624103e+02	d_3	-9.72059062e-01
c_3	1.02000897e+02	d_4	-9.36906534e-02
c_4	-1.96568263e+01	d_5	3.74309256e-02
c_5	1.38798155e+00	d_6	-3.13912751e-03
$V_{\parallel,\,\mathrm{min}}$	$-3.044 \times 10^7\,\mathrm{m\,s^{-1}}$	$V_{\parallel,\,\mathrm{max}}$	$4.555 \times 10^7\,\mathrm{m\,s^{-1}}$
N_e	169708704		

via

$$f_{\mathrm{fit}}(V'_{\parallel}) = \sqrt{N_\mathrm{e} \exp\left(\frac{\sum_{i=0}^{m} c_i V'^{i}_{\parallel}}{1 + \sum_{j=1}^{m} d_j V'^{j}_{\parallel}}\right)}. \tag{6.12}$$

Once $f_{\mathrm{fit}}(V'_{\parallel})$ is computed, it is directly the value corresponding to the $V_{\parallel}$ that was used to compute $V'_{\parallel}$. The optimal m terms in Eq. 6.11 and Eq. 6.12 is chosen by minimising the relative error Δf, defined as

$$\Delta f = \sum_k \frac{\sqrt{\left(f_{\mathrm{fit}}(V'_{\parallel,k}) - f(V'_{\parallel,k})\right)^2}}{f(V'_{\parallel,k})}.$$

The fitted parameters for the presented $V_{\parallel}$ distribution in Fig. 6.21 are tabulated in Tab. 6.5. In order to construct the electron $V_{\parallel}$ distribution at an arbitrary time t', perform the numerical evaluation of

$$f_{\mathrm{num}}(V'_{\parallel}, t') = f_{\mathrm{fit}}(V'_{\parallel}) \exp\left(\gamma_{\mathrm{e,sim.}}(t' - t_0)\right), \tag{6.13}$$

where t_0 is the time point of the data that was parameterised, which is 1.1375 ms in this case. Note that the resulting $f_{\mathrm{num}}(V'_{\parallel}, t')$ is valid for $t' = [0.80\,\mathrm{ms}, 2.75\,\mathrm{ms}]$. Fig. 6.22 shows the comparisons between $f(V'_{\parallel})$ and $f_{\mathrm{num}}(V'_{\parallel})$ at different times, which shows good agreement between actual and fitted distribution. Since electrons are counted in integers, it is recommended to round down $f_{\mathrm{num}}(V'_{\parallel})$ values. Such rounding will have minimal impact to the overall $V_{\parallel}$ distribution since the total electron population is above 10^6 from 0.8 ms onward.

6.3.4.2 Formation of closed magnetic field

As mentioned briefly before, continuous loss of electrons is expected in the absence of closed magnetic flux surfaces, therefore it is interesting to estimate the time when such surfaces emerge. In order to do so, a time series of $\mathbf{B}_{\mathrm{int.}}$ poloidal map (specifically the

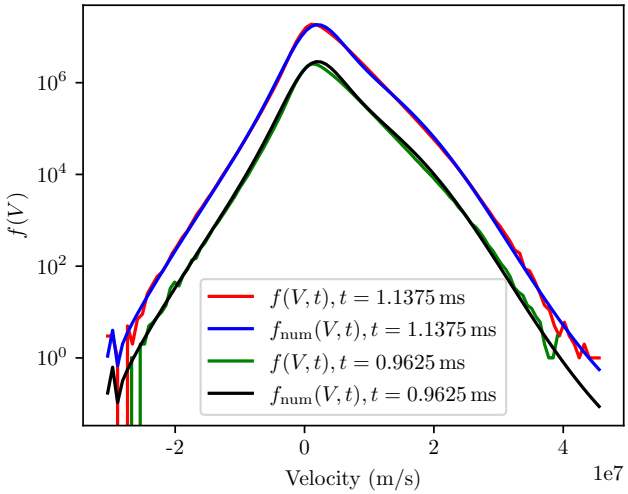

FIGURE 6.22: Comparison between actual electron V_{par} distribution and fitted distribution f_{fit} at different times.

top left quadrant) over time is taken. The time series taken ranges from 0.8 ms up to 1.1 ms. An assumption is made such that the unit vector map of $\mathbf{B}_{\mathrm{int.}}$ is time invariant from $t = 0.8$ ms onward. Aside from that, it is observed that the magnitude rises in an exponential manner akin to the fitted $\gamma_{\mathrm{sim.}}$ (See Fig. 6.23). Numerical fitting is then performed onto the $\|\mathbf{B}_{\mathrm{int.}}\|$ poloidal map time series with a test function of the form

$$\|\mathbf{B}_{\mathrm{int.}}(\mathbf{x}, t)\| = \|\mathbf{B}_{\mathrm{int.}}(\mathbf{x}, t_0)\| \exp(C_{\mathrm{B}}(\mathbf{x})\ t), \tag{6.14}$$

with $\mathbf{x}$ denoting the spatial coordinates of grid points on the poloidal map, $t_0 = 0.8$ ms and C_{B} the fitted exponential growth factor of $\|\mathbf{B}_{\mathrm{int.}}\|$.

The critical time $t_{\mathrm{crit.}}$ that closed magnetic field is formed, is approximately when the condition

$$\|\mathbf{B}_{\mathrm{int.}}(\mathbf{x}, t_{\mathrm{crit.}})\| \geq \|\mathbf{B}_{\theta}(\mathbf{x})\|, \quad \forall \mathbf{x} \tag{6.15}$$

is fulfilled. Combining Eq. 6.14 and Eq. 6.15, then $t_{\mathrm{crit.}}$ is

$$t_{\mathrm{crit.}} = \min\left(\{t(\mathbf{x}) : \log\left(\|\mathbf{B}_{\theta}(\mathbf{x})\| - \|\mathbf{B}_{\mathrm{int.}}(\mathbf{x}, t_0)\|\right) / C_{\mathrm{B}}(\mathbf{x}), \forall \mathbf{x}\}\right). \tag{6.16}$$

Numerically evaluating Eq. 6.16 yields a $t_{\mathrm{crit.}} = 2.75$ ms, which the computation of $\mathbf{B}_{\mathrm{int.}}$ becomes crucial for the proper plasma breakdown to be simulated. Fig. 6.24 shows the map of computed $t_{\mathrm{crit.}}$ in the poloidal plane. The electron number density is projected to reach $1.27 \times 10^{13}\,\mathrm{m}^{-3}$ with a corresponding Debye length of 6.6 mm at such $t_{\mathrm{crit.}}$.

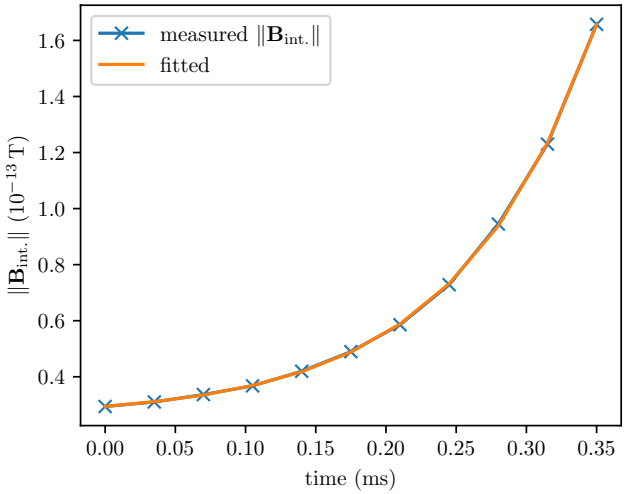

FIGURE 6.23: Time evolution of local $\|\mathbf{B}_{\text{int.}}\|$ at $\rho = 6.05\,\text{m}$ and $z = -1\,\text{m}$. The numerical fit of Eq. 6.14 is shown as well. This numerical extrapolation is performed at every grid point in Fig. 6.24.

The electron plasma frequency ω_{pe} will then be approximately $201 \times 10^6\,\text{rad}\,\text{s}^{-1}$ and the total current is $63(7)\,\text{A}$ at $t_{\text{crit.}}$. The plasma frequency has already been discussed prior that it is orders of magnitude lower than the frequency of the calculation of $\mathbf{E}_{\text{int.}}$. It is also interesting to consider the effects of Coulomb collision at this point. The expression for electron-ion scattering frequency ν_{ei} [94] due to Coulomb collision is given as

$$\nu_{\text{ei}} \approx \frac{\sqrt{2}\omega_{\text{pe}}^4}{64\pi n_{\text{e}}} \left(\frac{k_{\text{B}} T_{\text{e}}}{m_{\text{e}}} \right)^{-3/2}. \tag{6.17}$$

n_{e} refers to the electron number density, m_{e} denotes the electron rest mass and T_{e} is the electron temperature. The resulting ν_{ei} is then approximately $1.2 \times 10^{-2}\,\text{Hz}$, which is clearly much lower than either ω_{pe} and electron's gyrofrequency. As such, the prescribed frequency of the calculation of $\mathbf{E}_{\text{int.}}$ is more than enough to capture the effects of Coulomb collision.

6.3.4.3 Extrapolation of $\mathbf{E}_{\text{int.}}$

The self-consistent electric field $\mathbf{E}_{\text{int.}}$ due to ion-electron charge imbalance at the time of 1.14 ms is shown in Fig. 6.17. The prior observation is that the existence of $\mathbf{E}_{\text{int.}}$ reduces the loss of electrons over time. It is of specific interest to predict the maximum $\mathbf{E}_{\text{int.}}$ should the electron loss rate up to 1.14 ms is sustained.

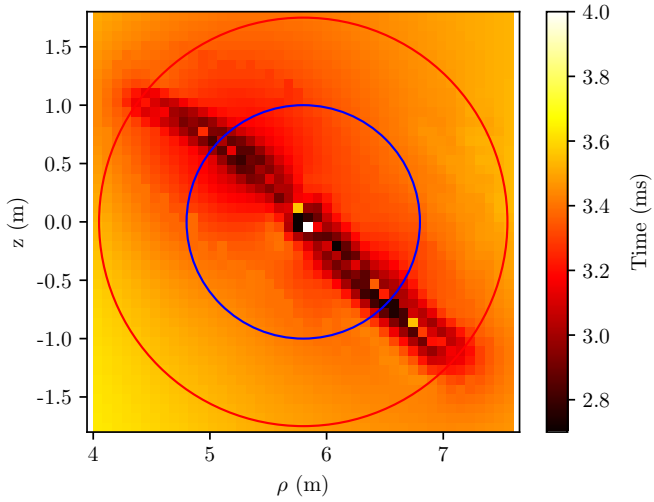

FIGURE 6.24: Computed $t_{\text{crit.}}$ across the poloidal plane.

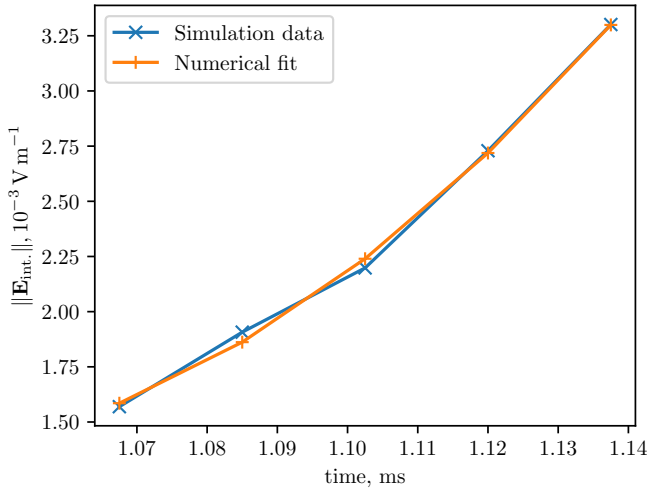

FIGURE 6.25: Time series plot of maximum $\mathbf{E}_{\text{int.}}$. The numerically fitted data is also shown for comparison.

The steps involved start by identifying the location where $\mathbf{E}_{\text{int.}}$ is maximum at the time of 1.14 ms. This is then followed by the time record of $\|\mathbf{E}_{\text{int.}}\|$ at that specific location. A numerical fitting is performed and the resulting parameters are used to extrapolate the predicted magnitude at $t_{\text{crit.}}$. Fig. 6.25 shows the result. The obtained $\|\mathbf{E}_{\text{int.}}\|$ at the time of 2.75 ms is then approximately 0.49 V m^{-1}. However, this value is likely an over-exaggeration.

Consider an extreme case of highly energetic electron with an initial energy of 6 keV positioned at a minor radius of 1 m moving in the toroidal direction, the predicted $\|\mathbf{E}_{\text{int.}}\|$ required to deter said electron from leaving the simulation domain can be calculated. The averaged poloidal field strength on the edge of the simulation domain $\|\mathbf{B}_{\theta,\text{edge}}\|$ is calculated to be 3.6 mT, the electron's transverse velocity $V_\perp$ is then approximately $63.6\,\text{km}\,\text{s}^{-1}$ assuming that $\|\mathbf{B}_\phi\| = 2.6\,\text{T}$. The value of $V_\perp$ is obtained via

$$V_\perp \propto V_\parallel \frac{B_\theta}{B_\phi} \tag{6.18}$$

where B_θ and B_ϕ denote the poloidal and toroidal magnetic field strength respectively. Recalling that the shortest distance to the simulation edge is just 0.75 m for this particular electron, a rudimentary calculation of the required $\|\mathbf{E}_{\text{int.}}\|$ to decelerate and confine this electron is done through kinematic equations. The required $\|\mathbf{E}_{\text{int.}}\|$ comes out to be approximately $0.03\,\text{V}\,\text{m}^{-1}$, which is an order of magnitude lower than the $0.49\,\text{V}\,\text{m}^{-1}$ obtained via simple time series extrapolation. In other words, electron losses will diminish significantly once $\|\mathbf{E}_{\text{int.}}\|$ is in the order of $10^{-2}\,\text{V}\,\text{m}^{-1}$, and ion-electron charge imbalance will not increase to the point where $\|\mathbf{E}_{\text{int.}}\|$ reaches $0.49\,\text{V}\,\text{m}^{-1}$.

A more detailed methodology or model is needed, should one insist on predicting the time evolution of $\|\mathbf{E}_{\text{int.}}\|$ without committing to the detailed numerical simulation.

6.4 Conclusion

A numerical study of the first plasma scenario in ITER-like tokamak has been conducted. The simulation is performed with a simplified quadrupole magnetic stray field $\mathbf{B}_\theta$. Comparisons with the discussed 0D ionisation fraction model are made, focusing on the V_e and L variable. It is found that the 0D model underestimates both the measures, which leads to an overall lower $\gamma_{0\text{D}}$ compared to the simulation results. The spatial distribution of charges in the poloidal plane is also found to correspond closely with the newly defined L_bt measure. This is true so long as $\mathbf{B}_\theta$ remains dominant.

The computed internal magnetic field at 1.1375 ms shows that it falls far short in comparison to the background poloidal field $\mathbf{B}_\theta$. Approximately 10 orders of magnitude lower, thus it can still be considered negligible. However, assuming the exponential growth rate of charged particles in Fig. 6.13 continues, the gap in magnitude will be narrowed significantly in the timescale of milliseconds. It is then possible to have a closed magnetic field structure which will significantly alter the confinement property of charged particles, reducing the overall charged particle loss rate. This is estimated to

happen approximately at the time of 2.75 ms.

The parallel velocity distribution of electrons $f(V_{\mathrm{par}})$ exhibits self-similar behaviour provided that the electron mean drift velocity $V_{\mathrm{e,sim.}}$ has already settled to a constant. Combining the obtained $\gamma_{\mathrm{e,sim.}}$ and the f_{fit} data, one could predict the electron V_{par} distribution at a given time (Eq. 6.13). Additionally, one must recall that the $f(V_{\mathrm{par}})$ distribution is a result of a hard-sphere collision assumption. Switching to a scattering angle model derived via first Born approximation gives a starkly different distribution (Fig. 6.12) at the cost of a diminished ionisation fraction growth rate. A new and improved scattering angle model which is more physically accurate while best approximating the first Townsend coefficient α is required.

It should be mentioned that numerical fitting via the use of Padé approximant provides a good approximation of the actual $f(V_{\mathrm{par}})$ distribution. Gaussian distribution fit is ultimately discarded for the reason that it cannot be generalised to all the variant configurations of $\mathbf{B}_{\phi}$ and $\mathbf{B}_{\theta}$. More details are shared in the following chapter, where the influence of prescribed $\mathbf{B}_{\phi}$ and $\mathbf{B}_{\theta}$ on the different γ values will be explored.

Chapter 7

Variants of ITER-like plasma breakdown

The field configuration and the operating conditions of an ITER-like tokamak have been discussed in Ch. 6. A multitude of various magnetic field configurations will now be explored in order to understand the impact of different $\mathbf{B}_\phi$ and $\mathbf{B}_\theta$ onto the calculated L_{bt} as well as the resulting γ values. The discussed configurations are idealisation of the magnetic fields during an operation of ITER-like tokamak. The various field configurations will be detailed first, which is then followed by the respective results from the simulations.

7.1 ITER-like tokamak scenario variants

In order to easily identify the various scenarios, they will be assigned a number individually. Since one such scenario has already been discussed in Ch. 6, it will now be referred to as scenario Sce. 0 moving forward. The specific $\mathbf{B}_\phi$ and $\mathbf{B}_\theta$ configurations are discussed first. Five additional configurations are simulated, and two of them involve an octupole $\mathbf{B}_\theta$ configuration. The three quadrupole configurations are first described.

The positions of the coils are identical to the tabulated data in Tab. 7.1, but carry different currents I. Combined with the prescribed $I_{\mathbf{B}_\phi}$ value for use in Eq. 3.35, the parameters fully describe the magnetic field configurations in 3D.

All the listed scenarios share the same null point at $\rho = 5.8\,\mathrm{m}$ and $z = 0\,\mathrm{m}$. The resulting $\mathbf{B}_\theta$ vector map is similar to Fig. 6.4, the respective poloidal magnetic field strength at null point $B_{\theta,\mathrm{null}}$, averaged poloidal field strength within the minor radius of $1.75\,\mathrm{m}$ $\langle B_\theta \rangle$

TABLE 7.1: Currents (A) running through the numbered coils for quadrupole $\mathbf{B}_\theta$ configuration, as well as the $I_{\mathbf{B}_\phi}$ for $\mathbf{B}_\phi$.

Coil no.	Sce. 1	Sce. 2	Sce. 3
1	2357.4	2357.4	1178.7
2	2357.4	2357.4	1178.7
3	100 000.0	100 000.0	50 000.0
4	14 999.9	14 999.9	7499.9
$I_{\mathbf{B}_\phi}$	7.524×10^7	1.505×10^8	7.524×10^7

TABLE 7.2: Computed $B_{\theta,\text{null}}$, $\langle B_\theta \rangle$, $\langle B_{\theta,\text{edge}} \rangle$ and B_ϕ in Tesla for each scenario, Sce. 0 is included as a reference.

	Sce. 0	Sce. 1	Sce. 2	Sce. 3
$B_{\theta,\text{null}}$	3×10^{-5}	10^{-8}	10^{-8}	10^{-8}
$\langle B_\theta \rangle$	2.205×10^{-3}	2.193×10^{-3}	2.193×10^{-3}	1.096×10^{-3}
$\langle B_{\theta,\text{edge}} \rangle$	3.613×10^{-3}	3.596×10^{-3}	3.596×10^{-3}	1.798×10^{-3}
$B_{\phi,\text{null}}$	2.6	2.6	5.2	2.6

TABLE 7.3: Coil positions/dimensions and the corresponding current for Sce. 4 octupole $\mathbf{B}_\theta$ configuration

Coil no.	z' (m)	R (m)	I (kA)
1	3.0	5.905	19.94
2	-3.0	5.905	19.94
3	0.0	2.905	21.1
4	0.0	8.905	20.1
5	2.121	7.976	−20
6	-2.121	7.976	−20
7	2.121	3.834	−20
8	-2.121	3.834	−20

and the averaged strength on the domain edge $\langle B_{\theta,\text{edge}} \rangle$ are tabulated in Tab. 7.2. The toroidal field strength at the null $B_{\phi,\text{null}}$ is also included for reference.

The two remaining cases with octupole $\mathbf{B}_\theta$ field configuration is detailed here. The coil positions and the respective currents are listed in Tab. 7.3 and Tab. 7.4. As with the previously discussed setup, the values are used in conjunction with Eq. 3.34 to compute the $\mathbf{B}_\theta$ values. It should be mentioned that 4 of the 8 coils have their current flowing in the opposite direction, so that a circular area with minimal $\mathbf{B}_\theta$ field vector is created around the torus' minor axis. This can be seen in Fig. 7.1, which shows the resulting $\mathbf{B}_\theta$ for the Sce. 5 configuration. Tab. 7.5 shows the corresponding overview variables of $\mathbf{B}_\theta$ in Sce. 4 and Sce. 5 for comparison. Drawing attention to the difference between $\langle B_\theta \rangle$ and $\langle B_{\theta,\text{edge}} \rangle$ among the quadrupole and octupole configuration, it is immediately clear that the differences are lesser in Sce. 4 and Sce. 5. This is an indication that the octupole configuration has less $\|\nabla B_\theta\|$ radially.

TABLE 7.4: Coil positions/dimensions and the corresponding current for Sce. 5 octupole $\mathbf{B}_\theta$ configuration

Coil no.	z' (m)	R (m)	I (kA)
1	3.625	6.01	19.97
2	-3.625	6.01	19.97
3	0.0	2.385	20.95
4	0.0	9.635	20
5	2.562	8.484	−19.9775
6	-2.562	8.484	−19.9775
7	2.584	3.557	−19.9805
8	-2.584	3.557	−19.9805

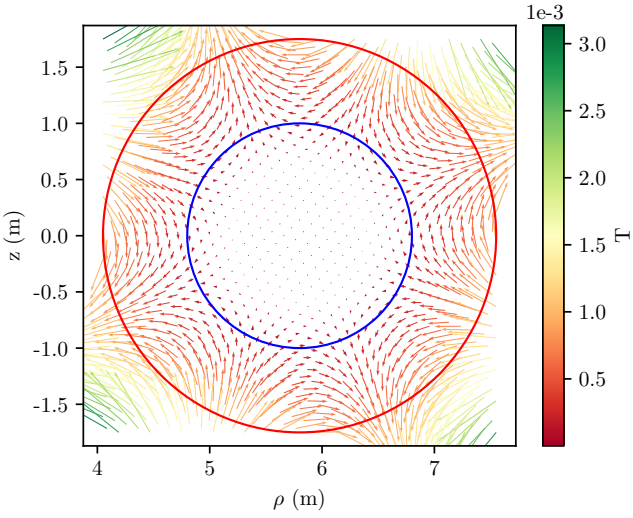

FIGURE 7.1: $\mathbf{B}_\theta$ vector field of Sce. 5.

TABLE 7.5: Computed $B_{\theta,\text{null}}$, $\langle B_\theta \rangle$, $\langle B_{\theta,\text{edge}} \rangle$ and B_ϕ in Tesla.

	Sce. 4	Sce. 5
$B_{\theta,\text{null}}$	1.07×10^{-8}	1.02×10^{-8}
$\langle B_\theta \rangle$	0.832×10^{-3}	0.382×10^{-3}
$\langle B_{\theta,\text{edge}} \rangle$	0.896×10^{-3}	0.402×10^{-3}
$B_{\phi,\text{null}}$	2.6	2.6

The remaining operating conditions, such as $\mathbf{E}_\phi$ and those listed in Tab. 6.1 remain unchanged. Due to the immense computational cost involved, we cannot afford to do detailed parameter scans. As a reference, the presented simulation in Ch. 6 consumed upwards of 3 million core-hours in computation resources on FZJ's Jureca-Booster module. Some of the data sets shown here were truncated in time, due to the depletion of available computational resources. Specifically, Sce. 1 reached the same termination point of Sce. 0 at 1.1375 ms, while Sce. 2 and 3 stopped at 1 ms. Sce. 4 and 5 terminate earliest at the time of 0.9 ms. Ideally, we would like to extend the simulation to each scenario's respective $t_{\text{crit.}}$ when local closed magnetic flux surfaces start to form. In order to achieve that, the discussed merging algorithm in Ch. 4 can be used to reduce the computational load introduced by an exponentially increasing number of charged particles. This provides an avenue for future extended study.

7.2 $L_{\mathbf{bt}}$ comparison

It should be mentioned here that the implemented streakline integral algorithm imposes an upper limit on the maximum L_{bt} that can be computed. It is due to a combination of the limited duration (a full 24 h run) allowed for a submitted computation on the supercomputer, as well as the algorithm's inability to save the results and resume computation at a later time. Thus, the streakline integral terminates upon L_{bt} reaching 10 km. A total of 100 points are computed in both z and ρ direction. This problem can be alleviated if the total number of points to compute the streakline integral is reduced, so that the numerical computation can be completed within the time limit. The result of L_{bt} map for all secnarios are shown in Fig. 7.2, areas coloured white have at least 10 km in L_{bt}.

The given quadrupole magnetic field configuration of Sce. 1 is very similar to Sce. 0, aside from the lower $B_{\theta,\text{null}}$ value. Since the resulting $\langle B_\theta \rangle$, $B_{\theta,\text{edge}}$ and $B_{\phi,\text{null}}$ are all comparable, the resulting L_{bt} for Sce. 1 is expected to look similar to Sce. 0. Since the null point is located at the middle of the highlighted circles, it is expected that the longest L_{bt} is in the same proximity. In the case of Sce. 0, the maximum L_{bt} within the blue circle is recorded at 8.5 km while Sce. 1 records multiple locations where $L_{\text{bt}} = 10$ km. This result is due to Sce. 1 having a much lower $B_{\theta,\text{null}}$.

The computed L_{bt} of Sce. 2 and Sce. 3 shows a notable difference to both Sce. 0 and Sce. 1. Although the L_{bt} remains capped at 10 km, the result shows a much larger area that has such maximum measure. This result demonstrates that doubling B_ϕ has similar effect to halving B_θ, both increasing the obtained L_{bt}. Finally, the obtained

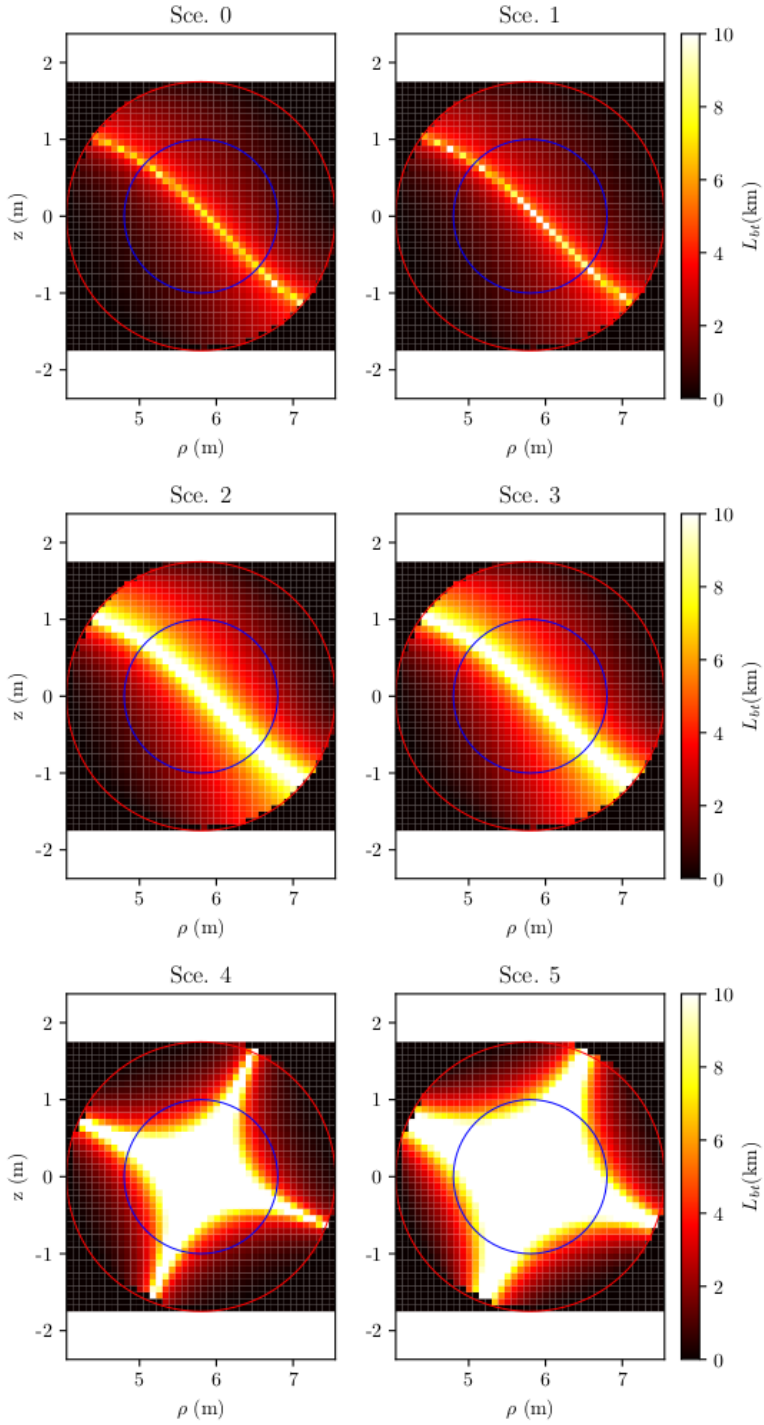

FIGURE 7.2: Map of L_{bt} for all scenarios.

TABLE 7.6: Computed $\langle L_{\mathrm{bt,\ seed}} \rangle$ for all scenarios.

	Sce. 0	Sce. 1	Sce. 2	Sce. 3	Sce. 4	Sce. 5
$\langle L_{\mathrm{bt,\ seed}} \rangle$, km	1.880	1.880	3.760	3.760	5.833	11.32

TABLE 7.7: $V_{\mathrm{e,sim.}}$ for all scenarios.

	Sce. 0	Sce. 1	Sce. 2	Sce. 3	Sce. 4	Sce. 5
$V_{\mathrm{e,sim.}}$, $10^6\,\mathrm{m\,s^{-1}}$	2.74	2.75	3.02	3.02	3.30	3.37

L_{bt} for an octupole field configuration shows such field creates a pattern which has 4 'limbs' where fast moving electrons can travel and eventually leave the simulated domain.

Although the results in Fig. 7.2 showed the L_{bt} for different $\mathbf{B}_\theta$ and $\mathbf{B}_\phi$, it is rather unfortunate that an uncapped L_{bt} map is not available at the time of writing. However, it is still helpful to understand the magnitude of the expected L_{bt} for the different setups. As such, a measure of $\langle L_{\mathrm{bt,\ seed}} \rangle$ is introduced and defined as the average of the computed L_{bt} on the torus surface which encapsulates all seeded electrons at the initial state of the simulations. This corresponds to the blue circle in Fig. 7.2. $\langle L_{\mathrm{bt,\ seed}} \rangle$ is defined because it can be interpreted as the averaged minimum L_{bt} experienced by the electrons at the start of the simulations. Additionally, such value can be computed without imposing the artificial 10 km cap since 256 evenly distributed compute points along the blue circle are used for the streakline integral, which is much lower than 10 000 points required to produce a full L_{bt} map. The results of such measure for all considered scenarios are tabulated in Tab. 7.6.

7.3 Electron V_{par} distribution

The averaged electron drift velocity V_{e} was previously defined in Sec. 6.3.1 and the same definition applies here. Even though the simulation time is truncated for Sce. 2, 3, 4 and 5, the recorded $V_{\mathrm{e,sim.}}$ already settle to a constant value at the time of 0.8 ms. $V_{\mathrm{e,sim.}}$ for each scenario is tabulated in Tab. 7.7. Comparing the results in Tab. 7.7 and Tab. 7.6, it can be observed that $V_{\mathrm{e,sim.}}$ tend to be higher with a longer $\langle L_{\mathrm{bt,\ seed}} \rangle$. However, the relationship between the two observables cannot be clearly established. Doubling the $\langle L_{\mathrm{bt,\ seed}} \rangle$ (between Sce. 1 and Sce. 2) resulted in approximately 9.81 % rise in $V_{\mathrm{e,sim.}}$. This trend does not apply to the comparison between Sce. 4 and Sce. 5, which only recorded a rise of 2.12 %. This may suggest that there is a threshold of $\langle L_{\mathrm{bt,\ seed}} \rangle$ where higher values don't have a notable impact on the resulting $V_{\mathrm{e,sim.}}$.

Comparison of normalised electron parallel velocity distribution $f(V_{\mathrm{par}})$ at the final simulated time (obtained by dividing the distribution with the respective total electron

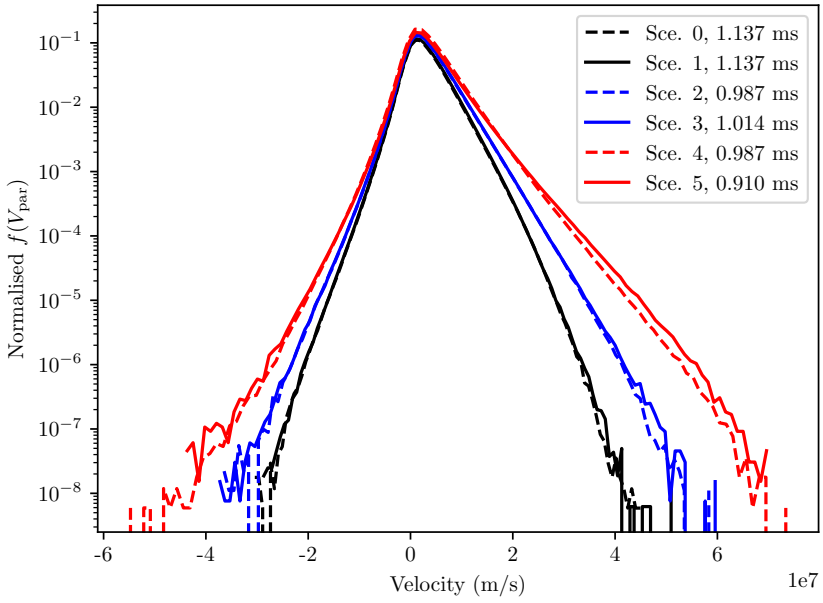

FIGURE 7.3: Normalised electron parallel velocity distribution $f(V_{\mathrm{par}})$ for all scenarios, taken at the final time step of respective simulations.

population) is shown in Fig. 7.3. The shown normalised distribution can be broadly categorised into 3 groups. The first group involves Sce. 0 and Sce. 1 which share identical $\langle L_{\mathrm{bt,\,seed}} \rangle$. This is followed by Sce. 2 and Sce. 3 which also have the same $\langle L_{\mathrm{bt,\,seed}} \rangle$. Finally, the last group consists of Sce. 4 and Sce. 5 which both have the octupole configuration as well as significantly longer $\langle L_{\mathrm{bt,\,seed}} \rangle$ measure.

It is plausible to represent the V_{par} distribution with a Gaussian function for Sce. 0 up to Sce. 3, but the last two scenarios have a more notable electron population with highly positive V_{par}. A Gaussian function may no longer be suitable for these cases. Regardless, the methodology explained in Sec. 6.3.4.1 still provides a good representation to all considered scenarios as well as providing a time extrapolation of the electron's parallel velocity distribution. An example of such fit to Sce. 6 data is shown in Fig. 7.4. The fitting parameters for respective scenarios are given in Tab. C.1 to C.6

The representation of the distribution via a fitted equation enables the calculation of the Full Width Half Maximum for V_{par} of each scenario. This value is computed via the gradient ascent method to find the maximum population, combined with the Newton's method to find the corresponding velocities at half maximum value. The results are tabulated in Tab. 7.8. This provides a straightforward measure of the spread of the electron population's parallel velocity magnitude, approximately 2/3 of the electron's

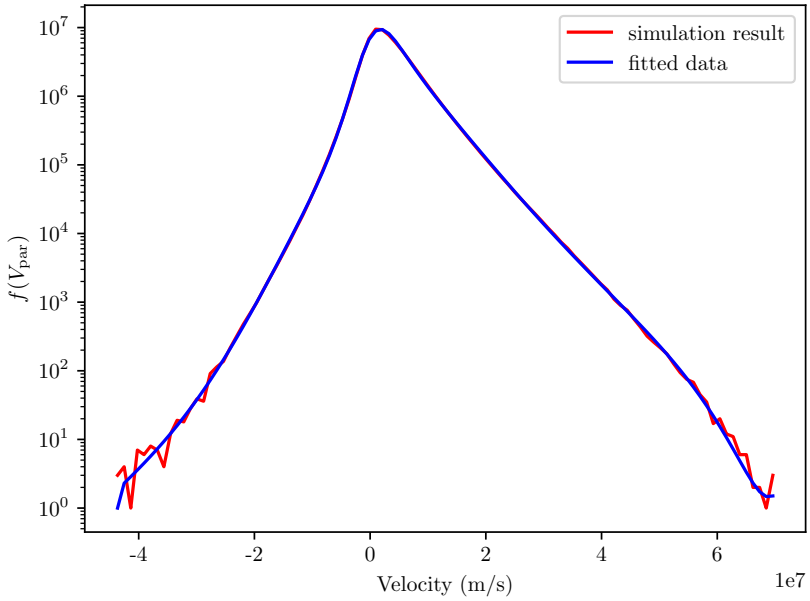

FIGURE 7.4: Electron V_{par} distribution for Sce. 5 at 0.91 ms.

total population falls within the measured width.

One can draw the conclusion that having a longer $\langle L_{bt,\,seed} \rangle$ results in a larger spread of the V_{par} distribution. This is a direct consequence of electrons having a longer confinement length, thus able to gain more energy before leaving the simulated domain. The widening of the negative velocity tail can be attributed to the electron-H_2 collisions. During elastic scatterings, electrons preserve the total kinetic energy before and after the scattering event while only altering its velocity vector. Thus, backscattering of highly energetic electrons adds to the long negative velocity tail. In the case of ionisation, the remaining energy is split purely between the incident and freed electrons. Since it was assumed in Eq. 3.18 that both the electrons is strictly forward scattered (relative to the incident electron's vector), this adds to the positive tail when coupled with continuous acceleration by $\mathbf{E}_\phi$.

As was previously discussed in Sec. 6.3.1.2, it is important to recall that the presented velocity distributions are obtained with a classical hard sphere model assumption when resolving the electron-neutral scattering angle. Changing the scattering angle model will impact the velocity distribution profile (as shown in Fig. 6.12) as well as the measured growth rates γ.

TABLE 7.8: FWHM for all scenarios.

	Sce. 0	Sce. 1	Sce. 2	Sce. 3	Sce. 4	Sce. 5
FWHM, $10^6\,\mathrm{m\,s^{-1}}$	6.03	5.83	6.41	6.42	6.68	6.58

7.3.1 Bimodal distribution fit of electrons' $f(V_{\mathbf{par}})$

Electron's parallel velocity distribution $f(V_{\mathrm{par}})$ for all scenarios were presented in Fig. 7.3, and the discussion that followed was focused on the accurate reproduction of the results via numerical fitting. However, the fitting has difficulties in providing intuitive physical interpretations. Therefore, this section focuses on further analysis in an attempt to rectify such difficulty.

For ease of analysis, the presented $f(V_{\mathrm{par}})$ are first rescaled into the unit of energy eV. A simplification is further introduced such that only the population of electrons which moves in the direction parallel to the direction of acceleration is considered. This originates from two specific considerations, the first is that the back-scattered electrons are considered as numerical artefacts (arising from the classical hard sphere model). The second is the additional consideration that the back-scattered electrons lose energy over time due to the background acceleration field vector opposing the direction of motion. The interest here is only on the portion of electrons that experience continuous energy gain over time. The corresponding distributions are shown in Fig. 7.5.

An assumption that the electron energy distribution consists of two distinct electron populations is made here. The first group describes the energetic electrons whose average kinetic energy is well above 1 keV, thus experiencing a significantly diminished probability of scattering with a neutral molecule and are able to freely accelerate. The other group describes electrons whose energies are below said energy threshold. By assuming that the energetic electrons are thermalised, their mean and standard deviation in energy can be found by fitting the distribution with a bimodal distribution function. Fig. 7.6 shows an example (Sce. 0) of the comparison between the results obtained from simulation and the numerically fitted bimodal distribution.

It is clear from Fig. 7.5 that the scenarios can once again be grouped into 3 distinct groups. As such, fitted Gaussian function parameters that represent the high energy tail of the distributions reflected such grouping as well (shown in Tab. 7.9). This is also proportional to the L_{bt} measures, which indicates that a better confinement property results in a longer acceleration duration for electrons before leaving the simulated domain. Thus, these conditions result in higher values of the mean energy for the energetic electron population.

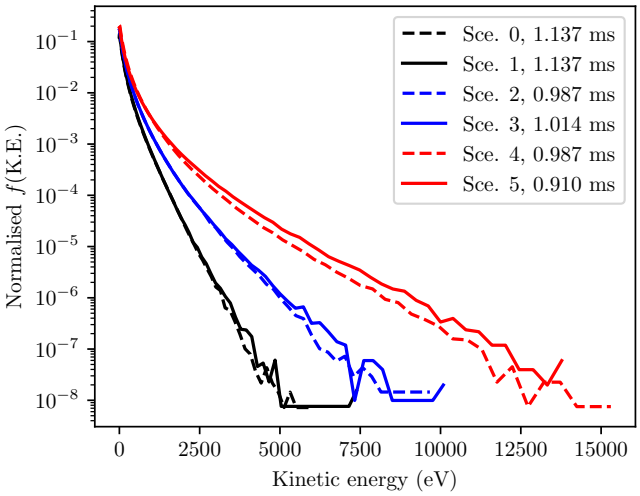

FIGURE 7.5: Normalised electron V_{par} distribution in kinetic energy scale for all scenarios at their respective simulation end time.

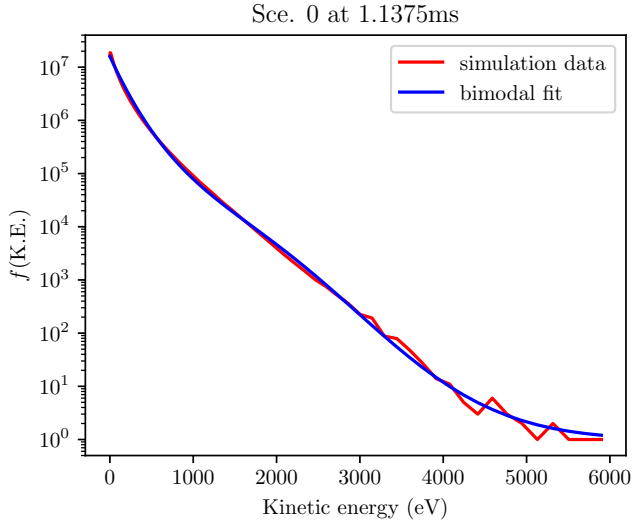

FIGURE 7.6: Electron V_{par} distribution in kinetic energy scale for Sce. 0 at 1.1375 ms, a bimodal distribution function is fitted to the simulation data.

TABLE 7.9: Gaussian function parameters for energetic electron group.

	Mean, keV	Standard deviation, keV
Sce. 0	1.9	1.5
Sce. 1	2.4	1.4
Sce. 2	3.3	2.2
Sce. 3	3.5	2.7
Sce. 4	4.3	4.3
Sce. 5	4.9	3.8

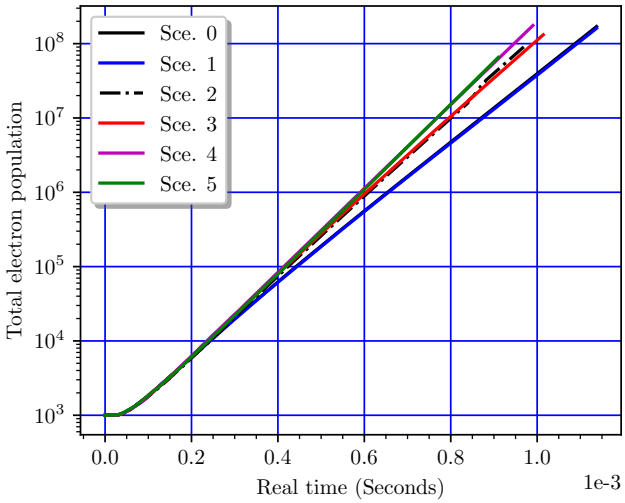

FIGURE 7.7: Total net electrons over time for all considered scenarios.

7.4 Numerically fitted γ coefficient

In every scenario, the growth constant $\gamma_{\text{sim.}}$ for both electron and ions are obtained via the described methodology in Sec. 6.3.2 and the results are tabulated in Tab. 7.10. The total net electron population over time for each scenario is shown in Fig. 7.7 to provide a visual reference to the obtained γ factors. It is observed that there are once again 3 distinct group of scenarios which gives near identical electron growth over time, namely the group of Sce. 0 and Sce. 1, Sce. 2 and Sce. 3, and finally the third group which includes Sce. 4 and Sce. 5. The respective plot for the total ion population over time is omitted as it is nearly identical to the electrons. Subsequently, Fig. 7.8 shows a plot of the $\gamma_{\text{e,sim.}}$ value with their respective $\langle L_{\text{bt, seed}} \rangle$ (a measure that was discussed in detail in Sec. 7.2).

At the first glance of Fig. 7.8, one might draw the conclusion that $\gamma_{\text{e,sim.}}$ tapers off after $\langle L_{\text{bt, seed}} \rangle$ reaches above $\sim$6 km. This might suggest that the L_{bt} has a limited

TABLE 7.10: Numerically fitted $\gamma_{\mathrm{e,sim.}}$ and $\gamma_{\mathrm{i,sim.}}$ for all scenarios.

	Sce. 0	Sce. 1	Sce. 2
$\gamma_{\mathrm{e,sim.}}$, s^{-1}	10 591.848(19)	10 529.070(54)	11 811.069(25)
$\gamma_{\mathrm{i,sim.}}$, s^{-1}	10 604.226(17)	10 536.928(22)	11 865.999(25)
	Sce. 3	Sce. 4	Sce. 5
$\gamma_{\mathrm{e,sim.}}$, s^{-1}	11 756.204(76)	12 912.475(52)	13 233.720(63)
$\gamma_{\mathrm{i,sim.}}$, s^{-1}	11 815.001(90)	12 966.321(48)	13 235.817(64)

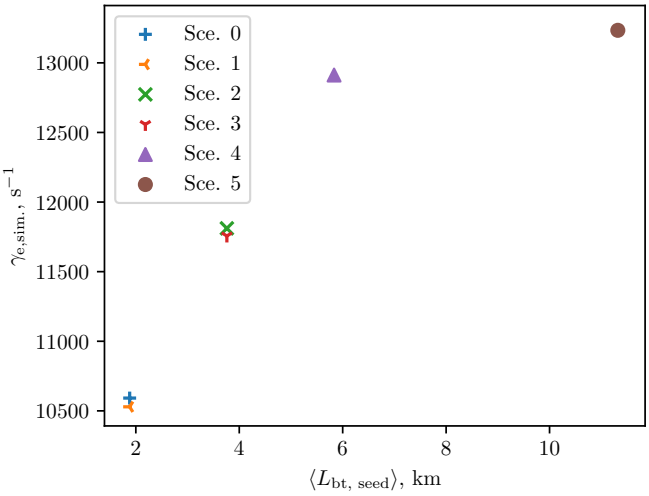

FIGURE 7.8: $\gamma_{\mathrm{e,sim.}}$ with its respective $\langle L_{\mathrm{bt,\ seed}} \rangle$ for all considered scenarios.

influence on $\gamma_{\mathrm{e,sim.}}$ beyond this point. However, caution is urged when interpreting the plot in Fig. 7.8, as Sce. 4 and Sce. 5 are simulations with the octupole field configuration. Direct comparison based solely on the $\langle L_{\mathrm{bt,\ seed}} \rangle$ measure could be misguided since the distribution of B_θ across the poloidal plane (subsequently L_{bt} map) is distinctly different from a quadrupole configuration. In order to make a conclusive statement on whether the $\gamma_{\mathrm{e,sim.}}$ saturates at high L_{bt} values, a future extended numerical study is suggested here. The study can be conducted with a series of simulations using the same quadrupole configuration while doubling the L_{bt} values for each subsequent simulation. Calculation and comparisons of the resulting $\gamma_{\mathrm{e,sim.}}$ should help show if it grows indefinitely as L_{bt} increases. As was alluded to earlier in Sce. 7.1, the annually allocated compute resources had already been depleted while obtaining the results in Tab. 7.10. Thus, the suggested numerical study could not be carried out.

TABLE 7.11: Computed $t_{\text{crit.}}$ and physical parameters related to the maximum predicted local electron number density n_{e} for all scenarios.

	Sce. 0	Sce. 1	Sce. 2
$t_{\text{crit.}}$, ms	2.75	2.73	2.07
Max. local n_{e}, m^{-3}	3.4439×10^{14}	2.4927×10^{14}	1.4364×10^{12}
ω_{pe}, $\text{rad}\,\text{s}^{-1}$	1.0469×10^{9}	8.9068×10^{8}	6.7614×10^{7}
λ_{D}, mm	3.97	4.68	66.73

	Sce. 3	Sce. 4	Sce. 5
$t_{\text{crit.}}$, ms	2.04	1.85	1.77
Max. local n_{e}, m^{-3}	1.1410×10^{12}	6.5655×10^{11}	3.2778×10^{11}
ω_{pe}, $\text{rad}\,\text{s}^{-1}$	6.0261×10^{7}	4.5712×10^{7}	3.2298×10^{7}
λ_{D}, mm	74.86	107.22	155.87

7.5 Prediction of $t_{\text{crit.}}$

The time when a closed magnetic flux surface is formed $t_{\text{crit.}}$ for the case of Sce. 0 had already been discussed in Sec. 6.3.4.2. The same steps are now applied to all the discussed scenarios. The resulting $t_{\text{crit.}}$ is tabulated in Tab. 7.11. The corresponding physical parameters related to the maximum local electron density n_{e} at respective $t_{\text{crit.}}$ are also calculated.

Making a direct comparison of the previously computed $\langle L_{\text{bt, seed}} \rangle$ and the results of $t_{\text{crit.}}$, it is clear to see that the measures are inversely proportional to each other. This is rather expected, since the longer backtraced connection length is an indication of a longer confined distance of charged particles. Thus, resulting in a higher local charged particle number density over time (subsequently higher current density). This creates a conducive environment for faster growth of self-consistent magnetic field $\mathbf{B}_{\text{int.}}$ magnitude.

The chosen simulation time step sizing for all considered scenarios is also shown to be sufficiently fine to properly capture the plasma frequencies of the charged particles system at $t_{\text{crit.}}$, since the electron gyrofrequency is orders of magnitude higher than other frequency measures.

7.6 0D L and $\langle L_{\text{bt, seed}} \rangle$ comparison

Both the connection length L_{0D} and $V_{\text{e,0D}}$ in the 0D ionisation fraction equation (Eq. 2.19) are shown to underestimate the results obtained from the present numerical simulations. However, there is still an interest in assessing the applicability of the 0D ionisation fraction model to a 3D setting.

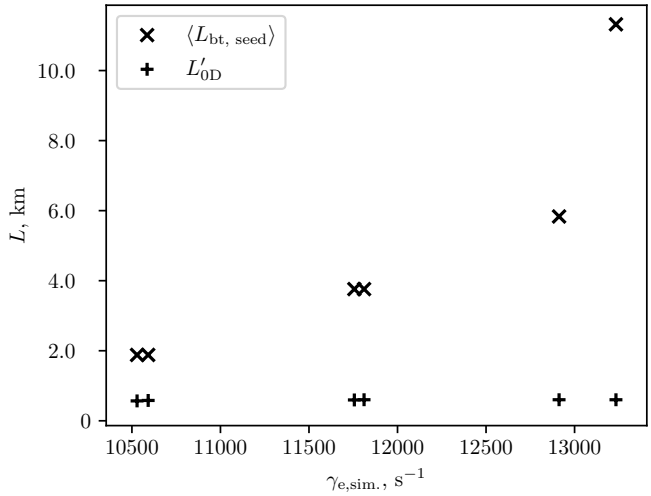

FIGURE 7.9: Comparison between $L'_{0\mathrm{D}}$ and $\langle L_{\mathrm{bt,\ seed}} \rangle$ for given V_{e} (Tab. 7.7) and $\gamma_{\mathrm{e,sim.}}$ (Tab. 7.10).

The idea is to assess whether the connection length $L'_{0\mathrm{D}}$ calculated from Eq. 2.19 (using the average electron drift velocity from the 3D simulation $V_{\mathrm{e,sim.}}$ and the fitted electron growth rate $\gamma_{\mathrm{e,sim.}}$) yields comparable trend as seen in L_{bt}. If $L'_{0\mathrm{D}}$ shows a similar trend compared to L_{bt}, a correction term added to the 0D equation could be proposed in order to adapt it to 3D scenarios. $L'_{0\mathrm{D}}$ is computed via

$$L'_{0\mathrm{D}} = \frac{V_{\mathrm{e,sim.}}}{\alpha V_{\mathrm{e,sim.}} - \gamma_{\mathrm{e,sim.}}}.$$

The results are plotted in comparison to $\langle L_{\mathrm{bt,\ seed}} \rangle$ as shown in Fig. 7.9. It is immediately clear that $\gamma_{\mathrm{e,sim.}}$ is proportional to $V_{\mathrm{e,sim.}}$ (Tab. 7.10 and Tab. 7.7), and this results in a near constant $L'_{0\mathrm{D}}$ value across differing values of $\gamma_{\mathrm{e,sim.}}$. This sufficiently informs us that simple corrections to Eq. 6.1 (subsequently Eq. 2.19) could not adapt the 0D model to a 3D setting, due to the stark difference. A new analytical model that sufficiently captures the ionisation fraction growth rate in 3D scenario is required.

7.7 Conclusion

Multiple variants of the background magnetic field ($\mathbf{B}_\theta$ and B_ϕ) configuration were simulated and various aspects of the simulation were analysed. Due to a numerical challenge preventing the full computation of the L_{bt} map for the whole poloidal plane, $\langle L_{\mathrm{bt,\ seed}} \rangle$ is introduced as the averaged minimum L_{bt} that initial electron population experiences.

L_{bt} depended purely on the external magnetic field $\mathbf{B}$, thus provide a link to the resulting $V_{\mathrm{e,sim.}}$, $\gamma_{\mathrm{e,sim.}}$ and $\gamma_{\mathrm{i,sim.}}$ observables.

It was found that $V_{\mathrm{e,sim.}}$, $\gamma_{\mathrm{e,sim.}}$ and $\gamma_{\mathrm{i,sim.}}$ are proportional to $\langle L_{\mathrm{bt,\,seed}} \rangle$, while $t_{\mathrm{crit.}}$ is inversely proportional. However, the effects on the growth rates ($\gamma_{\mathrm{e,sim.}}$ and $\gamma_{\mathrm{i,sim.}}$) are little, since they only increased by approximately 2 % while doubling $\langle L_{\mathrm{bt,\,seed}} \rangle$. Aside from that, the longer $\langle L_{\mathrm{bt,\,seed}} \rangle$ also broadens the electron V_{par} distribution. This is due to a longer connection length experienced by charged particles, allowing a longer duration of acceleration and gaining higher energies. The minimum time $t_{\mathrm{crit.}}$ when self-consistent magnetic field strength $\|\mathbf{B}_{\mathrm{int.}}\|$ becomes comparable to the background B_θ is also computed, demonstrating that magnetic field configurations that lengthen the L_{bt} will shorten $t_{\mathrm{crit.}}$. Lastly, it was found that the 0D model's calculated connection length L'_{0D} using numerically obtained $\gamma_{\mathrm{e,sim.}}$ does not compare well with the backtraced connection length L_{bt} (which is a good indicator of the charged particles' spatial distribution over time). The 0D model also consistently underestimates the V_{e}, as well as the growth rate of n_{e}.

As pointed out earlier, a full L_{bt} map in the poloidal plane is required to fully understand the impact of $\mathbf{B}_\theta$ and $\mathbf{B}_\phi$ on the overall charged particle growth rate as well as the resulting V_{e}. Two proposed directions of further investigation are suggested here to improve the presented findings. The first is a re-implementation of the streakline integral function that calculates L_{bt}, allowing the calculation to resume at later times. This would remove the cap on the L_{bt}, thus obtaining an accurate picture of the expected electron ionisation path length. Secondly, a further extension of the series of quadrupole field configuration simulation, reducing $\langle B_\theta \rangle$ by half (thus, increasing the measure of L_{bt}) at every subsequent simulation. This effectively doubles the overall L_{bt}, thus able to provide an insight into whether $\gamma_{\mathrm{sim.}}$ saturates and no longer rises when L_{bt} drastically increase.

Chapter 8

Summary and outlook

The creation of plasma medium from neutral prefill gas during the breakdown process is not well understood. This motivated the development of a first principles particle-based model, in an attempt to capture the time evolution of the electron growth rate and its velocity distribution. The influence of the prescribed 3D magnetic field geometry on the charged particle growth rate and spatial distribution is also a subject of study. The output of this research work can be categorised into three major areas. First among them is quantifying the resulting ionisation rate (represented by αV_e) from each considered scattering angle model and selecting the suitable model for tokamak plasma breakdown simulation. This is followed by an in-depth study on the influence of $\mathbf{B}_\phi$, $\mathbf{B}_\theta$ and $\mathbf{E}_\mathrm{int.}$ on the rate of ionisation as well as the charge and current density spatial distribution in an ITER-scale tokamak. Finally, an attempt to develop a new merging algorithm is done for a full 3D3V particle code to provide a way forward to simulate high number density systems (upward of $10^{10}\,\mathrm{m}^{-3}$). The following three sections provide summaries and outlooks for respective areas. This is then followed by a concluding remark to put the findings into context for ITER's eventual plasma initiation campaign.

8.1 Parallel plate experiment benchmark

The implemented particle-based model is tested in comparison with a parallel plate experiment. The goal of this exercise is to identify the scattering angle model that best approximates the first Townsend coefficient α and the resulting mean electron drift velocity V_DE. It was found that the Random Scatter model, which assumes a classical hard sphere collision model, provides the α measure that is closest to the reported values from D. J. Rose's work for $E/p \approx 300\,\mathrm{V\,m^{-1}\,Pa^{-1}}$. However, the obtained V_DE lies in the lower ranges of reported experimental values. The stated E/p ratio is important as it

corresponds to ITER's operating condition.

The isotropic elastic scatter angle distribution which originates from the classical hard sphere collision model is not physically correct. Switching to the Ohkrimovskyy model, which scatter angle distribution is derived from the first Born approximation, would yield a more physically correct description of electron-neutral scattering. However, Ohkrimovskyy's model has been shown to perform the worst in approximating the experimentally obtained α value. Probable future works would be to reexamine Ohkrimovskyy's derived scatter angle mode. Ohkrimovskyy's model was originally tested in simulations with larger nonpolar gases (for example, CH_4 and Ar), modification to the model for use in lighter nuclei can possibly yield better results.

8.2 ITER-like plasma initiation simulations

Variant simulations of Townsend avalanche breakdown in a 3 spatial dimensional torus, which incorporate prescribed 3D magnetic and electric fields were done. The model includes a tree code Coulomb potential solver in the computation of charged particle's electrostatic fields. The self-consistent magnetic field is excluded from the simulation as its strength is in the order of $10^{-13}\,\mathrm{T}$, at least 10 orders lower than the prescribed poloidal magnetic field. Prior to the tokamak simulations, a benchmark of the scattering angle models was done and the Random Scatter model was chosen due to its good approximation of the first Townsend's coefficient α and the resulting mean electron drift velocity V_{DE} in the $E/p \approx 300\,\mathrm{V\,m^{-1}\,Pa^{-1}}$ range, which is the operating condition of the ITER tokamak.

The simulation of plasma initiation in ITER-sized torus at $E/p \approx 300\,\mathrm{V\,m^{-1}\,Pa^{-1}}$ in Ch. 6 showed that the electron population growth rate $\gamma_{\mathrm{e,sim.}}$ is higher than the 0D ionisation fraction model γ_{0D} predicted. The 3D nature of the electron-neutral scattering is a major factor contributing to the discrepancy, which is also reflected in the higher mean electron drift velocity $V_{\mathrm{e,sim.}}$ compared to $V_{\mathrm{e,0D}}$. It was also found that the assumed connection length of $L_{\mathrm{0D}} = 1\,\mathrm{km}$ in the 0D model is an underestimation of the connection length near the magnetic null region. Another factor that increases the population growth rate is the averaged strength of poloidal magnetic stray field $\langle B_\theta \rangle$. It is observed that the depth of the magnetic null mattered less than the $\langle B_\theta \rangle$ measure, and the lower the $\langle B_\theta \rangle$, the better the growth rate is. At the same time, a larger toroidal magnetic field B_ϕ strength will contribute to better growth rate. Since there is an interplay between B_ϕ and B_θ in determining the overall growth rate, a single variable is defined to encapsulate the two variables into one. A proposed measure of backtraced

connection length L_{bt} summarises the influence of both B_ϕ and B_θ on ionisation rate, which a longer L_{bt} increases the rate and vice versa. It is also observed that the longer L_{bt} will cause a wider spread of the electron's velocity distribution $f(V)$ in the direction parallel to the torus' minor axis, as well as a higher mean electron drift velocity V_{e}. Extrapolation of the self-consistent magnetic field showed that the higher the value of L_{bt}, the shorter the time when it grows to be comparable in strength with the prescribed poloidal magnetic stray field.

Detailed simulation of the Townsend avalanche process during the early phase of plasma initiation had been done. However, one must be reminded that the electron velocity measures were obtained using the Random Scatter model. This approximates the electron-neutral scattering via a hard sphere collision model, which introduces excessive back-scattering due to its isotropic scatter angle distribution. More work is needed to replace the scattering model with a quantum mechanical description and thus improve upon the velocity distribution results discussed so far. This will also impact the obtained electron growth rates as a result of the altered mean electron drift velocity. Aside from that, the self-consistent magnetic field is not incorporated into the simulation itself, but rather obtained from post-processed results. It is a valid simplification up to the time scale of 1 ms, as the magnitude is approximately 10^{-13} T across all simulation variants. In order to progress further into the time scale of 2 ms and beyond, it is necessary to resolve the self-consistent magnetic field in order to capture the formation of closed magnetic flux surfaces.

8.3 Merging algorithm

The implementation of merging algorithm is done as a preparation for high charged number density scenarios found in later stages of the breakdown process. It is unfeasible to simulate and compute the electrostatic potential of 10^{12} electrons and above. Therefore, a merging algorithm that preserves the system's energy and momentum phase space is implemented. The algorithm is proven to be able to preserve the energy and momentum of the merging candidates at every merging instance. The global energy and momentum of the system are also conserved. However, introduction of electron-neutral scattering and ionisation into the merged super-particles produced unsatisfactory results, causing the approximation of the ionisation fraction to deviate from the unmerged case. This suggests that the scatterings/ionisations experienced by super-particles introduce additional alteration to the energy distribution over time. This is despite the fact that careful selection of the merging candidates ensures the preservation of the charged particles system's energy distribution.

Alternate scattering and ionisation models for super-particles need to be explored. The current model's artificial splitting of super-particles based on the collision outcomes could be the culprit behind the deviation. Another avenue of investigation is the influence of super-particles population. It is currently uncertain if the existing number of super-particles is abundant enough to offset the errors in ionisation rate. It may be that the low population of charged particles (approximately 4×10^7 total particles) invalidates the use of super-particles. Future benchmarks with a system that has a much higher charged particle number density can provide more insight into the applicability of the merging algorithm. Regardless, the continued development of the merging algorithm is necessary to push the simulation of plasma breakdown to a much longer time scale.

8.4 Remark on ITER's plasma initiation

The findings in Ch. 6 and Ch. 7 are obtained for an ITER-scale tokamak with the toroidal magnetic field strength B_ϕ of approximately 2.6 T. As was demonstrated in the comparison between Sce. 1 and Sce. 2 in Fig. 7.7, the electron population growth rate (indicative of the ionisation fraction growth rate) improves when B_ϕ is doubled. ITER's superconducting toroidal field coils are designed to reach a nominal peak field of 11.8 T [95]. Assuming that the pressure and the nominal loop voltage in ITER are comparable to the simulated cases, the initial ionisation growth rate during plasma initiation in ITER is expected to exceed the reported numbers in this study. The exponential growth of electron population in Fig. 7.7 shows no sign of slowing down and will likely sustain itself despite the constant electron losses. The internal electric field $\mathbf{E}_{\text{int.}}$ (seen in Fig. 6.17 and 6.25) which grows as the charge imbalance between electrons and ions rises will then assist in keeping the electrons confined (seen in Fig. 6.19). Optimistically, this shows that successful plasma initiation towards fusion ready plasma within ITER is possible.

Naturally, the simulations were done using a rather simplified representation of the actual magnetic field structures in ITER. All the metallic components of ITER (including those for the purposes of diagnostics, load-bearing support structures etc.) were excluded from the simulation. The current ramp-up phase during ITER's operation will induce additional stray fields not captured by the simulations. This will then affect the electron loss rates as well as the shape of the plasma column prior to the formation of closed magnetic flux surfaces. However, as long as the stray fields' strength remains in the order of mT (as done in the simulations), the simulated exponential growths of the ionisation fraction should remain relevant during the actual ITER operation.

Appendix A

Cross Sections

TABLE A.1: Vibrational excitation ($v = 0 \rightarrow 1$) cross section of electron-hydrogen molecule collision [4].

Energy(eV)	Cross Section (Å^2)	Energy(eV)	Cross Section (Å^2)
0.55	0.01	5.0	0.343
0.6	0.017	5.3	0.324
0.66	0.027	5.6	0.302
0.74	0.038	6.1	0.27
0.8	0.047	7.0	0.21
0.85	0.059	15.0	0.0565
1.0	0.094	20.0	0.0332
1.25	0.172	25.0	0.0242
1.48	0.24	30.0	0.017
2.0	0.367	40.0	0.0112
2.46	0.442	50.0	0.00968
3.0	0.486	60.0	0.00817
3.8	0.461	80.0	0.00609
4.6	0.38	100.0	0.00451

TABLE A.2: Total scattering cross section of electron-hydrogen molecule collision [4].

Energy(eV)	Cross Section (Å^2)	Energy(eV)	Cross Section (Å^2)
0.1	9.23	12.	9.61
0.12	9.47	15.	8.19
0.15	9.76	17.	7.46
0.17	9.93	20.	6.6
0.2	10.1	25.	5.61
0.25	10.5	30.	4.97
0.3	10.7	35.	4.54
0.35	11.	40.	4.19
0.4	11.2	45.	3.91
0.45	11.4	50.	3.68
0.5	11.6	60.	3.36
0.6	11.9	70.	3.06
0.7	12.3	80.	2.86
0.8	12.8	90.	2.68
0.9	13.2	100.	2.54
1.0	13.5	120.	2.25
1.2	14.2	150.	1.98
1.5	15.	170.	1.84
1.7	15.5	200.	1.66
2.	16.	250.	1.43
2.5	16.5	300.	1.24
3.	16.6	350.	1.11
3.5	16.6	400.	1.
4.	16.3	450.	0.914
4.5	15.9	500.	0.841
5.	15.4	600.	0.7
6.	14.4	700.	0.614
7.	13.3	800.	0.516
8.	12.4	900.	0.464
9.	11.6	1000.	0.422
10.	10.9		

TABLE A.3: Elastic scattering cross section of electron-hydrogen molecule collision [4].

Energy(eV)	Cross Section (Å^2)	Energy(eV)	Cross Section (Å^2)
0.02	7.41	2.0	14.11
0.03	7.71	3.0	14.12
0.04	8.08	4.0	13.2
0.05	8.32	5.0	12.51
0.06	8.51	6.0	11.45
0.07	8.69	8.0	9.85
0.08	8.84	10.0	8.58
0.09	8.99	12.0	7.61
0.1	9.13	14.0	6.92
0.12	9.33	16.0	6.32
0.15	9.55	18.0	5.78
0.2	9.83	20.0	5.26
0.25	10.04	25.0	4.23
0.3	10.24	30.0	3.40
0.4	10.61	35.0	2.81
0.5	10.95	40.0	2.36
0.6	11.28	50.0	1.73
0.7	11.59	60.0	1.31
0.8	11.88	70.0	1.06
0.9	12.16	80.0	0.89
1.0	12.36	90.0	0.81
1.25	13.00	100.0	0.74
1.5	13.55		

TABLE A.4: Rotational excitation ($J = 0 \rightarrow 2$) cross section of electron-hydrogen molecule collision [4].

Energy(eV)	Cross Section (Å^2)	Energy(eV)	Cross Section (Å^2)
0.0439	0.0	0.6	0.323
0.047	0.0185	0.7	0.394
0.05	0.027	0.8	0.469
0.055	0.035	0.9	0.555
0.06	0.042	1.0	0.638
0.065	0.048	1.2	0.796
0.07	0.053	1.5	1.036
0.08	0.062	2.0	1.37
0.09	0.068	2.5	1.585
0.1	0.074	3.0	1.704
0.11	0.079	3.5	1.755
0.13	0.088	4.0	1.758
0.15	0.097	4.5	1.732
0.2	0.115	5.0	1.689
0.25	0.132	6.0	1.579
0.3	0.152	7.0	1.462
0.35	0.175	8.0	1.35
0.4	0.2	9.0	1.248
0.45	0.228	10.0	1.156
0.5	0.26	15.0	0.73

TABLE A.5: Dissociative ionisation cross section of electron-hydrogen molecule collision [4].

Energy(eV)	Cross Section (Å^2)	Energy(eV)	Cross Section (Å^2)
30	0.0086	200	0.0545
35	0.0176	225	0.0505
40	0.0287	250	0.045
45	0.0408	275	0.0412
50	0.0482	300	0.0392
55	0.0572	350	0.0339
60	0.0625	400	0.0294
65	0.0682	450	0.026
70	0.0705	500	0.0241
75	0.0737	550	0.0211
80	0.0739	600	0.0197
85	0.0751	650	0.0181
90	0.0754	700	0.0171
95	0.0761	750	0.0159
100	0.0759	800	0.0149
110	0.0744	850	0.0137
120	0.0724	900	0.0135
140	0.0671	950	0.0125
160	0.0639	1000	0.0117
180	0.0592		

TABLE A.6: Nondissociative ionisation cross section of electron-hydrogen molecule collision [4].

Energy(eV)	Cross Section (Å^2)	Energy(eV)	Cross Section (Å^2)
16	0.0299	80	0.863
16.5	0.0607	85	0.853
17	0.0924	90	0.843
17.5	0.123	95	0.835
18	0.156	100	0.824
18.5	0.187	110	0.797
19	0.22	120	0.78
19.5	0.249	140	0.739
20	0.28	160	0.699
20.5	0.31	180	0.655
21	0.336	200	0.622
21.5	0.362	225	0.585
22	0.39	250	0.551
22.5	0.414	275	0.515
23	0.439	300	0.49
23.5	0.461	350	0.443
24	0.484	400	0.407
24.5	0.505	450	0.372
25	0.524	500	0.349
30	0.642	550	0.317
35	0.742	600	0.298
40	0.812	650	0.284
45	0.839	700	0.266
50	0.859	750	0.256
55	0.874	800	0.242
60	0.882	850	0.234
65	0.88	900	0.222
70	0.879	950	0.21
75	0.871	1000	0.199

Appendix B

Derivations

B.1 Current Density in a Circular Loop

Since the current is restricted to flow in a circular loop, current density is then

$$\mathbf{J} = J_\phi \hat{\boldsymbol{\phi}}.$$

The loop's radius is predefined as R and it is in plane with the origin (which lies on x-y plane). These conditions are expressed by $\delta(r' - R)$ and $\delta(\theta' - \pi/2)$. Since $\theta' = [0, \pi]$, this leads to

$$\delta(\theta' - \pi/2) = \delta(\cos\theta')$$

where only $\theta' = \pi/2$ is allowed.

Hence, J_ϕ can now be expressed as

$$J_\phi = \lambda \sin\theta' \; \delta(\cos\theta') \; \delta(r' - R).$$

Before proceeding with the next step, it is important to recognise that since the current travels only within the loop,

$$\int_0^\infty \int_0^{2\pi} \int_0^\pi \mathbf{J} r'^2 \sin\theta' \; \mathrm{d}\theta' \; \mathrm{d}\phi' \; \mathrm{d}r' = \int_C I\mathbf{dl}$$

holds and the current magnitude is conserved. **dl** refers to a vector that is always tangent to the circular loop. Substituting the expression of J_ϕ and evaluating the integral

$$\begin{aligned}
\int_C I\mathbf{dl} &= \int_0^{\infty}\int_0^{2\pi}\int_0^{\pi} \lambda \sin\theta' \ \delta(\cos\theta') \ \delta(r'-R) r'^2 \sin\theta' \ \mathrm{d}\theta' \ \mathrm{d}\phi' \ \mathrm{d}r' \\
\int_C I\mathbf{dl} &= \int_0^{2\pi} \lambda R^2 \mathrm{d}\phi' \\
\int_0^{2\pi} IR\mathrm{d}\phi' &= 2\pi R^2\lambda \\
2\pi IR &= 2\pi R^2\lambda \\
\lambda &= \frac{I}{R}
\end{aligned}$$

The complete expression of J_ϕ is then

$$J_\phi = \frac{I}{R}\sin\theta' \ \delta(\cos\theta') \ \delta(r'-R).$$

B.2 Expressing Vector Potential in Complete Elliptic Integral of 1st & 2nd Kind

The expression for complete elliptic integral of the first kind is

$$K(k) = \int_0^{\frac{\pi}{2}} \frac{\mathrm{d}\gamma}{\sqrt{1-k^2\sin^2\gamma}}.$$

The expression for complete elliptic integral of the second kind is

$$E(k) = \int_0^{\frac{\pi}{2}} \sqrt{1-k^2\sin^2\gamma} \ \ \mathrm{d}\gamma$$

Hence it is prudent to transform the variable $\phi' = [0, 2\pi]$ into γ variable that is in the range of $[-\pi/2, \pi/2]$. It then follows

$$\phi' = \pi - 2\gamma.$$

Subsequently,

$$\cos\phi' = 2\sin^2\gamma - 1 \quad \text{and} \quad \mathrm{d}\phi' = -2\mathrm{d}\gamma.$$

Starting from Eq. 3.31,

$$
\begin{aligned}
A_\phi(r,\theta) &= \frac{\mu_0 I R}{4\pi}\int_0^{2\pi}\frac{\cos\phi'}{\sqrt{r^2+R^2-2rR\sin\theta\cos\phi'}}\,\mathrm{d}\phi' \\
&= \frac{\mu_0 I R}{4\pi}\int_{\frac{\pi}{2}}^{-\frac{\pi}{2}}\frac{2-4\sin^2\gamma}{\sqrt{r^2+R^2-2rR\sin\theta(2\sin^2\gamma-1)}}\mathrm{d}\gamma \\
&= \frac{\mu_0 I R}{2\pi}\int_{\frac{\pi}{2}}^{-\frac{\pi}{2}}\frac{1-2\sin^2\gamma}{\sqrt{r^2+R^2-4rR\sin\theta\sin^2\gamma+2rR\sin\theta}}\mathrm{d}\gamma \\
&= \frac{\mu_0 I R}{2\pi}\frac{1}{\sqrt{r^2+R^2+2rR\sin\theta}}\int_{\frac{\pi}{2}}^{-\frac{\pi}{2}}\frac{1-2\sin^2\gamma}{\sqrt{1-\frac{4rR\sin\theta\sin^2\gamma}{r^2+R^2+2rR\sin\theta}}}\mathrm{d}\gamma \\
&= C(\theta)\int_{\frac{\pi}{2}}^{-\frac{\pi}{2}}\frac{1-2\sin^2\gamma}{\sqrt{1-\frac{4rR\sin\theta\sin^2\gamma}{r^2+R^2+2rR\sin\theta}}}\mathrm{d}\gamma;\ C(\theta)=\frac{\mu_0 I R}{2\pi}\frac{1}{\sqrt{r^2+R^2+2rR\sin\theta}} \\
&= C(\theta)\int_{\frac{\pi}{2}}^{-\frac{\pi}{2}}\frac{1-2\sin^2\gamma}{\sqrt{1-k^2\sin^2\gamma}}\mathrm{d}\gamma;\ k^2=\frac{4rR\sin\theta}{R^2+r^2+2rR\sin\theta} \\
&= C(\theta)\int_{-\frac{\pi}{2}}^{\frac{\pi}{2}}\frac{2\sin^2\gamma-1}{\sqrt{1-k^2\sin^2\gamma}}\mathrm{d}\gamma \\
&= 2C(\theta)\int_0^{\frac{\pi}{2}}\frac{2\sin^2\gamma-1}{\sqrt{1-k^2\sin^2\gamma}}\mathrm{d}\gamma \\
&= 2C(\theta)\left(\int_0^{\frac{\pi}{2}}\frac{2\sin^2\gamma}{\sqrt{1-k^2\sin^2\gamma}}\mathrm{d}\gamma - K(k)\right) \\
&= 2C(\theta)\left(\frac{2}{k^2}\int_0^{\frac{\pi}{2}}\frac{k^2\sin^2\gamma}{\sqrt{1-k^2\sin^2\gamma}}\mathrm{d}\gamma - K(k)\right) \\
&= 2C(\theta)\left(\frac{2}{k^2}\Big(\int_0^{\frac{\pi}{2}}\frac{1}{\sqrt{1-k^2\sin^2\gamma}}\mathrm{d}\gamma - \int_0^{\frac{\pi}{2}}\frac{1-k^2\sin^2\gamma}{\sqrt{1-k^2\sin^2\gamma}}\mathrm{d}\gamma\Big) - K(k)\right) \\
&= 2C(\theta)\left(\frac{2}{k^2}\Big(K(k)-E(k)\Big) - K(k)\right) \\
&= \frac{\mu_0 I R}{\pi}\frac{1}{\sqrt{r^2+R^2+2rR\sin\theta}}\left(\frac{2}{k^2}\Big(K(k)-E(k)\Big) - K(k)\right)
\end{aligned}
$$

Appendix C

Numerical Fit Coefficients

C.1 $V_{\parallel}$ distributions

TABLE C.1: Fit parameters to reconstruct Sce. 0 electron $V_{\parallel}$ distribution at $t = 1.1375\,\mathrm{ms}$.

c_0	-1.87662460e+01	d_1	-9.63739644e+00
c_1	1.99571755e+02	d_2	5.98349954e+00
c_2	-2.32624103e+02	d_3	-9.72059062e-01
c_3	1.02000897e+02	d_4	-9.36906534e-02
c_4	-1.96568263e+01	d_5	3.74309256e-02
c_5	1.38798155e+00	d_6	-3.13912751e-03
$V_{\parallel,\,\mathrm{min}}$	$-3.044 \times 10^7\,\mathrm{m\,s^{-1}}$	$V_{\parallel,\,\mathrm{max}}$	$4.555 \times 10^7\,\mathrm{m\,s^{-1}}$
N_e	169708704		

TABLE C.2: Fit parameters to reconstruct Sce. 1 electron $V_{\parallel}$ distribution at $t = 1.1375\,\mathrm{ms}$.

c_0	-1.66961859e+01	d_1	1.56360320e+03
c_1	-2.73821291e+04	d_2	-1.68299949e+03
c_2	4.69093293e+04	d_3	7.02533218e+02
c_3	-3.15585329e+04	d_4	-1.36081179e+02
c_4	1.07617619e+04	d_5	8.60760931e+00
c_5	-1.96014800e+03	d_6	1.35671039e+00
c_6	1.81189413e+02	d_7	-2.79407048e-01
c_7	-6.68008773e+00	d_8	1.44924052e-02
$V_{\parallel,\,\mathrm{min}}$	$-2.868 \times 10^7\,\mathrm{m\,s^{-1}}$	$V_{\parallel,\,\mathrm{max}}$	$5.095 \times 10^7\,\mathrm{m\,s^{-1}}$
N_e	160741535		

TABLE C.3: Fit parameters to reconstruct Sce. 2 electron V_{par} distribution at $t = 0.987\,\mathrm{ms}$.

c_0	-1.69339300e+01	d_1	-3.17026032e+05
c_1	6.10351832e+06	d_2	1.39769196e+06
c_2	-2.85328074e+07	d_3	-1.19755359e+06
c_3	2.94192916e+07	d_4	5.19132328e+05
c_4	-1.30633035e+07	d_5	-1.38156021e+05
c_5	2.86814068e+06	d_6	2.21106324e+04
c_6	-2.99262219e+05	d_7	-1.80865097e+03
c_7	1.15889190e+04	d_8	5.70983165e+01
$V_{\mathrm{par,\,min}}$	$-3.643 \times 10^7\,\mathrm{m\,s^{-1}}$	$V_{\mathrm{par,\,max}}$	$5.831 \times 10^7\,\mathrm{m\,s^{-1}}$
N_{e}	90441558		

TABLE C.4: Fit parameters to reconstruct Sce. 3 electron V_{par} distribution at $t = 1.014\,\mathrm{ms}$.

c_0	-1.73092738e+01	d_1	4.32889722e+03
c_1	-8.33342338e+04	d_2	-3.90296058e+03
c_2	9.97318004e+04	d_3	1.57793785e+03
c_3	-4.59793642e+04	d_4	-3.77061519e+02
c_4	1.01906127e+04	d_5	5.43927138e+01
c_5	-1.06800729e+03	d_6	-4.00480888e+00
c_6	4.18363030e+01	d_7	1.10202887e-01
$V_{\mathrm{par,\,min}}$	$-3.726 \times 10^7\,\mathrm{m\,s^{-1}}$	$V_{\mathrm{par,\,max}}$	$5.956 \times 10^7\,\mathrm{m\,s^{-1}}$
N_{e}	131603446		

TABLE C.5: Fit parameters to reconstruct Sce. 4 electron V_{par} distribution at $t = 0.987\,\mathrm{ms}$.

c_0	-1.89403331e+01	d_1	3.02151891e+02
c_1	-5.82025402e+03	d_2	-2.14466171e+03
c_2	4.16197848e+04	d_3	5.42923583e+03
c_3	-1.06539714e+05	d_4	-6.53625185e+03
c_4	1.30101455e+05	d_5	4.13968892e+03
c_5	-8.33612016e+04	d_6	-1.44759733e+03
c_6	2.87598572e+04	d_7	2.97211982e+02
c_7	-5.36150811e+03	d_8	-3.58894685e+01
c_8	5.07297989e+02	d_9	2.29972420e+00
c_9	-1.89552631e+01	d_{10}	-5.48247689e-02
$V_{\mathrm{par,\,min}}$	$-5.474 \times 10^7\,\mathrm{m\,s^{-1}}$	$V_{\mathrm{par,\,max}}$	$7.337 \times 10^7\,\mathrm{m\,s^{-1}}$
N_{e}	168470572		

TABLE C.6: Fit parameters to reconstruct Sce. 5 electron V_{par} distribution at $t = 0.91\,\mathrm{ms}$.

c_0	-1.61146858e+01	d_1	-7.91744026e-01
c_1	1.49079451e+01	d_2	2.74321710e-01
c_2	-5.06550011e+00	d_3	-5.17478716e-02
c_3	7.49167227e-01	d_4	4.97953656e-03
c_4	-3.99691944e-02	d_5	-1.62070559e-04
$V_{\mathrm{par,\,min}}$	$-4.365 \times 10^7\,\mathrm{m\,s^{-1}}$	$V_{\mathrm{par,\,max}}$	$6.960 \times 10^7\,\mathrm{m\,s^{-1}}$
N_{e}	65326685		

Appendix D

Curriculum Vitae

Education

2018–2022 **PhD study in progress**, *Ruhr-Universität Bochum*, Germany, *(Thesis in progress, tentative submission in December 2022).*

Thesis *3D first-principles simulation of plasma initiation in ITER-like tokamak.*

Supervisors Prof. Dr. Paul Gibbon, Dr. Dirk Brömmel, Prof. Dr. Bernhard Unterberg, Prof. Dr. Rainer Grauer

2015–2018 **Masters in Simulation Sciences**, *Rheinisch-Westfälische Technische Hochschule Aachen*, Germany, *Overall Grade – 1.6 (grade ranges from 1.0 - 4.0, highest to lowest).*

Thesis *Numerical modelling of the early phase of plasma breakdown in JET-like tokamak.*

Supervisors Prof. Dr. Paul Gibbon, Dr. Dirk Brömmel

2008–2012 **Bachelor of Aerospace Engineering**, *University Putra Malaysia*, Serdang, *GPA – 3.866 (grade ranges from 4.0 - 1.0, highest to lowest).*

Thesis *Study of Magnetohydrodynamics flow in Combined Attitude and Thermal Control System (CATCS) for Satellites.*

Supervisor Professor Renuganth Varatharajoo

Academic Conferences/Summer School

2021 **47th Conference on Plasma Physics**, *online conference.*

2021 **ISC High Performance 2021**, *online conference.*

2019 **The Scalasca Scalable Parallel Performance Analysis Toolset – for POP assessments and beyond**, *Webinar - JSC*, Forschungszentrum Jülich.

2019 **GPU Programming - JSC Guest Student Programme**, *JSC*, Forschungszentrum Jülich.

2018 **55th Culham Plasma Physics Summer School**, *Culham Science Centre*, Oxford.

Publications

- Chew, J., Gibbon, P., Brömmel, D., de Vries, P. & Gribov, Y. (2021). First principles 3D simulation of tokamak plasma breakdown. *Plasma Physics. EPS Conference. 47th 2021. (EPS 2021)*, 141-144
- Chew, J., Gibbon, P., Brömmel, D., Wauters T., Gribov Y., de Vries, P (2021). Three-dimensional first principles simulation of a hydrogen discharge. *Plasma Physics and Controlled Fusion*, 63(4), 045012.
- Romli, F., Kian, H. C., Chew, J. & Rafie, A. (2011). Subsystem Change Ranking Methodology (SCRaM) for Complex Product Redesign Process. *Advanced Materials Research*, 308, 167-173.

Talks/Presentations

- Oral contribution in 47th EPS Conference on Plasma Physics, *First principles 3D simulation of tokamak plasma breakdown.*
- *Numerical Modelling of the Electron-Hydrogen Molecule Impact Ionisation in Tokamak*,

Remote Collaborative Seminar with ITER Science Division, 2020.

- Poster Presentation of *Simulation of MHD fluid in Combined Attitude and Thermal Control System (CATCS)*, Department of Aerospace Engineering, University Putra Malaysia, 2012.

Work Experience

Oct, 2018 - present **Scientific staff**, *SimLab Plasma Physics*, Jülich Supercomputing Centre (JSC), FZJ.

Completed tasks:

- Implemented parallel calculation of external electric and magnetic fields in a tokamak geometry.
- Implementation of charge and current density interpolation onto uniform grid, similar to Particle-in-Cell methods diagnostic purposes.
- Charge and current density interpolation onto unstructured grid for better approximation of simulated domain.
- Profiling the computational costs of the code's various components to improve compute efficiency.
- Derivation and implementation of a particle merging algorithm to reduce computational cost.
- Writing and submission of annual JARA-HPC/VSR proposal.
- Conduct large scale simulations for avalanche breakdown ionisation in tokamak scenarios, on both JURECA DC (> 40 nodes) and booster module (> 120 nodes).

Oct, 2017 - Sept, 2018 **Academic Assistant(HiWi)**, *SimLab Plasma Physics*, Jülich Supercomputing Centre (JSC), FZJ.

Completed tasks:

- Programming a new parallelised frontend code that supports new particle injection or ionisation instances.
- Integration of existing meshless Pretty Efficient Parallel Coulomb (PEPC) solver into said frontend.
- Integration of the highly parallelisable Random123 RNG library into the fronted, interfacing C in Fortran.
- Implementation of an explicit particle motion integrator.
- Implemented Monte-Carlo simulations for electron-neutral impact ionisation simulations.

Feb, 2016 - April, 2017 **Academic Assistant(HiWi)**, *Institute of Aerodynamics*, RWTH Aachen.

Assigned tasks:

- Debug & implement subroutines which assist with Lattice-Boltzmann portion of in-house C++ solver code (Zonal-Flow-Solver, ZFS).
- Implementation of various boundary condition for cell lattice configurations in MPI parallel environment.
- Identify/compute simulation input parameters and run simulations, along with results post-processing.

Sept, 2012 - Sept, 2015 **Applications Engineer**, *Drawbridge Technologies (M) Private Limited*, Malaysia.

Assigned tasks:

- Provide technical support to customers using Autodesk Simulation CFD and Simulation Mechanical products
- Perform technical demonstration to potential customers in regards to Simulation Mechanical & CFD's capabilities
- Simulation applications problem solving and fulfilling client's simulation requests.

Bibliography

[1] IAEA Nuclear Data Services. https://www-nds.iaea.org/. Accessed: 28-11-2022.

[2] V. Vahedi and M. Surendra. A Monte Carlo Collision Model for the Particle-in-Cell Method: Applications to Argon and Oxygen Discharges. *Computer Physics Communications*, 87(1):179 – 198, 1995. Particle Simulation Methods.

[3] A. Okhrimovskyy, A. Bogaerts, and R. Gijbels. Electron anisotropic scattering in gases: A formula for monte carlo simulations. *Phys. Rev. E*, 65:037402, Feb 2002.

[4] J. S. Yoon, M. Y. Song, J. M. Han, S. H. Hwang, W. S. Chang, B. J. Lee, and Y. Itikawa. Cross Sections for Electron Collisions with Hydrogen Molecules. *Journal of Physical and Chemical Reference Data*, 37(2):913–931, 2008.

[5] H. T. Saelee and J. Lucas. Simulation of electron swarm motion in hydrogen and carbon monoxide for high E/N. *Journal of Physics D: Applied Physics*, 10(3):343–354, feb 1977.

[6] H. Schlumbohm. Stoßionisierungskoeffizient α, mittlere elektronenenergien und die beweglichkeit von elektronen in gasen. *Zeitschrift für Physik*, 184(5):492–505, oct 1965.

[7] V. A. Lisovskiy and V. D. Yegorenkov. Rf breakdown of low-pressure gas and a novel method for determination of electron-drift velocities in gases. *Journal of Physics D: Applied Physics*, 31(23):3349–3357, dec 1998.

[8] H. A. Blevin, J. Fletcher, and S. R. Hunter. The electron drift velocity and longitudinal diffusion coefficient of an electron swarm in hydrogen at elevated swarm energies. *Journal of Physics D: Applied Physics*, 9(12):1671–1679, aug 1976.

[9] W. Roznerski and K. Leja. Electron drift velocity in hydrogen, nitrogen, oxygen, carbon monoxide, carbon dioxide and air at moderate e/n. *Journal of Physics D: Applied Physics*, 17(2):279–285, feb 1984.

[10] World Energy & Climate Statistics - Yearbook 2022. https://yearbook.enerdata.net/total-energy/world-consumption-statistics.html. Accessed: 28-11-2022.

[11] Record clean energy spending is set to help global energy investment grow by 8% in 2022. https://www.iea.org/news. Accessed: 28-11-2022.

[12] The global fusion industry in 2022. https://www.fusionindustryassociation.org/copy-of-about-the-fusion-industry. Accessed: 28-11-2022.

[13] X. Gao, Y. Yang, T. Zhang, H. Liu, G. Li, T. Ming, Z. Liu, Y. Wang, L. Zeng, X. Han, Y. Liu, M. Wu, H. Qu, B. Shen, Q. Zang, Y. Yu, D. Kong, W. Gao, L. Zhang, H. Cai, X. Wu, K. Hanada, F. Zhong, Y. Liang, C. Hu, F. Liu, X. Gong, B. Xiao, B. Wan, X. Zhang, J. Li, and the EAST Team. Key issues for long-pulse high-βN operation with the experimental advanced superconducting tokamak (east). *Nuclear Fusion*, 57(5):056021, mar 2017.

[14] G. Sinclair, S. Gonderman, J.K. Tripathi, and A. Hassanein. Effect of elm pacing on morphology evolution and erosion of tungsten as a plasma-facing material in a fusion environment. *Journal of Nuclear Materials*, 508:26–32, 2018.

[15] S. Wang, J. Li, Y. Wang, X. Zhang, R. Wang, Y. Wang, and J. Cao. Thermal damage of tungsten-armored plasma-facing components under high heat flux loads. *Scientific Reports*, 10, 2020.

[16] H. T. Kim. *Physics and Computational Simulations of Plasma Burn-through for Tokamak Start-up*. PhD thesis, Imperial College London, 2013.

[17] D. Mueller. The Physics of Tokamak Start-Up. *Physics of Plasmas*, 20(5):058101, 2013.

[18] P. C. de Vries and Y. Gribov. ITER breakdown and plasma initiation revisited. *Nuclear Fusion*, 59(9):096043, aug 2019.

[19] K. Brodén, R. Edwards, M. Lindberg, P. Rocco, and M. Zucchetti. Waste from fusion reactor: A comparison with other energy producing systems. *Fusion Engineering and Design*, 42(1):1–6, 1998.

[20] M. Zucchetti, L. Candido, V. Khripunov, B. Kolbasov, and R. Testoni. Fusion power plants, fission and conventional power plants. radioactivity, radiotoxicity, radioactive waste. *Fusion Engineering and Design*, 136:1529–1533, 2018. Special Issue: Proceedings of the 13th International Symposium on Fusion Nuclear Technology (ISFNT-13).

[21] *ITER Poloidal Field System.* Number 27 in ITER Documentation Series. International Atomic Energy Agency, Vienna.

[22] M. J. Singh, D. Boilson, A. R. Polevoi, T. Oikawa, and R. Mitteau. Heating neutral beams for iter: negative ion sources to tune fusion plasmas. *New Journal of Physics*, 19(5):055004, may 2017.

[23] K. Ikeda, K. Tsumori, M. Kisaki, H. Nakano, K. Nagaoka, M. Osakabe, S. Kamio, Y. Fujiwara, Y. Haba, and Y. Takeiri. First results of deuterium beam operation on neutral beam injectors in the large helical device. *AIP Conference Proceedings*, 2011(1):060002, 2018.

[24] D. Van Eester and E. Lerche. Kinetic theory of plasma waves. *Fusion Science and Technology*, 61(2T):331–346, 2012.

[25] J. Wesson and D. J. Campbell. *Tokamaks (4th ed.).* Oxford University Press, 2011.

[26] Y. Sarazin, J. Hillairet, J.-L. Duchateau, K. Gaudimont, R. Varennes, X. Garbet, Ph. Ghendrih, R. Guirlet, B. Pégourié, and A. Torre. Impact of scaling laws on tokamak reactor dimensioning. *Nuclear Fusion*, 60(1):016010, oct 2019.

[27] F. Troyon, R. Gruber, H. Saurenmann, S. Semenzato, and S. Succi. MHD-Limits to Plasma Confinement. *Plasma Physics and Controlled Fusion*, 26(1A):209, jan 1984.

[28] F. Troyon, A. Roy, W. A. Cooper, F. Yasseen, and A. Turnbull. Beta limit in tokamaks. experimental and computational status. *Plasma Physics and Controlled Fusion*, 30(11):1597, oct 1988.

[29] P. K. Kaw, R. M. Kulsrud, and S. C. Cowley. Equilibrium poloidal beta limit in tokamaks. In *Research Using Small Tokamaks*, volume 20, pages 67–70. International Atomic Energy Agency (IAEA), 1989.

[30] M. S. Chu and M. Okabayashi. Stabilization of the external kink and the resistive wall mode. *Plasma Physics and Controlled Fusion*, 52(12):123001, oct 2010.

[31] P. Piovesan, J. M. Hanson, P. Martin, G. A. Navratil, F. Turco, J. Bialek, N. M. Ferraro, R. J. La Haye, M. J. Lanctot, M. Okabayashi, C. Paz-Soldan, E. J. Strait, A. D. Turnbull, P. Zanca, M. Baruzzo, T. Bolzonella, A. W. Hyatt, G. L. Jackson, L. Marrelli, L. Piron, and D. Shiraki. Tokamak Operation with Safety Factor $q_{95}lt;2$ via Control of MHD Stability. *Phys. Rev. Lett.*, 113:045003, jul 2014.

[32] F. Perkins, P. Barabaschi, and D. Boucher. *ITER physics basis.* IAEA, 1995.

[33] H. Zohm. On the Minimum Size of DEMO. *Fusion Science and Technology*, 58(2):613–624, 2010.

[34] H. Zohm. On the size of tokamak fusion power plants. *Phil. Trans. R. Soc. A.*, 377(20170437), 2019.

[35] D. R. Cohn and L. Bromberg. Advantages of high-field tokamak for fusion reactor development. *J. Fusion Energy; (United States)*, 5:3, sep 1986.

[36] W. Jiang, Y. Peng, Y. Zhang, and G. Lapenta. Numerical modeling of tokamak breakdown phase driven by pure Ohmic heating under ideal conditions. *Nuclear Fusion*, 56(12):126017, sep 2016.

[37] J. Bucalossi, P. Hertout, M. Lennholm, F. Saint-Laurent, F. Bouquey, C. Darbos, E. Traisnel, and E. Trier. First experiments of plasma start-up assisted by ECRH on Tore Supra. *Nuclear Fusion*, 48(5):054005, apr 2008.

[38] Y. S. Bae, J. H. Jeong, S. I. Park, M. H. Cho, W. Namkung, G. L. Jackson, M. Joung, S. W. Yoon, J. H. Kim, S. H. Hahn, W. C. Kim, H. L. Yang, Y. K. Oh, D. Humphreys, M. L. Walker, Y. Gorelov, J. A. Leuer, A. W. Hyatt, N. W. Eidietis, D. Mueller, J. S. Bak, and M. Kwon. ECH-assisted startup at KSTAR. *AIP Conference Proceedings*, 1187(1):495–502, 2009.

[39] Sir Townsend, John. *The Theory of Ionization of Gases by Collision.* London :Constable, 1910. https://www.biodiversitylibrary.org/bibliography/22810 — Continued by: Landmarks II. — Master microform held by: Readex.

[40] R. Papoular. The genesis of toroidal discharges. *Nuclear Fusion*, 16(1):37, feb 1976.

[41] B. Lloyd, G.L. Jackson, T.S. Taylor, E.A. Lazarus, T.C. Luce, and R. Prater. Low voltage Ohmic and electron cyclotron heating assisted startup in DIII-D. *Nuclear Fusion*, 31(11):2031, nov 1991.

[42] P.C. de Vries, A.C.C. Sips, H.T. Kim, P.J. Lomas, F. Maviglia, R. Albanese, I. Coffey, E. Joffrin, M. Lehnen, A. Manzanares, M. O'Mulane, I. Nunes, G. van Rooij, F.G. Rimini, M.F. Stamp, and JET-EFDA Contributors. Characterisation of plasma breakdown at JET with a carbon and ITER-like wall. *Nuclear Fusion*, 53(5):053003, apr 2013.

[43] V. A. Belyakov, K. M. Lobanov, L. P. Makarova, A. B. Mineev, and V. I. Vasiliev. Plasma initiation stage analysis in tokamaks with transmak code. *Plasma Devices and Operations*, 11(3):193–201, 2003.

[44] M. G. Yoo, J. Lee, Y. G. Kim, and Y. S. Na. Development of 2D implicit particle simulation code for ohmic breakdown physics in a tokamak. *Computer Physics Communications*, 221:143–159, 2017.

[45] M. G. Yoo, J. Lee, Y. G. Kim, J. Kim, F. Maviglia, A. C. C. Sips, H. T. Kim, T. S. Hahm, Y. S. Hwang, H. J. Lee, and Y. S. Na. Evidence of a turbulent exb mixing avalanche mechanism of gas breakdown in strongly magnetized systems. *Nature Communications*, 9, 2018.

[46] M. Hoppe, I. Ekmark, E. Berger, and T. Fülöp. Runaway electron generation during tokamak start-up. *Journal of Plasma Physics*, 88(3):905880317, 2022.

[47] O. Schmitz, T. E. Evans, M.E. Fenstermacher, A. McLean, J. Boedo, N. H. Brooks, H. Frerichs, M. Jakubowski, R. Laengner, C. L. Lasnier, A. Loarte, R. A. Moyer, D. Orlov, H. Reimerdes, D. Reiter, U. Samm, H. Stoschus, E. A. Unterberg, and J. G. Watkins. The influence of three-dimensional stochastic magnetic boundaries on plasma edge transport and the resulting plasma wall interaction. *Journal of Nuclear Materials*, 415(1, Supplement):S886–S893, 2011. Proceedings of the 19th International Conference on Plasma-Surface Interactions in Controlled Fusion.

[48] G. Manfredi, S. A. Hirstoaga, and S. Devaux. Vlasov modelling of parallel transport in a tokamak scrape-off layer. *Plasma Physics and Controlled Fusion*, 53(1):015012, January 2011.

[49] J. P. Boris. Acceleration calculation from a scalar potential. jan 1970.

[50] T. D. Arber, K. Bennett, C. S. Brady, A. Lawrence-Douglas, M. G. Ramsay, N. J. Sircombe, P. Gillies, R. G. Evans, H. Schmitz, A. R. Bell, and C. P. Ridgers. Contemporary particle-in-cell approach to laser-plasma modelling. *Plasma Physics and Controlled Fusion*, 57(11):113001, sep 2015.

[51] A. Pukhov. Particle-in-cell codes for plasma-based particle acceleration, 2015.

[52] Charles K. Birdsall and A. B. Langdon. *Plasma Physics Via Computer Simulation.* McGraw Hill Higher Education, 1984.

[53] S. Markidis and G. Lapenta. The energy conserving particle-in-cell method. *Journal of Computational Physics*, 230(18):7037–7052, 2011.

[54] S. Mattei, K. Nishida, M. Onai, J. Lettry, M. Q. Tran, and A. Hatayama. A fully-implicit particle-in-cell monte carlo collision code for the simulation of inductively coupled plasmas. *Journal of Computational Physics*, 350:891–906, 2017.

[55] E. P. Alves, W. B. Mori, and F. Fiuza. Numerical heating in particle-in-cell simulations with monte carlo binary collisions. *Phys. Rev. E*, 103:013306, Jan 2021.

[56] R. Beatson and L. Greengard. *A short course on fast multipole methods*, pages 1–37. Numerical Mathematics and Scientific Computation. Oxford University Press, 1997.

[57] J. Barnes and P. Hut. A hierarchical O(N log N) force-calculation algorithm. *Nature*, 324(6096):446–449, December 1986.

[58] J. Ambrosiano, L. Greengard, and V. Rokhlin. The fast multipole method for gridless particle simulation. *Computer Physics Communications*, 48(1):117–125, 1988.

[59] J. P. Singh, C. Holt, T. Totsuka, A. Gupta, and J. Hennessy. Load balancing and data locality in adaptive hierarchical n-body methods: Barnes-hut, fast multipole, and radiosity. *Journal of Parallel and Distributed Computing*, 27(2):118–141, 1995.

[60] H. Langston, L. Greengard, and D. Zorin. A free-space adaptive FMM-Based PDE solver in three dimensions. *Communications in Applied Mathematics and Computational Science*, 6(1):79 – 122, 2011.

[61] N. Fang, C. Liao, and L. A. Ying. Darwin approximation to maxwell's equations. In G. Allen, J. Nabrzyski, E. Seidel, G. D. van Albada, J. Dongarra, and P. M. A. Sloot, editors, *Computational Science – ICCS 2009*, pages 775–784, Berlin, Heidelberg, 2009. Springer Berlin Heidelberg.

[62] L. Siddi, G. Lapenta, and P. Gibbon. Mesh-free hamiltonian implementation of two dimensional darwin model. *Physics of Plasmas*, 24(8):082103, 2017.

[63] PEPC Pretty Efficient Parallel Coulomb Solver. https://www.fz-juelich.de/en/ias/jsc/about-us/structure/simulation-and-data-labs/sdl-plasma-physics/pepc. Accessed: 28-11-2022.

[64] M. Winkel, R. Speck, H. Hübner, L. Arnold, R. Krause, and P. Gibbon. A massively parallel, multi-disciplinary barnes–hut tree code for extreme-scale n-body simulations. *Computer Physics Communications*, 183(4):880–889, 2012.

[65] M. S. Warren and J. K. Salmon. A Parallel Hashed Oct-Tree N-body Algorithm. In *Proceedings of the 1993 ACM/IEEE Conference on Supercomputing*, Supercomputing '93, pages 12–21, New York, NY, USA, 1993. ACM.

[66] P. Gibbon, R. Speck, A. Karmakar, L. Arnold, W. Frings, B. Berberich, D. Reiter, and M. Mašek. Progress in mesh-free plasma simulation with parallel tree codes. *IEEE Transactions on Plasma Science*, 38(9):2367–2376, 2010.

[67] Supercomputer configurations in Jülich Supercomputing Centre. https://apps.fz-juelich.de/jsc/hps/jureca/configuration.html. Accessed: 28-11-2022.

[68] H. Qin, S. Zhang, J. Xiao, J. Liu, Y. Sun, and W. M. Tang. Why is boris algorithm so good? *Physics of Plasmas*, 20(8):084503, 2013.

[69] S. Zenitani and T. Umeda. On the boris solver in particle-in-cell simulation. *Physics of Plasmas*, 25(11):112110, 2018.

[70] K. Königsberger. *Analysis 1.* Springer-Lehrbuch. Springer Berlin Heidelberg, 2003.

[71] H. R. Skullerud. The Stochastic Computer Simulation of Ion Motion in a Gas Subjected to a Constant Electric Field. *Journal of Physics D: Applied Physics*, 1(11):1567, 1968.

[72] B. van Wingerden, F. J. de Heer, E. Weigold, and K. J. Nygaard. Elastic scattering of electrons by molecular and atomic hydrogen. *Journal of Physics B: Atomic and Molecular Physics*, 10(7):1345–1362, may 1977.

[73] S. F. Biagi. Fortran program, MAGBOLTZ version 8.97, Oct 2012.

[74] M. Vranic, T. Grismayer, J. L. Martins, R. A. Fonseca, and L. O. Silva. Particle merging algorithm for pic codes. *Computer Physics Communications*, 191:65–73, 2015.

[75] C. H. Shon, H. J. Lee, and J. K. Lee. Method to increase the simulation speed of particle-in-cell (pic) code. *Computer Physics Communications*, 141(3):322–329, 2001.

[76] J. Teunissen and U. Ebert. Controlling the weights of simulation particles: adaptive particle management using k-d trees. *Journal of Computational Physics*, 259:318–330, 2014.

[77] Hübner H. A priori minimisation of algorithmic bottlenecks in the parallel tree code pepc. Master's thesis, Aachen, FH, Campus Jülich, 2011.

[78] J. Katajainen and J. L. Träff. A meticulous analysis of mergesort programs. In G. Bongiovanni, D. P. Bovet, and G. Di Battista, editors, *Algorithms and Complexity*, pages 217–228, Berlin, Heidelberg, 1997. Springer Berlin Heidelberg.

[79] R. Cole. Parallel merge sort. In *27th Annual Symposium on Foundations of Computer Science (sfcs 1986)*, pages 511–516, 1986.

[80] I. J. Davis. A Fast Radix Sort. *The Computer Journal*, 35(6):636–642, 12 1992.

[81] A. Bondi. van der waals volumes and radii. *The Journal of Physical Chemistry*, 68(3):441–451, mar 1992.

[82] J. Chew, P. Gibbon, D. Brömmel, T. Wauters, Y. Gribov, and P. de Vries. Three-dimensional first principles simulation of a hydrogen discharge. *Plasma Physics and Controlled Fusion*, 63(4):045012, feb 2021.

[83] D. J. Rose. Townsend Ionization Coefficient for Hydrogen and Deuterium. *Phys. Rev.*, 104:273–277, Oct 1956.

[84] H. Tagashira and J. Lucas. The measurement of ionization coefficients in hydrogen and nitrogen. *Journal of Physics D: Applied Physics*, 2(6):867–880, jun 1969.

[85] T. E. Sharp. Potential-energy Curves for Molecular Hydrogen and Its Ions. *Atomic Data and Nuclear Data Tables*, 2:119 – 169, 1970.

[86] J. K. Salmon, M. A. Moraes, R. O. Dror, and D. E. Shaw. Parallel Random Numbers: As Easy As 1, 2, 3. In *2011 International Conference for High Performance Computing, Networking, Storage and Analysis (SC)*, pages 1–12, Nov 2011.

[87] L. M. Chanin and G. D. Rork. Measurements of the first townsend ionization coefficient in neon and hydrogen. *Phys. Rev.*, 132:2547–2553, Dec 1963.

[88] J. Chew, P. Gibbon, D. Brömmel, P. de Vries, and Y. Gribov. First principles 3D simulation of tokamak plasma breakdown. In G. Giruzzi, C. Arnas, D. Borba, A. Gopal, and S. Lebedev, editors, *47th EPS Conference on Plasma Physics*, pages 141–144. European Physical Society.

[89] J. L. Autran, D. Munteanu, T. Saad Saoud, and S. Moindjie. Characterization of atmospheric muons at sea level using a cosmic ray telescope. *Nuclear Instruments and Methods in Physics Research Section A: Accelerators, Spectrometers, Detectors and Associated Equipment*, 903:77–84, 2018.

[90] A. V. Phelps. Cross Sections and Swarm Coefficients in H2 for Energies from 0.1 eV to 10 keV. *Journal of Physical and Chemical Reference Data*, 19(3):653–675, 1990.

[91] Additional atomic and molecular data for EIRENE. http://www.eirene.de/html/hydhel.html. Accessed: 28-11-2022.

[92] NIST electron-impact cross section for ionisation and excitation. https://physics.nist.gov/PhysRefData/Ionization/intro.html. Accessed: 28-11-2022.

[93] S. J. Doyle, D. Lopez-Aires, A. Mancini, M. Agredano-Torres, J. L. Garcia-Sanchez, J. Segado-Fernandez, J. Ayllon-Guerola, M. Garcia-Muñoz, E. Viezzer, C. Soria-Hoyo, J. Garcia-Lopez, G. Cunningham, P. F. Buxton, M. P. Gryaznevich, Y. S.

Hwang, and K. J. Chung. Magnetic equilibrium design for the smart tokamak. *Fusion Engineering and Design*, 171:112706, 2021.

[94] W. Baumjohann and R. A. Treumann. *Basic Space Plasma Physics*. Imperial College Press, 1996.

[95] First ITER magnet arrives this year. https://www.iter.org/newsline/. Accessed: 28-11-2022.

Schriften des Forschungszentrums Jülich
IAS Series

Band / Volume 43
Algorithms for massively parallel generic *hp*-adaptive finite element methods
M. Fehling (2020), vii, 78 pp
ISBN: 978-3-95806-486-7
URN: urn:nbn:de:0001-2020071402

Band / Volume 44
The method of fundamental solutions for computing interior transmission eigenvalues
L. Pieronek (2020), 115 pp
ISBN: 978-3-95806-504-8

Band / Volume 45
Supercomputer simulations of transmon quantum computers
D. Willsch (2020), IX, 237 pp
ISBN: 978-3-95806-505-5

Band / Volume 46
The Influence of Individual Characteristics on Crowd Dynamics
P. Geoerg (2021), xiv, 212 pp
ISBN: 978-3-95806-561-1

Band / Volume 47
Structural plasticity as a connectivity generation and optimization algorithm in neural networks
S. Diaz Pier (2021), 167 pp
ISBN: 978-3-95806-577-2

Band / Volume 48
Porting applications to a Modular Supercomputer
Experiences from the DEEP-EST project
A. Kreuzer, E. Suarez, N. Eicker, Th. Lippert (Eds.) (2021), 209 pp
ISBN: 978-3-95806-590-1

Band / Volume 49
Operational Navigation of Agents and Self-organization Phenomena in Velocity-based Models for Pedestrian Dynamics
Q. Xu (2022), xii, 112 pp
ISBN: 978-3-95806-620-5

Band / Volume 50
Utilizing Inertial Sensors as an Extension of a Camera Tracking System for Gathering Movement Data in Dense Crowds
J. Schumann (2022), xii, 155 pp
ISBN: 978-3-95806-624-3

Schriften des Forschungszentrums Jülich
IAS Series

Band / Volume 51
Final report of the DeepRain project
Abschlußbericht des DeepRain Projektes
(2022), ca. 70 pp
ISBN: 978-3-95806-675-5

Band / Volume 52
JSC Guest Student Programme Proceedings 2021
I. Kabadshow (Ed.) (2023), ii, 82 pp
ISBN: 978-3-95806-684-7

Band / Volume 53
Applications of variational methods for quantum computers
M. S. Jattana (2023), vii, 160 pp
ISBN: 978-3-95806-700-4

Band / Volume 54
Crowd Management at Train Stations in Case of Large-Scale Emergency Events
A. L. Braun (2023), vii, 120 pp
ISBN: 978-3-95806-706-6

Band / Volume 55
Gradient-Free Optimization of Artificial and Biological Networks using Learning to Learn
A. Yeğenoğlu (2023), II, 136 pp
ISBN: 978-3-95806-719-6

Band / Volume 56
Real-time simulations of transmon systems with time-dependent Hamiltonian models
H. A. Lagemann (2023), iii, 166, XXX pp
ISBN: 978-3-95806-720-2

Band / Volume 57
Plasma Breakdown and Runaway Modelling in ITER-scale Tokamaks
J. Chew (2023), xv, 172 pp
ISBN: 978-3-95806-730-1

Weitere ***Schriften des Verlags im Forschungszentrum Jülich*** unter
http://wwwzb1.fz-juelich.de/verlagextern1/index.asp

IAS Series
Band / Volume 57
ISBN 978-3-95806-730-1

Mitglied der Helmholtz-Gemeinschaft

JÜLICH
Forschungszentrum